EFFICIENT SAMPLING GEOMETRIES AND RECONSTRUCTION ALGORITHMS FOR ESTIMATION OF DIFFUSION PROPAGATORS

By

WENXING YE

A DISSERTATION PRESENTED TO THE GRADUATE SCHOOL
OF THE UNIVERSITY OF FLORIDA IN PARTIAL FULFILLMENT
OF THE REQUIREMENTS FOR THE DEGREE OF
DOCTOR OF PHILOSOPHY

UNIVERSITY OF FLORIDA

2012

© 2012 Wenxing Ye

To my parents

ACKNOWLEDGMENTS

I owe a great thank you to many people who helped me finish my dissertation. First and foremost, I would like to thank Dr. Baba Vemuri, my advisor, who introduced me into the field of medical image processing and guided me through my Ph.D. study using his tireless inspiration and rich academic experience. I am also thankful that Dr. Vemuri offered me full research assistantship with which I could put all my focus on the research and not worry about financial problems. Dr. Vemuri built the example of a passionate and serious scholar for me.

I would also like to appreciate Dr. Alireza Entezari, my co-advisor, who is always available for discussion when I need his technical advise. He selflessly shared his experience and knowledge so that I avoided making many mistakes. From him, I learned the importance of mathematical thinking and carefulness in solving a research problem. The memories are still clear that he worked together with me from morning to the night before the conference deadlines. It is my luck to have him as a patient friend and knowledgeable mentor.

Furthermore, I would like to express my sincere appreciation to Dr. Anand Rangarajan, Dr. Jay Gopalakrishnan and Dr. Stephen Blackband for serving as my Ph.D. committee members. They spent hours in discussing details of my works. The courses taught by Dr. Rangarajan and Dr. Gopalakrishnan provided critical knowledge and training for my later research and Dr. Blackband gave many advises from a neuroscientist point.

All the works in this dissertation are evaluated on real diffusion MRI data provided by the McKnight Brain Institution at the University of Florida. I owe my deepest gratitude to Sharon Portnoy and Dr. MinSig Hwang who worked very hard collecting testing data for me. Their technical suggestions and feedbacks also helped a lot in adjusting my studies to meet the clinical requirements. In addition, I am grateful that Sharon has taken the time to correct the wording of my manuscripts.

Moreover, I want to thank all my friends in the laboratory for Computer Vision, Graphics, and Medical Imaging. I benefited a lot from the tools and articles developed by Dr. Angelos Barmpoutis, Dr. Fei Wang and Dr. Bing Jian. I also gained many enlightenments from the discussion with Guang Cheng, Yuchen Xie, Ting Chen and Meizhu Liu. It has been really good time working with them.

I also would like to thank Shannon Chillingworth, the graduate coordinator of the Electrical and Computer Engineering department. Her professional knowledge and always in-time assistance saved me lots of time in handling non-academic affairs in the university.

Last but not least, I thank generous funding for this research from the NIH grants, EB007082 and NS066340 to my advisor, Dr. Vemuri.

TABLE OF CONTENTS

page

ACKNOWLEDGMENTS 4

LIST OF TABLES 8

LIST OF FIGURES 9

ABSTRACT 11

CHAPTER

1 DIFFUSION PROPAGATOR RECONSTRUCTION FRAMEWORK 13

1.1 Introduction to Diffusion Propagator Reconstruction 13
1.2 Common Sampling Geometries 14
1.3 Existing Reconstruction Methods 16
1.3.1 Diffusion Tensor Imaging 17
1.3.2 High Angular Resolution Diffusion Imaging 17
1.3.3 Q-ball Imaging 18
1.3.4 Diffusion Spectrum Imaging 19
1.3.5 Reconstruction from Multi-shell Sampling 19
1.4 Main Contributions 20

2 MULTIVARIATE LATTICES AND THE OPTIMAL INTERPOLATION FUNCTIONS 23

2.1 Sampling Multivariate Signals 23
2.2 Multidimensional Lattices 26
2.2.1 Point Lattices 26
2.2.2 Dicing Lattices 27
2.2.3 Sphere Packing and Covering Lattices For Sampling 27
2.3 Sinc Functions On Multidimensional Lattices 29
2.3.1 Zonotopes 31
2.3.2 Space Tesselations and Lattice Voronoi Polytopes 33
2.3.2.1 Two-Dimensional Lattices 34
2.3.2.2 Three-Dimensional Lattices 35
2.3.3 FCC and BCC Lattices 36
2.3.4 Multivariate Shannon Wavelets 38
2.3.5 Multivariate Lagrange Interpolant 40
2.3.6 Multidimensional Lanczos Windowing 42
2.4 Experimental Comparison 45
2.4.1 Experiments Setup 45
2.4.2 Visual Comparison 48
2.4.3 Numerical Comparison 48

3 TOMOGRAPHIC RECONSTRUCTION OF DIFFUSION PROPAGATORS USING OPTIMAL SAMPLING LATTICES 53

3.1 Motivations 53
3.2 Algorithm and Implementation 54
3.3 Algorithm Evaluation 55

4 RECONSTRUCTION FROM INTERLACED SAMPLING 59

4.1 Interlaced Sampling Scheme 59
4.2 Reconstruction Algorithm 63
4.3 Experiments 67
4.3.1 Experiments on synthetic data 67
4.3.2 Experiments on real data 72

5 BOX SPLINE BASED RECONSTRUCTION METHOD 79

5.1 Box Splines and Radon Transform 80
5.2 Detailed Algorithm 82
5.3 Experimental Results of the Algorithm 84

6 RECONSTRUCTION OF A DIFFUSION PROPAGATOR FIELD 88

6.1 Overview: From Fixed Basis to Data Driven Dictionary 88
6.2 Adaptive Kernels for Multi-fiber Reconstruction 89
6.3 Dictionary based Reconstruction Framework 91
6.4 Results 93
6.4.1 Synthetic Dataset 93
6.4.2 Real Dataset 95

7 CONCLUSIONS 97

REFERENCES 99

BIOGRAPHICAL SKETCH 108

LIST OF TABLES

Table page

2-1 Decomposition of the Brillouin zone for the BCC lattice, $\Xi^{\mathbb{B}}$ used to construct the $\text{sinc}_{\mathbb{B}}$. 37

2-2 Decomposition of the Brillouin zone for the FCC lattice, $\Xi^{\mathbb{F}}$ used to construct the $\text{sinc}_{\mathbb{F}}$. 38

3-1 SSE comparison of reconstructions from different lattices with N_r, $N_\theta = 12$, $N_\phi = 13$, $\alpha = 90°$ 56

3-2 SSE comparison of reconstructions from different lattices with N_θ, N_ϕ, $N_r = 10$,$\alpha = 90°$ 56

3-3 SSE comparison of reconstructions from different lattices with α, $N_r = 10$, $N_\theta = 12$, $N_\phi = 13$ 56

3-4 SSE comparison of reconstructions from different lattices with σ, $N_r = 10$, $N_\theta = 12$, $N_\phi = 13$, $\alpha = 90$ 57

4-1 Sampling directions used in our experiments for Rhombic Triacontahedron and Icosidodecahedron. 70

5-1 MSE in percentage of the reconstructions for the synthetic data. 85

LIST OF FIGURES

Figure page

1-1 Sampling schemes used in diffusion MRI. 15

2-1 A lattice **L** and its fundamental domain (Voronoi cell). 26

2-2 3-D Cartesian, BCC and FCC lattices. 28

2-3 Hexagonal lattice and its Brillouin zone. 34

2-4 The fundamental domains of all 3-D lattices tessellate the space. 36

2-5 Decomposition of a rhombic dodecahedron and a truncated octahedron 39

2-6 Brillouin zone subdivided to derive a multi-scale function for Shannon wavelets. 40

2-7 Lagrange basis for polynomial interpolation when the nodes are $\mathbb{Z}$ converges to sinc. 41

2-8 Lanczos filter as a multiplication with the main lobe of the scaled sinc function. 43

2-9 Plots of $\text{sinc}_{\mathbb{H}}$ and its Lanczos windowed version in the space domain and the frequency domain. 46

2-10 Benchmark volumetric datasets. 47

2-11 Visual comparison of ML isosurface images rendered from Cartesian, BCC and FCC lattices. 49

2-12 Visual comparison of carp fish isosurface images rendered from Cartesian, BCC and FCC lattices. 50

2-13 Visual comparison of bonsai tree isosurface images rendered from Cartesian, BCC and FCC lattices. 50

2-14 The RMS error comparison of BCC, FCC versus $41 \times 41 \times 41$ Cartesian lattice. 51

3-1 Visual comparison of the reconstructed $P(\mathbf{r})$. 57

3-2 Probability maps reconstructed from real data set. 58

4-1 Diagram of the reconstruction scheme using interlaced sampling. 60

4-2 Comparison of 2D standard and interlaced sampling schemes in the case of CT reconstruction. 60

4-3 The structure of BCC lattice as 2-D Cartesian layers of samples *shifted* on alternate Z slices. 61

4-4 Shape of polyhedra used in sampling schemes. 62

4-5 Illustration of 3-D interlaced and standard sampling geometries. 64
4-6 Reconstruction of $P(\mathbf{r})$ in the two-fiber case. 69
4-7 Plots showing the normalized MSE of the reconstruction for synthetic data of two-fiber crossings. 71
4-8 Plots showing the normalized MSE of the reconstruction for single fiber synthetic data of different FA values. 72
4-9 Reconstruction of $P(\mathbf{r})$ in the three-fiber case. 73
4-10 Plots showing the normalized MSE of the reconstruction for synthetic data of three-fiber crossings. 74
4-11 Reconstruction results on dataset $\#1$ 75
4-12 Reconstruction results on dataset $\#2$ 76
4-13 Reconstruction results on dataset $\#3$ 78
5-1 Diagram of the box spline based reconstruction process. 80
5-2 A 2-D illustration of Radon transform geometry. 82
5-3 The desired isosurface of $P(\mathbf{r})$. 84
5-4 Reconstruction results for the synthetic data. 85
5-5 Reconstruction results for a region of the multi-shell mouse brain data with different box spline basis orders. 86
6-1 Reconstructed diffusion propagator fields using different methods. 94
6-2 Reconstruction error comparison and the convergence plot. 95
6-3 S_0 image of the optic chiasm and the ROI. 95
6-4 Reconstructed region of interest from real data using different methods. 96

Abstract of Dissertation Presented to the Graduate School
of the University of Florida in Partial Fulfillment of the
Requirements for the Degree of Doctor of Philosophy

EFFICIENT SAMPLING GEOMETRIES AND RECONSTRUCTION ALGORITHMS FOR ESTIMATION OF DIFFUSION PROPAGATORS

By

Wenxing Ye

May 2012

Chair: Baba C. Vemuri
Cochair: Alireza Entezari
Major: Electrical and Computer Engineering

Diffusion weighted magnetic resonance imaging (DW-MRI) is a non-invasive techniques that can reveal the anatomical structure of living organism. Through measuring directional diffusion of water molecules in tissue rich in fiber structure, DW-MRI can provide invaluable *in vivo* information about the neuronal connectivity patterns. This kind of information is extremely important for many clinical applications, especially when brain areas which consist of abundant white matter fibers is concerned.

Diffusion propagator is the most widely used measure to describe the water diffusion quantitatively. It gives the probability of water molecule motion along a vector in fixed MR setting. The main aim of this dissertation is to investigate better ways of sampling and reconstructing the diffusion propagator from a signal processing point of view.

This dissertation shows a model free framework for diffusion propagator reconstruction with special focus on increasing the total reconstruction accuracy through optimizing the sampling geometry. The reconstruction framework is proposed through gradually introducing the concepts of optimal sampling lattice, interlaced mult-shell sampling scheme, multi-dimensional sinc basis representation and box-spline basis representation.

The main difficulty in diffusion propagator reconstruction lies in the fact that sampling of diffusion signal is very time consuming and the time is linearly proportional

to the number of sample points. In order to maintain the angular resolution, in practice, the diffusion signal is sampled on spherical shells. There are many ways to estimate the diffusion propagator, which is the Fourier transform of the diffusion signal, from the spherical samples. One of them is to set a Cartesian lattice in the space of the diffusion signal and estimate the values of diffusion signal on the lattice points. Then, the diffusion propagator can be easily estimated through a fast Fourier transform. One intuitive idea is to replace this Cartesian lattice with a body centered cubic (BCC) lattice. The interlaced mult-shell sampling means sampling the diffusion signal in an interlaced style across every alternating shell. A weighted sum of the shifted sinc or box-spline basis are used to represent the diffusion signal or the diffusion propagator and the weighting coefficients are estimated by solving an inverse problem. With these coefficients, a continuous form of the estimated diffusion propagator is obtained.

Each of the concepts has its own way of improving the reconstruction accuracy. We have shown this through experimental comparison on both synthetic and real MRI data. As a whole framework, it seeks the more efficient way of sampling and reconstruction to achieve higher accuracy without increasing the sampling burden. Generally, the framework can take common spherical samples and generate accurate, model independent reconstructions.

In the end, the concept of dictionary learning and non-local regularization were introduced for reconstructing a regularized field of diffusion propagators. By investigating the spatial correlation in the field, the algorithm can produce results more resilient to the noise compared with the voxel-wise reconstruction methods. This is the first such algorithm in the field and our future will involve combination of this technique with the optimal sampling framework briefly described above.

CHAPTER 1
DIFFUSION PROPAGATOR RECONSTRUCTION FRAMEWORK

1.1 Introduction to Diffusion Propagator Reconstruction

Diffusion MRI is a non-invasive imaging technique that exhibits sensitivity to Brownian motion of water molecules through tissue *in vivo*. Water molecules exhibit preferred directional diffusion through tissue rich in white matter fibers. This directional preference allows one to infer connectivity patterns as well as changes in them over time that can be used in various clinical applications. For example, it is shown to be sensitive to the evaluation of early ischemic stages of the animal brain [86]. Many experiments have been exploited to investigate the anisotropic micro-structure of the fibrous tissues like muscle and white matter in the brain [22, 26, 66, 85].

One of the major tasks of diffusion MRI is the reconstruction of the 3-D diffusion propagator $P(\mathbf{r})$ characterizing the diffusion process of water molecules in fibrous tissues with probability density function (PDF). By integrating $P(\mathbf{r})$ from $||\mathbf{r}|| = 0$ to ∞, diffusion orientation distribution functions (ODF) is defined and exploited by many recent works as a replacement to $P(\mathbf{r})$ [2, 36, 59, 107, 110]. However, ODF only provides the averaged angular information about the diffusion process. In contrast, the diffusion propagator, $P(\mathbf{r})$, provides both radial and angular information and describes the diffusion process more accurately. Because of the additional radial information, $P(\mathbf{r})$ can be used to estimate extra features such as probability of diffusion permeability of the walls, average cell size, axonal diameter and other features that are useful in sensing white matter anomalies [28].

Under the narrow pulse assumption, i.e. the duration of the applied diffusion sensitizing gradients δ is much smaller than the time between the two pulses Δ, the diffusion signal $E(\mathbf{q})$ in $\mathbf{q}$-space and the diffusion propagator $P(\mathbf{r})$ in distance space are related through Fourier transform [20] as:

$$P(\mathbf{r}) = \int E(\mathbf{q}) exp(-2\pi i \mathbf{q} \cdot \mathbf{r}) d\mathbf{q} \tag{1–1}$$

where $E(\mathbf{q}) = S(\mathbf{q})/S_0$, S_0 is the diffusion signal with zero diffusion gradient ($\mathbf{q} = 0$), $\mathbf{r}$ is the displacement vector, $\mathbf{q} = \gamma\delta\mathbf{G}/2\pi$ is the reciprocal space vector, γ is the gyromagnetic ratio and $\mathbf{G}$ is the gradient vector. To be noted, $b = \gamma^2\delta^2|\mathbf{G}|^2 t$ is an important quantity, called b-value, that characterizes the sensitivity of MR sequences to diffusion. Here, $t = \Delta - \delta/3$ where Δ is the time between diffusion gradients and δ is the duration of diffusion gradient.

Diffusion propagator $P(\mathbf{r})$ is not directly measurable. Instead, the imaging spectrometer measures the diffusion signal $E(\mathbf{q})$. (1–1) states that the diffusion propagator is the 3-D Fourier transform of the diffusion signal $E(\mathbf{q})$ and provides the foundation for reconstructing $P(\mathbf{r})$. The problem seems straight forward. We can get accurate estimation of $P(\mathbf{r})$ through taking Fourier transform on samples of $E(\mathbf{q})$, as long as enough samples are collected. However, sampling $E(\mathbf{q})$ is very time consuming and the time cost is linearly increasing with the number of samples demanded. So how to sample $E(\mathbf{q})$ and what prior information to use emerges as the two core problems. The first problem is the sampling geometry problem and the second is the model selection problem (choosing a model means assuming prior information on the signal). The final goal is to achieve an accurate estimation of $P(\mathbf{r})$ from very few number of samples of $E(\mathbf{q})$.

1.2 Common Sampling Geometries

In diffusion weighted MRI, the diffusion properties of a tissue are determined by measuring its response to an oriented magnetic field gradient. By applying gradients of different strengths and directions, we obtain samples of the diffusion signal in 3-D $\mathbf{q}$-space for each voxel location within the tissue. For each $\mathbf{q}$-space sample, we need to alter the orientation and/or strength of the magnetic field gradient and measure the response for the entire volume, $\mathbf{q}$-space sampling cannot be performed in parallel -

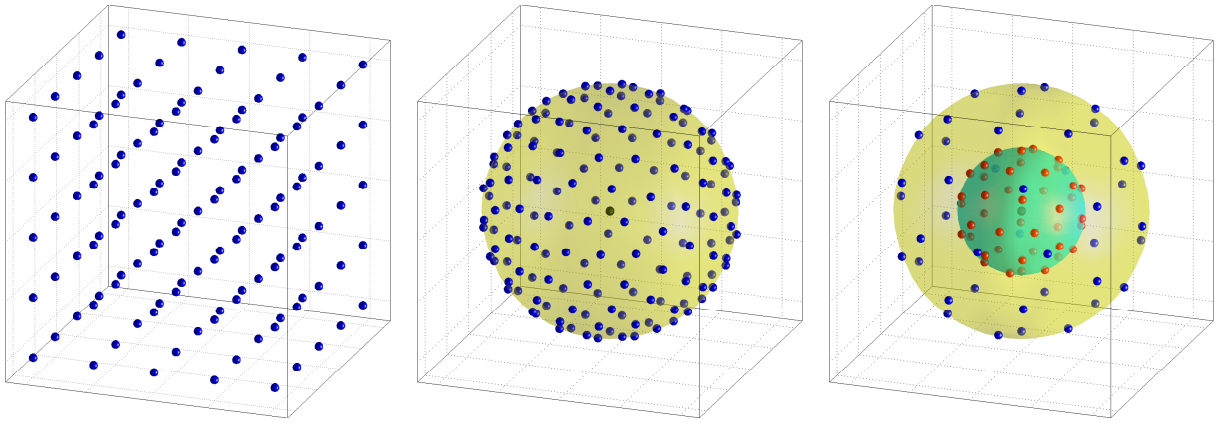

(a) (b) (c)

Figure 1-1. Sampling schemes used in diffusion MRI. (a) Cartesian sampling, (b) Spherical sampling, (c) Multi-shell spherical sampling.

the sampling time increases linearly with the number of $\mathbf{q}$-space samples. Therefore, within the signal acquisitions stage, we seek an optimal balance between the number of samples and reconstruction accuracy.

The sampling scheme determines how the sample points are distributed throughout 3-D $\mathbf{q}$-space. An approach, employed by DSI, is to put the samples on a regular Cartesian lattice (Figure 1-1(a)). This is the most conventional scheme used in signal processing where Shannon sampling theory provides the theoretical framework for sampling and reconstruction. In addition, $P(\mathbf{r})$ can be reconstructed through the Fast Fourier transform (FFT). However, this scheme is time consuming since it needs a large number of $\mathbf{q}$-space samples to achieve a reasonably accurate reconstruction.

In practice, the most widely used sampling scheme in diffusion MR is to take a sample at the origin together with uniformly distributed samples on a spherical shell in the $\mathbf{q}$-space (Figure 1-1(b)). All of the samples on the spherical shell $|\mathbf{q}| = \sqrt{b/t}/2\pi$ are taken under an applied magnetic field gradient of the same strength but with different directions. The benefit is that variations in signal to noise ratio and other factors related to the strength of the magnetic field are minimized. With some global or directional

decay models of the signal, $P(\mathbf{r})$ can be computed analytically through the continuous Fourier transform [37, 57].

A notable variation of this scheme acquires samples from multiple shells (Figure 1-1(c)), i.e. multiple b values, each with the same directional distribution of samples. In this *multi-shell setting*, more sophisticated models involving more parameters can be used. This type of model-based scheme needs fewer samples than DSI and can produce smooth reconstructions, but it is limited by the assumptions of proposed models [37, 57].

1.3 Existing Reconstruction Methods

Once the samples are collected, the next problem is to estimate the diffusion propagator from those samples. Many techniques have been proposed with different prior assumptions about the signal. Making an assumption finally turns out to be choosing a mathematical model. Different models have different degrees of freedom (i.e., number of parameters) which requires different numbers of samples to be fully determined. A model with higher degree of freedom is more flexible in representing more complicated signals. Of course, the price to pay is the need of more samples. The extreme case is the Shannon sampling which can represent any bandlimited signal but requires the most number of samples. The most common assumption in the diffusion propagator reconstruction scenario is that the $\mathbf{q}$ space diffusion signal decays along the radial direction exponentially. There are other assumptions which imposes a global mathematical model over the 3-D $\mathbf{q}$ space or assumes multi-exponential radial decaying for multi-shell data samples.

At times, introducing a strong model (i.e., of few parameters) offers the advantages of analytical reconstruction through Fourier transformation, smooth results which are resistant to noise, and a limited number of required samples. However, any model-based technique is inherently biased, as it will always produce results that obey the underlying model. This model bias on the diffusion signal will transfer to the reconstruction error of diffusion propagator through the Fourier transform.

In this section, some typical reconstruction methods are briefly reviewed. Many related publications about various approaches are also cited to provide extra information for the interested readers.

1.3.1 Diffusion Tensor Imaging

Diffusion tensor imaging (DTI) proposed by [13, 14] is a simple yet commonly used technique. It assumes the diffusion signal can be represented with an oriented Gaussian probability density function as:

$$S(\mathbf{G}) = S_0 exp(-b\mathbf{g}^T D\mathbf{g}) \tag{1–2}$$

where $b = (\gamma\delta G)^2 t$ is the diffusion weighting, $t = \Delta - \delta/3$ is the effective diffusion time, D is the apparent diffusion tensor, $G = |\mathbf{G}|$ and $\mathbf{g} = \mathbf{G}/G$. It is also referred to as the second order tensor model. This model has 7 coefficients which can be fixed with only 7 diffusion weighted images taken with different gradient directions. The principal eigenvector of the diffusion tensor specifies the fiber orientation at the given position. For DTI, the estimation is simple, the sampling burden is light and some successful applications in fiber tracking were exploited in the region of brain and spinal cord with significant white matter coherence [12, 29, 54, 67, 84, 119]. However, since the assumed oriented Gaussian PDF has only one principal orientation, It is now well known that this model fails to capture complex geometries caused by crossing, kissing or splaying fibers that result in orientational heterogeneity in a voxel [109]. This has spurred the development of improved acquisition techniques and reconstruction methods [2, 10, 11, 37, 56, 57, 64, 89, 106].

1.3.2 High Angular Resolution Diffusion Imaging

[108] introduced a high angular resolution diffusion imaging (HARDI) method which estimates a more sophisticated diffusion profile according to many orientations, usually many more than 7 directions which are needed by DTI. Without fitting a global model function to the data, the original HARDI method calculates the diffusion profile using the

Stejskal-Tanner expression [99]:

$$E(\mathbf{u}) = exp(-bD(\mathbf{u})) \tag{1–3}$$

where $\mathbf{u}$ is a unit vector defining the diffusion direction. The results are given as an angular distribution of apparent diffusivities $D(\mathbf{u})$ which has a complicated structure in voxels with orientational heterogeneity [109, 114]. Several studies have been proposed such as representing the diffusivity function $D(\mathbf{u})$ with a spherical harmonic expansion [4, 50], generalization of DTI using higher order tensors [10, 88, 90], modeling the diffusion signal using a mixture of Gaussian densities [109], combining hindered and restricted models of water diffusion (CHARMED) [7], direct estimation of the fiber orientation using spherical deconvolution [105], a tensor distribution model introduced in [57] and diffusion orientation transform (DOT) [89] which analytically evaluates the Fourier relation in spherical coordinates assuming the diffusion signal being a mixture of exponential decay functions.

1.3.3 Q-ball Imaging

The original version of q-ball imaging (QBI) is another model independent reconstruction method [109]. This method takes diffusion signal samples on a single $\mathbf{q}$ space sphere and closely resembles the ODF through spherical Radon transform. Spherical Radon transform, also known as Funk-Radon transform, takes a function on a sphere and outputs another spherical functions through the following integration:

$$(\mathcal{R}[f])(\mathbf{u}) = \int_{|\mathbf{x}|=1} f(\mathbf{x})\delta(\mathbf{u}^T\mathbf{x})d\mathbf{x} \tag{1–4}$$

where $\mathbf{u}$ is a unit vector.

This method is efficient and model free. But the resembled ODF, supposed to be the radial integration of the diffusion propagator, is actually the integration of the real diffusion propagator convolved with a 0-order Bessel function. This unwanted convolution degrades the fidelity of the reconstructions. A recent study [2] shows an

improved version of QBI which is more accurate in mathematics, gives sharper results and works in multiple $\mathbf{q}$-shell situations. However, QBI only works for reconstructing ODF which is a compromised version of diffusion propagator, not for the diffusion propagator itself.

1.3.4 Diffusion Spectrum Imaging

Diffusion spectrum imaging (DSI) [116], i.e. $\mathbf{q}$-space imaging (QSI) was proposed to sample the diffusion signal on a dense 3-D Cartesian lattice and reconstruct the diffusion propagator through 3-D fast Fourier transform (FFT). It has been extended through changing the sampling scheme into body centered cubic lattice [24] and some hybrid lattice [118], or using the tomographic reconstruction principle [92]. These methods have weak assumption about the diffusion signal and can be evaluated precisely through Shannon sampling theorem. But the heavy sampling burden makes the acquisition time-intensive and limits the widespread application.

1.3.5 Reconstruction from Multi-shell Sampling

Recently, reconstruction methods using multiple $\mathbf{q}$-shell acquisitions were investigated. Under such multi-shell situation, [37] introduced a diffusion propagator reconstruction method assuming that the diffusion signal attenuation can be estimated with the 3-D Laplace equation, [2] discussed about ODF reconstruction in multi-shell q-Ball imaging (QBI) within constant solid angle assuming radial multi-exponential model, [89] extended the DOT method to the multi-shell data with multi-exponential radial decaying assumption.

Hybrid diffusion imaging (HYDI) [118] was proposed as an alternative to DSI. It samples diffusion signal on several spherical shells and estimates the signal values on a dense 3-D Cartesian lattice through linear interpolation. The idea of interpolating spherical samples onto a dense regular lattice is also used in our proposed method discussed in Chapter 3 and Chapter 4. However, HYDI acquires more samples on shells

with higher b-values (similar to CHARMED [6]), where SNR decreases which leads to a less accurate reconstruction as discussed in [8].

1.4 Main Contributions

Current reconstruction methods, with or without model assumptions, have their own problems in the sense of accuracy. The model based methods (i.e., with strong assumption about the signal) share the same signal decaying assumption stated by Stejskal-Tanner equation. The Stejskal-Tanner equation is derived from a microscopic, free diffusion physical model which has no boundary conditions. Actually, the diffusion signal collected in MRI is from the cumulative microscopic diffusions of water molecules within a millimetric voxel. In addition, the diffusion of these water molecules are obviously restricted by the fiber structures in the tissue. Thus, the exponential signal decaying assumption is compromised and these model based methods will introduce false bias into the reconstruction.

On the other hand, the current model independent methods (i.e., with very weak assumption about the signal) have their own drawbacks. QBI can only reconstruct contaminated, radial integrated version of diffusion propagator. DSI has very heavy sampling burden for acceptable reconstruction accuracy.

The purpose of this work is to propose a framework of getting reliable and accurate diffusion propagator reconstructions from small number of samples. It tries to maintain the advantages of DSI technique from much less spherical samples.

The desired reconstruction framework should be accurate, reliable and does not bring too much burden in the sampling stage. So we decided to start with spherical samples and push them onto a much denser regular lattice in $\mathbf{q}$ space. The extension procedure is feasible as long as the diffusion signal is smooth. This framework has the advantages of QSI, but does not require so many samples. The main assumption here is the smoothness of the diffusion signal which is natural and practical. There are three problems in this framework: the choice of the regular lattice, the distribution of

the spherical samples and the approach to push spherical samples to the lattice points. In this dissertation, we visit each of the problems separately to make the framework complete.

The main contributions can be summarized as following:

A geometric approach to explicitly derive the multivariate sinc functions for general sampling lattices is given. It provides a useful tool for interpolating and reconstructing signals sampled on different lattices. Chapter 2 gives the derivation and compares the sampling efficiency of different lattices. The optimal sampling lattice and the corresponding sinc function will be used in Chapter 3 and Chapter 4.

The idea of optimal sampling lattice is introduced into the tomographic reconstruction framework to estimate the diffusion propagators. Chapter 3 shows that simple replacement of the traditional Cartesian lattice with optimal body-centered cubic (BCC) lattice leads to increased reconstruction accuracy of the tomographic method.

A novel interlaced sampling geometry is proposed as a better way of distributing diffusion signal samples on multiple $\mathbf{q}$ shells. The interlaced geometry, compared with the non-interlaced sampling, preserves more angular information of the diffusion signal as shown in Chapter 4. In addition, Section 4.2 gives the algorithm of estimating the signal values on regular lattices, Cartesian or BCC, from the spherical samples. This algorithm is based on the sinc functions derived earlier and shows the further increase of reconstruction accuracy due to the usage optimal BCC lattices.

For the first time, box splines are introduced into the tomographic framework of diffusion propagator reconstruction. Chapter 5 introduces an algorithm which reconstructs $P(\mathbf{r})$ in box spline basis from its projections. Experiments show that using higher order box splines increases the reconstruction accuracy with the same number of samples. Different box splines can be defined for different lattices, so combining this algorithm with interlaced sampling geometry and optimal lattices could be an alternative version of the tomographic reconstruction framework discussed within this dissertation.

A dictionary-based framework is proposed for the reconstruction of a diffusion propagator field with non-local regularization. This framework is shown to be very resilient to noise compared with voxel-wise methods. In its preliminary form, spherical spline basis and single shell sampling are used. But there is no doubt that the interlaced sampling can play a role in potential accuracy improvement. Details are shown in Chapter 6.

CHAPTER 2
MULTIVARIATE LATTICES AND THE OPTIMAL INTERPOLATION FUNCTIONS

One of the key ideas in this dissertation is the introduction of different lattices, BCC lattice, in the $\mathbf{q}$ space onto which we want to push the spherical samples. Later, we will also find that the lattice dependent sinc interpolating function plays a very important role in the reconstruction stage. Different from the Cartesian case, where the sinc function is simply a tensor product of univariate sinc functions, the sinc functions for BCC and FCC (face centered cubic) lattices are not separable and more complicated to derive. In this chapter, we are introducing the readers to the basics of multivariate lattices and give the derivations of the corresponding sinc functions.

2.1 Sampling Multivariate Signals

Sampling theorem plays a pivotal role in signal processing and information theory as it is key to the discrete-continuous model for sampling and reconstruction of univariate signals. The celebrated Whittaker-Shannon-Kotel'nikov theorem [111] elegantly introduces $\mathrm{sinc}(x) := \sin(\pi x)/(\pi x)$ whose shifts provide a countable basis for the space of bandlimited functions: a space, PW_T, of functions whose Fourier transforms vanish outside the open interval $]-\pi T, \pi T[$. The reconstruction formula presents a cardinal series expansion of any such function f:

$$f(x) = \sum_{n\in\mathbb{Z}} f(nT)\,\mathrm{sinc}\,(x/T - n). \tag{2–1}$$

In other words, the sampling theorem implies that a function $f \in \mathrm{PW}_T$ is completely determined by its samples $f(nT)$, $n \in \mathbb{Z}$. While Shannon's sampling theorem has had an enormous impact on communication and various engineering applications, it serves as a theoretical framework.

The bandlimited assumption is, sometimes, a prohibitively strong assumption specially for functions with finite (compact) support. Non-bandlimited signals are often passed through a pre-filtering step that makes them bandlimited. This pre-filtering

operation can be elegantly viewed as a projection onto the space of bandlimited functions [111]. Moreover, for non-bandlimited functions, Slepian functions [95, 97] allow for concentrating the energy of a signal over a finite bandwidth. There are several generalizations of sampling theorem [15, 53] such as for functions defined over locally compact abelian groups [62].

The significance of sinc function, from the theoretical point of view, is that it provides an orthonormal basis and a reproducing kernel for the space of bandlimited functions. The sinc function serves as the theoretical base for development of 1-D signal processing tools [17, 111]. Moreover, sinc function has provided a rich class of approximations and numerical analysis tools that provide efficient solutions to a variety of computational problems [63, 100, 101, 103].

For sampling multivariate functions the Cartesian lattice is the common choice. The separable structure of Cartesian lattice allows us to employ tensor-product filtering operations in multidimensions. For instance, the sinc function, can be easily extended to a multidimensional Cartesian sampling lattice via a tensor product of univariate sinc functions. The separable structure of Cartesian lattice makes it the preferred lattice in applications.

The Cartesian lattice, from the sampling theory viewpoint, is inefficient. The works of Miyakawa [83] and Petersen and Middleton [91] demonstrate the advantages of sphere packing and sphere covering lattices for sampling (see also [48]). In contrast to the Cartesian case, these lattices are not separable. The tensor product of sinc function or other 1-D filters fail to adhere to the non-separable nature of these lattices.

Although these lattices are interesting from the theoretical aspects [30, 81, 91], for their adoption in applications one need special signal processing tools tailored to their non-separable structure. This chapter presents an explicit derivation of sinc functions on multidimensional lattices together with a non-separable windowing scheme, which are fundamental tools for general multi-dimensional lattices. Our specific

contributions include: This chapter introduces a geometric approach to explicitly derive multivariate sinc functions on sampling lattices. The framework also allows one to derive complete interpolatory sequences (Riesz basis) for the space of functions whose Fourier transforms are supported on zonotopes.

This geometric framework allows us to derive a non-separable generalization of the 1-D Shannon wavelets in the multivariate setting. Moreover, in the univariate setting, the sinc function is known to be equivalent to the Lagrange basis function when the nodes are integers. Using this geometric framework, we devise a multidimensional counterpart where the sinc function turns out to be a sum of Lagrange basis functions.

The construction framework applies to any multi-dimensional lattices satisfying the "dicing" [46] property. To give concrete examples, we focus on characterizing all bivariate and trivariate sinc functions that cover *all* 2-D and 3-D lattices.

We introduce a non-separable, windowing technique that generalizes the concept of Lanczos filter to the multivariate setting. This windowing technique allows us to employ the sinc functions for reconstruction of volumetric datasets sampled on BCC and FCC lattices and perform comparisons with Cartesian-sampled datasets. The approximation spaces spanned by countably many translates of a single function (kernel or generator) are foundational to spline theory and sampling theory (as well as wavelet and radial basis function theories). While the spline theory often considers the case when the kernel is compactly supported, the paradigm in sampling theory is the compactness of the support of the Fourier transform of the kernel [35]. It is intriguing to note that the two have a somewhat reciprocal relationship, specially when considering the structure of Lanczos windowing functions. A spline framework was proposed for multidimensional lattices [82] and the current chapter offers the dual paradigm of the sinc functions for sampling theory on these lattices.

The construction of the sinc function, limited to the BCC lattice, was illustrated in [44] (lacking a practical implementation). In the current chapter we generalize

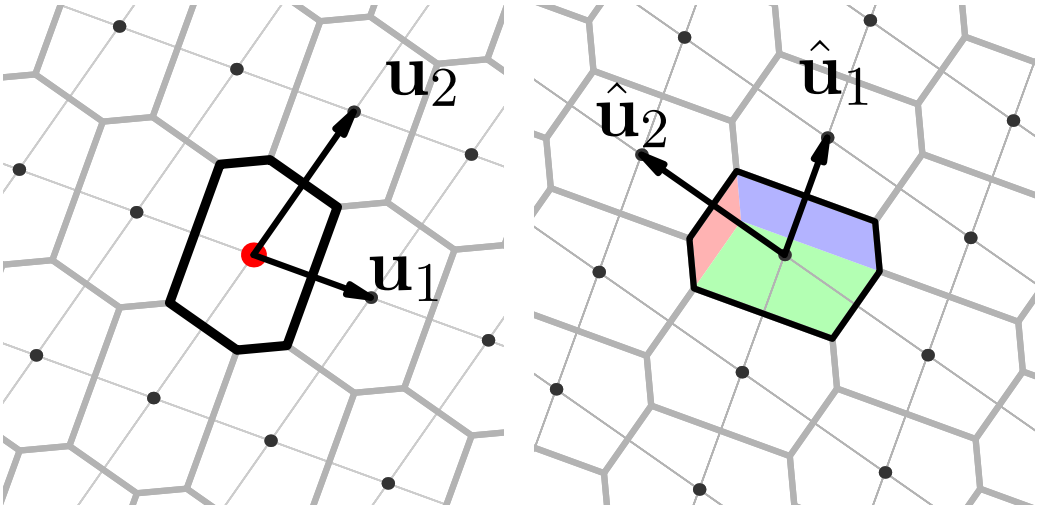

Figure 2-1. A lattice $\mathbf{L} = [\mathbf{u}_1, \mathbf{u}_2]$ and its fundamental domain (Voronoi cell) are illustrated on the left. The reciprocal lattice $\hat{\mathbf{L}} = \mathbf{L}^{-\top} = [\hat{\mathbf{u}}_1, \hat{\mathbf{u}}_2]$ is shown on the right whose Voronoi cell is the Brillouin zone of $\mathbf{L}$.

the construction to zonotopes that allows us to explicitly derive the sinc function for general lattices. The abstraction to zonotopes is also of interest for deriving complete interpolating sequences on Paley-Wiener spaces supported on bounded convex sets [9, 71].

2.2 Multidimensional Lattices

In this section we review the geometric aspects of multidimensional lattices that are relevant to their application in the context of sampling theory discussed later in Section 2.3.

2.2.1 Point Lattices

A point lattice is a discrete subgroup of the Euclidean space that includes the origin [96]. The set of points belonging to a lattice are closed under addition and negation. This implies that every lattice point has a neighborhood which contains all points to whom that lattice point is the closest lattice point. Such a neighborhood is defined as the Voronoi cell of a lattice point. Every lattice point is surrounded by congruent Voronoi cells of its neighbors. The Voronoi cell of a lattice is unique [19]; and is usually called the *fundamental domain* or *Wigner-Seitz cell* [96].

A lattice can be characterized by its **sampling matrix**, **L**, whose columns are a basis for the lattice. Every lattice point can be generated by integer linear combination of those column vectors. **L** is not unique for a given lattice. If both **L**' and **L** generate the same lattice, they are related via a unimodular matrix [112], **L**' $=$ **PL**, with $|\det \mathbf{P}| = 1$.

2.2.2 Dicing Lattices

A family of equally spaced (parallel) hyperplanes cuts the d-dimensional space, $\mathbb{R}^d$, into equi-thick bands (slabs). d such hyperplane families *dice* $\mathbb{R}^d$ into congruent parallelepipeds whose vertices form a d-dimensional "dicing" lattice. Generally, a **dicing** is an arrangement of N ($N \geq d$) such hyperplane families that are *non-degenerate* and *vertex regular*. Non-degeneracy of hyperplanes imply that d out of the N families must have linearly independent normal vectors and vertex regularity implies that there is one hyperplane from each family passing through each vertex of the dicing. See [46] for a more detailed presentation of dicing lattices.

2.2.3 Sphere Packing and Covering Lattices For Sampling

Similar to the distributional definition of comb (generalized) function, $\amalg_T$, one can introduce $\amalg_{\mathbf{L}}$ to model sampling of a multivariate signal with a lattice. The comb function associated with a lattice can be defined as:

$$\amalg_{\mathbf{L}} := \sum_{\mathbf{k} \in \mathbb{Z}^d} \delta(\cdot - \mathbf{L}\mathbf{k}),$$

which is formally defined as a distribution with the aid of test functions. The notion of the **reciprocal** (dual or polar) lattice appears when one considers the Fourier transform of $\amalg_{\mathbf{L}}$. The reciprocal lattice to a lattice **L** is generated by the columns of the matrix $\hat{\mathbf{L}} := \mathbf{L}^{-\top}$.

The (distributional) Fourier transform of $\amalg_{\mathbf{L}}$, is given by $1/|\det \mathbf{L}| \amalg_{\hat{\mathbf{L}}}$ [44]. Then using the multivariate Poisson sum formula we can observe that sampling a multidimensional signal on a lattice, generated by **L**, the spectrum of the signal is replicated on the reciprocal lattice $\hat{\mathbf{L}}$. **Brillouin zone** [96] is the unit cell of the dual lattice. The boundary

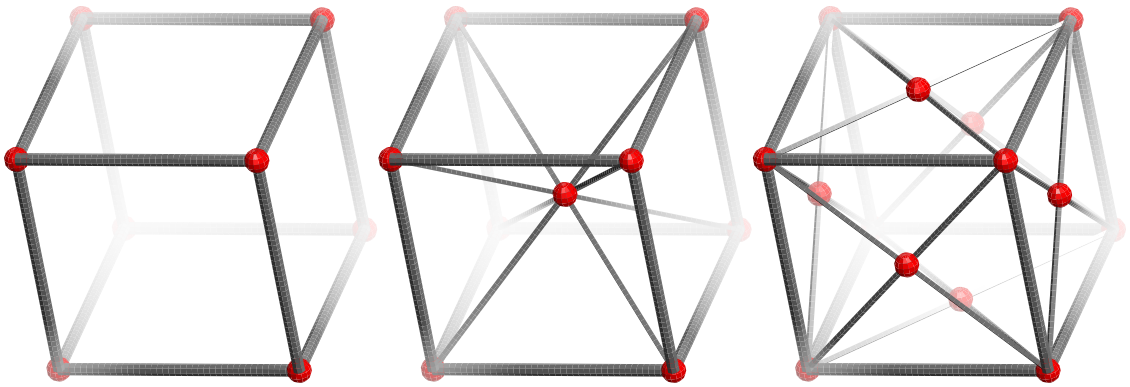

Figure 2-2. 3-D Cartesian, BCC and FCC lattices.

of Brilouin zone is the multidimensional counterpart to the Nyquist frequency for that specific multidimensional lattice.

For a low-pass bandlimited 1-D signal, the best sampling rate is determined by the supremum frequency of the signal's spectrum, which is called Nyquist frequency. In multidimensional cases, the term Nyquist frequencies is related to the geometry of the signal's spectrum. The *optimal sampling lattice* is optimal in the sense that once a signal is sampled on this lattice, its spectrum is periodically replicated and packed as densely as possible [41, 83, 91, 112]. So, the optimal sampling lattice for a specific signal is dependent on the geometry of its spectrum and can be computed if the geometric information is given [69]. On the other hand, without any prior geometric knowledge about the spectrum of the signal, *sphere packing and covering lattices* [30] outperform other lattices for sampling *generic* multidimensional signals. The reasoning is that without any prior information about the distribution of high-frequencies present in a signal, the best choice is to assume that they distribute equally along every direction and to isotropically preserve high frequencies as much as possible. According to such isotropic treatment, the best sampling lattice is determined by the the best sphere packing lattice in the frequency domain.

Because of the denser spectra packing in the frequency domain, the 2-D hexagonal lattice and its higher-dimensional counterparts require less number of samples than the Cartesian lattice to produce the alias-free sampling of generic signals [41, 83, 91, 112].

Compared to 3-D Cartesian lattice, the sampling efficiencies of the FCC and BCC lattices are 27% and 30% higher. Moreover, recent research shows that these lattices are more resilient to jitter noise in the sampling procedure [70]. This property makes them suitable alternatives for sampling operation in applications such as MRI [94]. In higher dimensional space, these lattices lead to more savings over the widely used Cartesian lattice. The sphere covering (e.g., BCC) lattice is the optimal choice to sample smooth and bandlimited signal while the sphere packing (e.g., FCC) lattice is the best choice for sampling non-smooth signals [48].

2.3 Sinc Functions On Multidimensional Lattices

As discussed in Section 2.2.3, sampling a multivariate signal f on the lattice $\mathbf{L}$, leads to periodic replication of the spectrum $\hat{f}$ on the reciprocal lattice $\hat{\mathbf{L}}$:

$$\amalg_{\mathbf{L}} f \Longleftrightarrow \frac{1}{|\det \mathbf{L}|} \amalg_{\hat{\mathbf{L}}} * \hat{f}$$
$$\sum_{\mathbf{k}\in\mathbb{Z}^d} \delta(\cdot - \mathbf{L}\mathbf{k}) f \Longleftrightarrow \frac{1}{|\det \mathbf{L}|} \sum_{\mathbf{k'}\in\mathbb{Z}^d} \hat{f}(\cdot - \hat{\mathbf{L}}\mathbf{k'}),$$

where $\Leftrightarrow$ indicates a Fourier transform pair.

The reconstruction formula needs to recover the spectrum by isolating the main period from the replica. Since the replication in the frequency space occurs on the reciprocal lattice, the fundamental domain of the reciprocal lattice (i.e., the Brillouin zone) identifies the main period that needs to be isolated for ideal bandlimited reconstruction. Therefore, the $\mathrm{sinc}_{\mathbf{L}}$ function on a lattice is defined as a function whose Fourier transform is the indicator function of the Brillouin zone of that lattice:

$$\mathrm{sinc}_{\mathbf{L}}(\mathbf{x}) := |\det \mathbf{L}| \int \chi_{\hat{\mathbf{L}}}(\mathbf{w}) \exp\left(2\pi i \left\langle \mathbf{x}, \boldsymbol{\omega} \right\rangle\right) \mathrm{d}\mathbf{w}, \tag{2–2}$$

where $\mathbf{x} := (x_1, \ldots, x_d)^T$ and $\boldsymbol{\omega} := (\omega_1, \ldots, \omega_d)^T$ denote the space and frequency domain variables, $\chi_{\hat{\mathbf{L}}}$ denotes the indicator function of the Voronoi cell of the lattice $\hat{\mathbf{L}}$ and $\langle , \rangle$

denotes the common inner product. Then the reconstructed function, f_r, is obtained by:

$$f_r = \mathrm{sinc}_{\mathbf{L}} * \mathrm{III}_{\mathbf{L}} f \iff \hat{f}_r = \chi_{\hat{\mathbb{L}}}\, \mathrm{III}_{\hat{\mathbf{L}}} * \hat{f}\ . \tag{2–3}$$

The convolution of the sampled function $\mathrm{III}_{\mathbf{L}} f$ with the $\mathrm{sinc}_{\mathbf{L}}$ leads to a linear combination of shifts of the $\mathrm{sinc}_{\mathbf{L}}$ function on the lattice **L**:

$$f_r = \sum_{\mathbf{k}\in\mathbb{Z}^d} f(\mathbf{Lk})\, \mathrm{sinc}_{\mathbf{L}}(\cdot - \mathbf{Lk}). \tag{2–4}$$

If f is bandlimited to the Brillouin zone, then $\hat{f}(\boldsymbol{\omega}) = 0$ for all $\boldsymbol{\omega}$ outside the Brillouin zone (i.e., when $\chi_{\hat{\mathbb{L}}}(\boldsymbol{\omega}) = 0$). Therefore the right hand side of (2–3) implies the perfect recovery of the bandlimited functions:

$$\hat{f}_r(\boldsymbol{\omega}) = \chi_{\hat{\mathbb{L}}}(\boldsymbol{\omega}) \sum_{\mathbf{k'}\in\mathbb{Z}^d} \hat{f}(\boldsymbol{\omega} - \hat{\mathbf{L}}\mathbf{k'}) = \hat{f}(\boldsymbol{\omega}). \tag{2–5}$$

The explicit derivation of $\mathrm{sinc}_{\mathbf{L}}$ for the Cartesian lattice is possible via the tensor product of the univariate sinc functions as the multivariate integral in (2–2) separates into a product of multiple univariate integrals; this is due to the separable geometry of the Brillouin zone of the Cartesian lattice which is a (hyper) cube. However, such derivation for non-Cartesian lattices is not possible since their Brillouin zones are not separable and integration in (2–2) does not lend itself to an easy derivation in the general setting.

Van De Ville et al. [113] derived the sinc function for the case of hexagonal lattice exploiting the 12-fold symmetry of the regular hexagon (i.e., the Brillouin zone). The derivation makes use of a function whose support is a cone in $\mathbb{R}^2$. A specific superposition of the cone function and a number of its rotations leads to the construction of the indicator function of a hexagon (i.e., $\chi_{\hat{\mathbb{L}}}(\boldsymbol{\omega})$) whose inverse Fourier transform is derived using the (distributional) inverse Fourier transform of the cone function. The application of this approach for general lattices becomes difficult as the choice of cone function and its superpositions and rotations becomes increasingly difficult for 2-D lattices without the 12-fold hexagonal symmetry or higher dimensional lattices.

On other hand, the Fourier transforms of the indicator functions of general polytopes can be derived using the divergence theorem [58, 69] in a recursive fashion. In contrast, our approach, which is specific to zonotopes, leads to a direct and explicit expansion in terms of sinc functions without any recursive terms. We exploit the geometric properties of zonotopes to derive the inverse Fourier transform of indicator functions of general zonotopes in *any* dimension. Lyubarskii and Rashkovskii [71] derived the complete interpolating sequences for functions whose Fourier transform is supported on symmetric polygons in $\mathbb{R}^2$. As we will see in what follows, symmetric polygons happen to be 2-D zonotopes and our geometric construction offers an explicit closed-form representation. While our proposed geometric construction is general for N-D zonotopes (not necessarily limited to lattices), we specifically focus on the case of Brillouin zones for *all* 2-D/3-D lattices and provide the recipes for higher dimensional lattices.

2.3.1 Zonotopes

A zonotope is a type of polytope that is obtained by projection of an N-dimensional hypercube to the d-dimensions ($N \geq d$). Let $\boldsymbol{\xi}_1, \dots, \boldsymbol{\xi}_N \in \mathbb{R}^d$ be a set of vectors that are obtained by a geometric projection of $\mathbf{e}_1, \dots, \mathbf{e}_N \in \mathbb{R}^N$ (i.e., edges of the unit hypercube in $\mathbb{R}^N$) down to $\mathbb{R}^d$. Then the zonotope is the convex polytope that is formed by the Minkowski sum of $\boldsymbol{\xi}$ vectors in $\mathbb{R}^d$. Hence, a zonotope, $\boldsymbol{\Xi}$, is uniquely identified by the (multi) set $\boldsymbol{\Xi} := [\boldsymbol{\xi}_1 \dots \boldsymbol{\xi}_N]$. The center of a zonotope is given by $\mathbf{c}_\Xi := \frac{1}{2}\sum_{n=1}^{N} \boldsymbol{\xi}_n$.

A zonotope together with all of its faces (any co-dimension) are symmetry with respect to their center points. One **zone** of a zonotope is defined as the set of all parallel edges of the zonotope [52]. A three-dimensional zonotope is often referred to as zonohedron. For instance, the elongated rhombic dodecahedron is a five-zone zonohedron. One of the zones is illustrated with red color in Figure 2-4. It turns out that a polyhedron is a zonohedron if and only if its faces are (center) symmetric [33]. The original motivation for studying zonohedra in geometry has been the fact that the Voronoi cells of any lattice are zonohedra [33].

The elements $\boldsymbol{\xi}$ in the set $\boldsymbol{\Xi}$ are vectors in $\mathbb{R}^d$ and a subset $\mathbf{B} \subset \boldsymbol{\Xi}$ is called a **basis** if the vectors in $\mathbf{B}$ are *minimally* spanning $\mathbb{R}^d$. The collection of all such bases of the zonotope is denoted by $\mathcal{B}(\boldsymbol{\Xi})$. A zonotope can be decomposed into a finite number of parallelepipeds formed by the vectors in each one of the bases in $\mathcal{B}(\boldsymbol{\Xi})$. This structure of zonotopes allows us to explicitly derive a function whose Fourier transform is the indicator function of a zonotope.

Theorem 2.1. *A zonotope, $\boldsymbol{\Xi}$, is the essentially disjoint union of (shifted) parallelepipeds each of which is formed by the vectors in a base of $\boldsymbol{\Xi}$. [34, I.53]*

Let χ denote the indicator function of the unit hypercube in $\mathbb{R}^d$. Then the indicator function of a parallelepiped formed by the Minkowski sum of the d vectors in $\mathbf{B}$, a base of the zonotope, is given by:

$$\chi_{\mathrm{B}} = \chi\left(\mathbf{B}^{-1}\cdot\right),$$

and its inverse Fourier transform is:

$$|\det \mathbf{B}| \prod_{\boldsymbol{\xi}\in\mathrm{B}} \frac{1-\exp\left(2\pi i \left\langle \boldsymbol{\xi}, \cdot \right\rangle\right)}{2\pi i \left\langle \boldsymbol{\xi}, \cdot \right\rangle} =$$
$$|\det \mathbf{B}| \exp\left(2\pi i \left\langle \mathbf{c}_{\mathrm{B}}, \cdot \right\rangle\right) \prod_{\boldsymbol{\xi}\in\mathrm{B}} \operatorname{sinc}\left\langle \boldsymbol{\xi}, \cdot \right\rangle \Longleftrightarrow \chi_{\mathrm{B}}$$

Here, $\mathbf{c}_{\mathrm{B}} := \frac{1}{2}\sum_{\boldsymbol{\xi}\in\mathrm{B}} \boldsymbol{\xi}$ denotes the phase-shift necessary to translate the parallelepiped so that its corner coincides with the origin. Then, according to Theorem 2.1, χ_{Ξ}, the indicator function of the zonotope, may be written as:

$$\chi_{\Xi} = \sum_{\mathrm{B}\in\mathcal{B}(\Xi)} \chi_{\mathrm{B}}(\cdot - \boldsymbol{\alpha}_{\mathrm{B}}), \tag{2–6}$$

where $\boldsymbol{\alpha}_{\mathrm{B}}$ is a translation associated to the base $\mathbf{B}$ in the parallelepiped decomposition of $\boldsymbol{\Xi}$. This translation is simply a sum of certain directions in the zonotope:

$$\boldsymbol{\alpha}_{\mathrm{B}} := \boldsymbol{\Xi}\delta_{\mathrm{B}}. \tag{2–7}$$

Here δ_{B} is a $N \times 1$ vector, associated with $\mathbf{B}$, whose elements are 0 or 1: $\delta_{\mathrm{B}} \in \{0,1\}^N$ [34]. The sum of two vectors $\boldsymbol{\alpha}_{\mathrm{B}}$ and $\mathbf{c}_{\mathrm{B}}$ translate the parallelepiped that corresponds to the base $\mathbf{B}$ to the appropriate location in the zonotope:

$$\boldsymbol{\tau}_{\mathrm{B}} = \boldsymbol{\alpha}_{\mathrm{B}} + \mathbf{c}_{\mathrm{B}} = \boldsymbol{\Xi}\left(\delta_{\mathrm{B}} + 1/2\right), \tag{2–8}$$

where $1/2$ is added to all elements of δ_{B} accounting for the center of the base, $\mathbf{c}_{\mathrm{B}}$.

With this parallelepiped decomposition, we can derive the inverse Fourier transform of the indicator function of a zonotope explicitly:

$$\sum_{\mathrm{B}\in\mathcal{B}(\Xi)} |\det \mathbf{B}| \exp\left(2\pi i \left\langle \boldsymbol{\tau}_{\mathrm{B}}, \cdot \right\rangle\right) \prod_{\boldsymbol{\xi}\in\mathrm{B}} \operatorname{sinc}\left\langle \boldsymbol{\xi}, \cdot \right\rangle \Leftrightarrow \chi_{\Xi} \tag{2–9}$$

2.3.2 Space Tesselations and Lattice Voronoi Polytopes

There are only a finite number of regular tesselations possible in any dimension. Therefore, various lattices can be categorized based on their Voronoi polytopes (cells) since the Voronoi cells translationally tile (tesselate) the space.

Theorem 2.2. *The Voronoi cell of any lattice is symmetric with respect to its center; moreover, all of its facets (i.e., faces of co-dimension 1) are centrally symmetric [40].*

The Voronoi cells of all 2-D or 3-D lattices are zonotopes [33]. More general, the Voronoi cells of all the higher dimensional lattices that satisfy the "Dicing" property are also zonotopes [46]. This topic is widely discussed in geometry and is closely related to the *Voronoi conjecture* [40, 74, 75].

Let $\boldsymbol{\Xi}^{\mathrm{L}}$ denote the zonotope that is congruent with the Brillouin zone of the lattice $\mathbf{L}$. Since a zonotope is not necessarily centered at the origin, and the Brillouin zone of a lattice is symmetric with respect to the origin, the zonotope needs to be translated to the origin by a translation $\mathbf{c}_{\Xi^{\mathrm{L}}}$:

$$\chi^{c}_{\Xi^{\mathrm{L}}} := \chi_{\Xi^{\mathrm{L}}}\left(\cdot - \mathbf{c}_{\Xi^{\mathrm{L}}}\right).$$

Then $\chi_{\mathbb{L}} = \chi^{c}_{\Xi^{\mathsf{L}}}$ which is symmetric with respect to the origin: $\chi_{\mathbb{L}}(\boldsymbol{\omega}) = \frac{1}{2}\left(\chi_{\mathbb{L}}(\boldsymbol{\omega}) + \chi_{\mathbb{L}}(-\boldsymbol{\omega})\right)$. Using (2–2) and (2–9), we have:

$$\begin{aligned}\mathrm{sinc}_{\mathsf{L}}(\mathbf{x}) =& |\det \mathbf{L}| \sum_{\mathsf{B}\in\mathcal{B}(\Xi^{\mathsf{L}})} |\det \mathbf{B}| \\ & \cos\left(2\pi \left\langle \boldsymbol{\tau}_{\mathsf{B}} - \mathbf{c}_{\Xi^{\mathsf{L}}}, \mathbf{x}\right\rangle\right) \prod_{\boldsymbol{\xi}\in\mathsf{B}} \mathrm{sinc}\left\langle \boldsymbol{\xi}, \mathbf{x}\right\rangle.\end{aligned} \tag{2–10}$$

Therefore, to determine the $\mathrm{sinc}_{\mathsf{L}}$ function for a lattice $\mathbf{L}$, one needs to consider the Brillouin zone as a zonotope. The bases of the zonotope $\mathcal{B}\left(\boldsymbol{\Xi}^{\mathsf{L}}\right)$ can be obtained by considering the full-rank subsets of the zones in the zonotope. The shifts $\mathbf{c}_{\mathsf{B}}$ for each base is determined by the center of that base, and the α_{B} translations are determined, geometrically or combinatorially, based on the $0/1$ vectors δ_{B}.

2.3.2.1 Two-Dimensional Lattices

Regular tesselation of the plane is only possible with equilateral triangles, squares and hexagons. The latter two tesselations are translational tilings of the plane and hence they characterize all 2-D lattices. In other words, the Voronoi cell of any 2-D lattice is combinatorially equivalent to a square or a hexagon (see Figure 2-1).

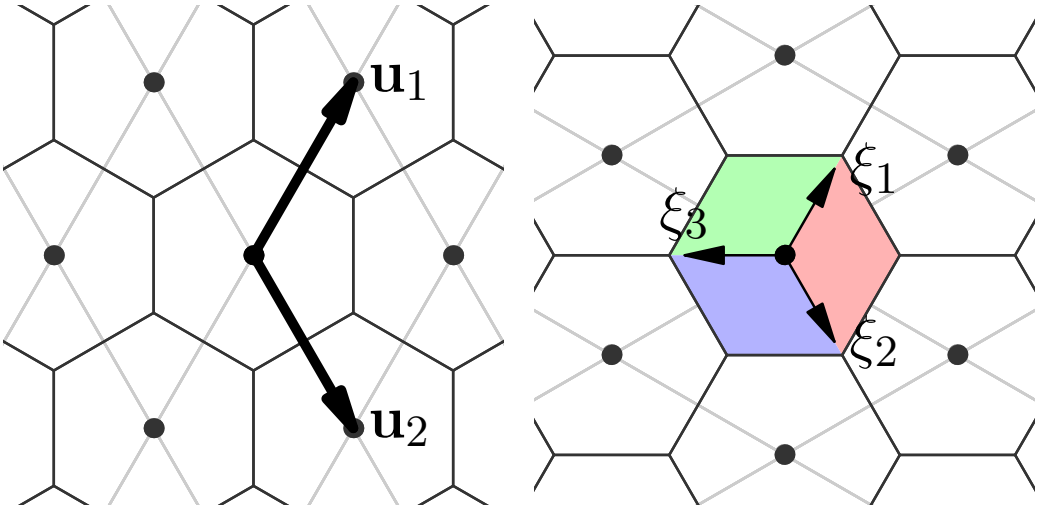

Figure 2-3. On the left: hexagonal lattice $\mathbf{L} = \mathbb{H}$. The Brillouin zone of the lattice $\mathbf{L}$ is illustrated on the right ($\chi_{\mathbb{L}} = \boldsymbol{\Xi}^{\mathsf{L}}$) that is a 3-zone zonogon with three bases.

The hexagon is a 3-zone zonogon and can be decomposed into three parallelepipeds. Figure 2-3 show such a decomposition for the Brillouin zone of a regular hexagonal lattice whose sampling matrix is:

$$\mathbb{H} = [\mathbf{u}_1, \mathbf{u}_2] = \frac{1}{2}\begin{bmatrix} 1 & 1 \\ \sqrt{3} & -\sqrt{3} \end{bmatrix}.$$

The Brillouin zone of this lattice is given by the following zonotope (illustrated in Figure 2-3 right):

$$\boldsymbol{\Xi}^{\mathbb{H}} = [\boldsymbol{\xi}_1, \boldsymbol{\xi}_2, \boldsymbol{\xi}_3] = \frac{2}{3}[\mathbf{u}_1, \mathbf{u}_2, -\mathbf{u}_1 - \mathbf{u}_2]. \tag{2–11}$$

The bases of this zonotope are:

$$\mathcal{B}\left(\boldsymbol{\Xi}^{\mathbb{H}}\right) = \{[\boldsymbol{\xi}_1, \boldsymbol{\xi}_2], [\boldsymbol{\xi}_1, \boldsymbol{\xi}_3], [\boldsymbol{\xi}_2, \boldsymbol{\xi}_3]\}.$$

As illustrated in Figure 2-3, the parallelepipeds forming the Brillouin zone are cornered at the origin and the translations $\boldsymbol{\alpha}_{\mathrm{B}} = 0$ for all bases. Hence, the $\mathrm{sinc}_{\mathbb{H}}$ for the hexagonal lattice can be written as:

$$\begin{aligned} \mathrm{sinc}_{\mathbb{H}}(\mathbf{x}) = & \\ & 1/3\cos\left(\pi\left\langle\boldsymbol{\xi}_3, \mathbf{x}\right\rangle\right)\mathrm{sinc}\left\langle\boldsymbol{\xi}_1, \mathbf{x}\right\rangle\mathrm{sinc}\left\langle\boldsymbol{\xi}_2, \mathbf{x}\right\rangle + \\ & 1/3\cos\left(\pi\left\langle\boldsymbol{\xi}_2, \mathbf{x}\right\rangle\right)\mathrm{sinc}\left\langle\boldsymbol{\xi}_1, \mathbf{x}\right\rangle\mathrm{sinc}\left\langle\boldsymbol{\xi}_3, \mathbf{x}\right\rangle + \\ & 1/3\cos\left(\pi\left\langle\boldsymbol{\xi}_1, \mathbf{x}\right\rangle\right)\mathrm{sinc}\left\langle\boldsymbol{\xi}_2, \mathbf{x}\right\rangle\mathrm{sinc}\left\langle\boldsymbol{\xi}_3, \mathbf{x}\right\rangle. \end{aligned} \tag{2–12}$$

The case of a generic 2-D lattice (Figure 2-1) follows similarly with the introduction of non-zero translations $\boldsymbol{\alpha}_{\mathrm{B}}$.

2.3.2.2 Three-Dimensional Lattices

3-D space can be translationally tiled by five combinatorially different polyhedra commonly referred to as the *Fedorov's parallelohedra* [96]. Cube is one of them, whose corresponding sinc function is precisely tensor-product of three 1-D sinc functions.
The Voronoi cells of FCC and BCC lattices are rhombic dodecahedron and truncated

octahedron as shown in Figure 2-4. The rest two tiling polyhedra, elongated rhombic dodecahedron and hexagonal prism, are Voronoi cells of elongated BCC and hexagonal lattices. These four types of Voronoi cells are zonohedra, so they can also be cut into parallelepipeds. The Voronoi cells of all the other non-Cartesian lattices in 3-D space are combinatorially equivalent to one of these four types. Hence, we provide a practical approach to construct sinc functions for *all* 3-D lattices. The cube is a zonohedron with 3 zones, rhombic dodecahedron and hexagonal prism have 4 zones, elongated rhombic dodecahedron has 5 zones and truncated octahedron has 6 zones. Since one zonotope can be converted to the other through setting the length of all the edges in one zone to zero, the truncated octahedron can be treated as the "most generic" zonohedron. Actually, the Voronoi cell of a "generic" 3-D lattice is combinatorially equivalent to the truncated octahedron [70]. The Voronoi cells of Cartesian, FCC, elongated BCC and hexagonal prism lattices are degenerate cases of the Voronoi cell of the BCC lattice (i.e., truncated octahedron).

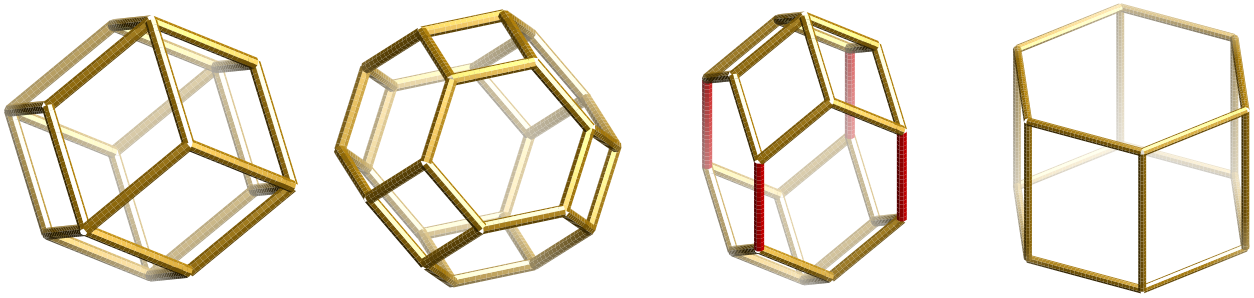

Figure 2-4. The fundamental domains of all 3-D lattices tessellate the space. (Left to right): Rhombic dodecahedron (FCC's Voronoi cell), truncated octahedron (BCC's Voronoi cell), elongated rhombic dodecahedron, and hexagonal prism. They all can be decomposed into paralleograms.

2.3.3 FCC and BCC Lattices

Since BCC and FCC lattices are of practical importance [42, 48, 51, 79, 102], we consider the explicit characterization of their sinc functions. The sampling lattices of BCC

Table 2-1. Decomposition of the Brillouin zone for the BCC lattice, $\Xi^{\mathbb{B}}$ used to construct the $\mathrm{sinc}_{\mathbb{B}}$.

$\mathcal{B}\left(\Xi^{\mathbb{B}}\right)$	Zones			δ_{B}			
$\mathbf{B}_1$	1	2	3	0	0	0	0
$\mathbf{B}_2$	1	2	4	0	0	0	0
$\mathbf{B}_3$	1	3	4	0	0	0	0
$\mathbf{B}_4$	2	3	4	0	0	0	0

and FCC are generated the columns of their respective matrices:

$$\mathbb{B} = \begin{bmatrix} -1 & 1 & 1 \\ 1 & -1 & 1 \\ 1 & 1 & -1 \end{bmatrix}, \mathbb{F} = \begin{bmatrix} 0 & 1 & 1 \\ 1 & 0 & 1 \\ 1 & 1 & 0 \end{bmatrix}. \tag{2–13}$$

The BCC and FCC lattices are reciprocal to each other; hence, the Voronoi cell of one serve as the Brillouin zone of the other. The Brillouin zone of the BCC lattice is a rhombic dodecahedron which is a 4-zone zonohedron:

$$\Xi^{\mathbb{B}} = [\xi_1 \dots \xi_4] = \frac{1}{4} \begin{bmatrix} 1 & -1 & -1 & 1 \\ -1 & 1 & -1 & 1 \\ -1 & -1 & 1 & 1 \end{bmatrix}. \tag{2–14}$$

All 3-subsets of zones in $\Xi^{\mathbb{B}}$ are full-rank and hence there are four bases in this zonotope. The α_{B} shifts are all zero since all of the parallelepipeds join at the origin as illustrated in Figure 2-5. The bases of this zonotope $\Xi^{\mathbb{B}}$ and the δ_{B} determining the translation vector are shown in Table 2-1. The $\mathrm{sinc}_{\mathbb{B}}$ for the BCC lattice directly from (2–10) and values in Table 2-1.

The Brillouin zone of the FCC lattice (i.e., truncated octahedron) is a 6-zone zonotope $\Xi^{\mathbb{F}}$:

$$\Xi^{\mathbb{F}} = [\xi_1 \dots \xi_6] = \frac{1}{4} \begin{bmatrix} 1 & -1 & 1 & 1 & 0 & 0 \\ 1 & 1 & 0 & 0 & 1 & -1 \\ 0 & 0 & 1 & -1 & 1 & 1 \end{bmatrix}. \tag{2–15}$$

Table 2-2. Decomposition of the Brillouin zone for the FCC lattice, $\Xi^{\mathbb{F}}$ used to construct the $\mathrm{sinc}_{\mathbb{F}}$.

$\mathcal{B}\left(\Xi^{\mathbb{F}}\right)$	Zones			δ_{B}					
$\mathbf{B}_1$	1	2	4	0	0	1	0	1	1
$\mathbf{B}_2$	1	5	6	0	0	1	1	0	0
$\mathbf{B}_3$	3	4	5	0	0	0	0	0	1
$\mathbf{B}_4$	2	3	4	0	0	0	0	1	1
$\mathbf{B}_5$	1	2	6	0	0	1	1	1	0
$\mathbf{B}_6$	3	5	6	0	0	0	1	0	0
$\mathbf{B}_7$	1	3	5	0	0	0	1	0	0
$\mathbf{B}_8$	1	4	6	0	1	1	0	1	0
$\mathbf{B}_9$	2	4	5	0	0	0	0	0	1
$\mathbf{B}_{10}$	1	2	3	0	0	0	1	1	0
$\mathbf{B}_{11}$	1	2	5	0	0	0	1	0	0
$\mathbf{B}_{12}$	4	5	6	0	1	0	0	0	0
$\mathbf{B}_{13}$	3	4	6	0	1	0	0	1	0
$\mathbf{B}_{14}$	2	5	6	0	0	0	1	0	0
$\mathbf{B}_{15}$	1	3	4	0	1	0	0	1	0
$\mathbf{B}_{16}$	2	3	6	0	0	0	1	1	0

Unlike the zones in $\Xi^{\mathbb{H}}$ or $\Xi^{\mathbb{B}}$, not every 3-subsets of zones in $\Xi^{\mathbb{F}}$ is a full-rank matrix. From the total of $\binom{6}{3} = 20$ choices of three-zone combinations, four of them are co-planar and hence do not form a 3-D parallelepiped. The truncated octahedron is decomposed into the remaining sixteen parallelepipeds which are shown in the second row of Figure 2-5. As we can see, since there is one parallelepiped centered at the origin, all the sixteen parallelepipeds have their corners off the origin. Therefore, the translations $\boldsymbol{\alpha}_{\mathrm{B}} \neq 0$ for all bases. The choices of the bases and the δ_{B} are shown in Table 2-2. Plugging the values in Table 2-2 into (2–10), we can get the $\mathrm{sinc}_{\mathbb{F}}$ for the FCC lattice directly.

2.3.4 Multivariate Shannon Wavelets

Non-separable wavelets in the multidimensions are difficult to come by [55]. The special 2-D examples [25, 27, 117], can not be generally extended to 3-D or higher dimensions for various lattices. However, the parallelepiped decomposition of general Brillouin zones of lattices, which was used for explicit derivation of sinc functions, leads

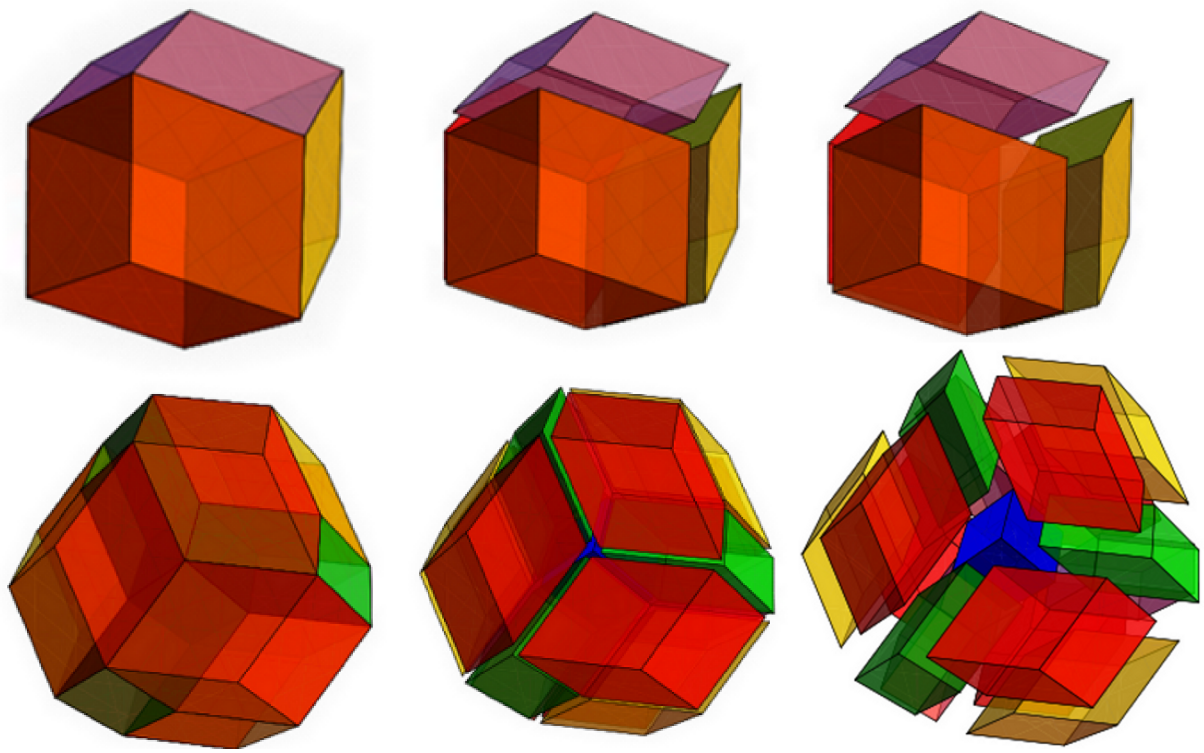

Figure 2-5. Top row: A rhombic dodecahedron (4-zones) can be divided into four 3-D parallelepipeds all joining the origin. Bottom row: Decomposition of a truncated octahedron (6-zones) into sixteen parallelepipeds.

to a frequency partitioning that leads to a wavelet-type decomposition based on scaled sinc_L functions. In the univariate setting, the Shannon wavelets [72], are obtained by using the sinc as the scaling function.

The main observation here is that the spectrum (i.e., Brillouin zone) of lattices are decomposed into parallelepipeds which lend themselves to a subdivision that partitions the spectrum, in a non-separable way, to low-bands and high-bands. The low-band frequencies from each parallelepiped form a self-similar Brillouin zone that can be recursively partitioned to lower-band frequencies, very similar to the 1-D filter-bank algorithms.

One step of the frequency partitioning is illustrated in Figure 2-6 that leads to a Brillouin zone of half the size. The sinc_L as a scaling function has a *multi-scale relationship* which is illustrated by the subdivision of parallelepipeds in Figure 2-6. The

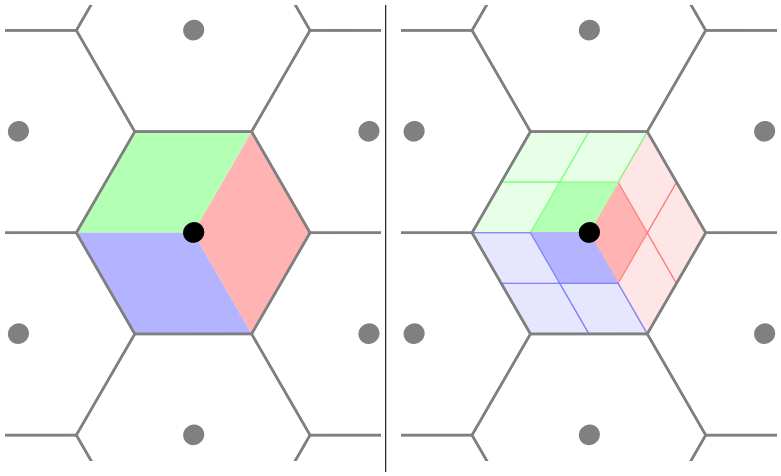

Figure 2-6. Brillouin zone from Figure 2-3, subdivided to derive a multi-scale function for Shannon wavelets. Low-frequency bands are indicated with darker colors.

hexagon after subdivision of parallelepipeds will build a smaller (centered) hexagon, on the right image, and this operation can be carried recursively. The spectrum of the Shannon 'mother' wavelet is composed of nine terms corresponding to the three (bright) high-pass sub-parallelepipeds for each parallelepiped in Figure 2-6(right).

One can also view each of the sub-parallelepipeds as a LH, HL, and HH partitions of the spectrum for each parallelepiped. The scaling function for Shannon wavelets on the hexagonal lattice will be the sum:

$$\varphi_{\mathrm{L}}^{\mathrm{Sh}}(\mathbf{x}) = \varphi_{\mathrm{red}}^{\mathrm{Sh}}(\mathbf{x}) + \varphi_{\mathrm{green}}^{\mathrm{Sh}}(\mathbf{x}) + \varphi_{\mathrm{blue}}^{\mathrm{Sh}}(\mathbf{x}), \tag{2–16}$$

where $\varphi_{\mathrm{red}}^{\mathrm{Sh}}$, similar to the other two, is constructed by a shear transformation, using $\boldsymbol{\xi}_1$, and $\boldsymbol{\xi}_2$ from a 2-D tensor-product sinc function.

2.3.5 Multivariate Lagrange Interpolant

The equivalence of sinc interpolation to Lagrange interpolation has been known as early as Borel [76]. Given an infinite number of equally spaced samples on the real line, the Lagrange basis polynomials converge to shifts of the sinc function.

$$\mathrm{sinc}(x) = \prod_{n \in \mathbb{Z} \setminus \{0\}} \left(1 - \frac{x}{n}\right) \tag{2–17}$$

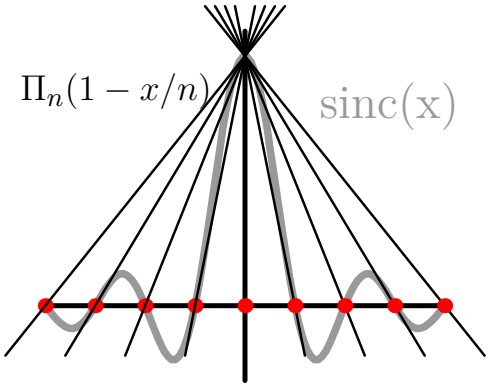

Figure 2-7. Lagrange basis for polynomial interpolation when the nodes are $\mathbb{Z}$ converges to sinc.

An argument for demonstrating the equivalence is that any analytic function is uniquely determined by its zeros and its value at one point. The sinc function and the right hand side of (2–17) cross zero on all integers except $x = 0$ where they are both equal to 1 (see also [93]).

The multivariate sinc functions discussed in Section 2.3.2 can not be directly related to a Lagrange type basis for interpolation. The product of sinc functions in (2–10) allow for a Lagrange-basis interpretation; the following remarkeable cosine expansion [1, p.85] allows us to write the $\mathrm{sinc}_{\mathbf{L}}$ as a sum of Lagrange-basis functions on the lattice **L**.

$$\begin{aligned}
\cos(x) &= \prod_{n=1}^{\infty}\left(1-\frac{x^2}{\pi^2(n-1/2)^2}\right)\\
\Rightarrow \cos(2\pi x) &= \prod_{n=1}^{\infty}\left(1-\frac{16x^2}{(2n-1)^2}\right)\\
&= \prod_{n=1}^{\infty}\left(1-\frac{4x}{2n-1}\right)\left(1+\frac{4x}{2n-1}\right)\\
&= \prod_{n\in\mathbb{Z}}\left(1-\frac{4x}{2n-1}\right).
\end{aligned} \tag{2–18}$$

Using (2–18) and (2–10) we can write the $\mathrm{sinc}_{\mathsf{L}}$ for a lattice $\mathbf{L}$ as a sum of Lagrange interpolants:

$$\begin{aligned}\mathrm{sinc}_{\mathsf{L}}(\mathbf{x}) = |\det \mathbf{L}| \sum_{\mathsf{B}\in\mathcal{B}(\Xi^{\mathsf{L}})} |\det \mathbf{B}| \left(1 + 4\left\langle \boldsymbol{\tau}_{\mathsf{B}} - \mathbf{c}_{\Xi^{\mathsf{L}}}, \mathbf{x}\right\rangle\right) \\ \prod_{n\in\mathbb{Z}\setminus\{0\}} \left(1 - \frac{4\left\langle \boldsymbol{\tau}_{\mathsf{B}} - \mathbf{c}_{\Xi^{\mathsf{L}}}, \mathbf{x}\right\rangle}{2n-1}\right) \prod_{\boldsymbol{\xi}\in\mathsf{B}} \left(1 - \frac{\langle \boldsymbol{\xi}, \mathbf{x}\rangle}{n}\right).\end{aligned} \tag{2–19}$$

2.3.6 Multidimensional Lanczos Windowing

The ideal interpolation, in the space of bandlimited functions, demands infinite computation since the support of the sinc function is unbounded. Truncating the sinc function, produces artifacts on the reconstructed function that is often referred as ringing. To minimize the ringing artifacts, there are a variety of windowing techniques in the univariate setting (such as Hamming, Parzen, Blackman [87]). In the multivariate setting, the problem is considerably more difficult and the non-separable multidimensional window functions are not well studied.

Radial extension of univariate windowing techniques (i.e., McClellan transform) provides an isotropic truncation of the sinc function which disregards the geometry of the lattice. Moreover, the isotropic windowing and truncation influence the frequency-space behavior of $\mathrm{sinc}_{\mathsf{L}}$ differently for each lattice and may lead to biases in one lattice over another. Tensor product of 1-D windows is only appropriate for the Cartesian lattice. Another approach is to design a discretized window for a separable (Cartesian) lattice, based on 1-D windows, and downsample to the desired lattice $\mathbf{L}$ [31]; however, this method may only be applied in the discrete setting utilizing a downsampling operation and can only approximate the true sinc function upto the level accommodated by the discretization resolution.

Among different univariate window design methods, the Lanczos window is uniquely suitable for the multivariate generalization as it picks the main lobe of the sinc function as a window. Also as we will see its frequency behavior is particularly suitable for this

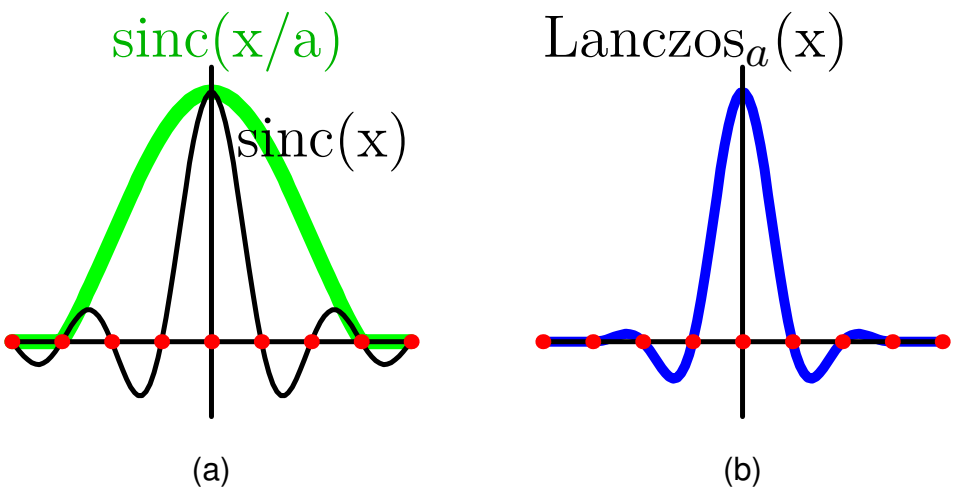

Figure 2-8. Lanczos filter as a multiplication with the main lobe of the scaled sinc function. (a) Main lobe of the scaled sinc function and original sinc functions. (b) Lanczos windowed sinc function.

generalization. The Lanczos window, also called sinc window, is essentially the central lobe of a scaled sinc function, $\mathrm{sinc}(x/a)$, restricted to the main period $-a \leq x \leq a$. Since the definition of the Lanczos window is purely determined by the sinc function, the multivariate Lanczos window is defined naturally on each lattice by the main lobe of its $\mathrm{sinc}_{\mathsf{L}}$. The boundary of the support of the window is the first zero level set of the corresponding $\mathrm{sinc}_{\mathsf{L}}$ function from the origin. This approach allows the window function to inherit the same anisotropic properties from the $\mathrm{sinc}_{\mathsf{L}}$ function. Moreover, it does not need special tailoring for different lattices which makes it an unbiased approach for multivariate window design.

Let $S\{\mathrm{sinc}_{\mathsf{L}}\}$ denote the support of the main lobe of $\mathrm{sinc}_{\mathsf{L}}$; the Lanczos windowed version of $\mathrm{sinc}_{\mathsf{L}}$ can be written as:

$$L_a(\mathbf{x}) = \begin{cases} \mathrm{sinc}_{\mathsf{L}}(\mathbf{x})\,\mathrm{sinc}_{\mathsf{L}}(\frac{\mathbf{x}}{a}), & \mathbf{x}/a \in S\{\mathrm{sinc}_{\mathsf{L}}\} \\ 0, & \text{otherwise.} \end{cases} \tag{2–20}$$

The scaling parameter a is picked as an integer value (usually 2 or 3 in 1-D applications [16]), and determines the size of the window.

The effect of Lanczos windowed sinc in the space domain is the increased smoothness of the truncated sinc while maintaining the interpolation property. For example, in 1-D case, the original sinc function and the main lobe of the scaled sinc function are illustrated as Figure 2-8 (a), while the Lanczos windowed sinc function, L_a, is shown as Figure 2-8 (b). The effect of Lanczos window in the frequency domain can be studied by considering the Fourier trasforms of $\mathrm{sinc}(x)$ and $\mathrm{sinc}(x/a)$ which are both box functions but with different widths. Since $\mathrm{sinc}(x/a)$ corresponds to a thinner box function ($a > 1$), the Fourier transform of the Lanczos windowed sinc is $\mathrm{box}(\omega)$ convolved by a thinner box function $|a|\mathrm{box}(a\omega)$. The convolution of these two rectangular functions results in a linear drop off of the transfer function with the increased support beyond the cut-off frequency. The effect in the frequency space is the increased continuity of $\mathrm{box}(\omega)$ from C^{-1} to C^0: while the original sinc filter's transfer function was a discontinuous box function, the transfer function of $\mathrm{sinc}(\omega)\,\mathrm{sinc}(\omega/a)$ has a linear drop off and is a continuous function.

Figure 2-9 illustrates the $\mathrm{sinc}_{\mathbb{H}}$ and its transfer function for hexagonal lattice, in the space and frequency domains. The transfer function of $\mathrm{sinc}_{\mathbb{H}}(\cdot/a)$, is related by a scaling (i.e., shrinked for $a > 1$) to that of $\mathrm{sinc}_{\mathbb{H}}$; hence we have:

$$\mathrm{sinc}_{\mathbb{H}}\,\mathrm{sinc}_{\mathbb{H}}(\cdot/a) \Longleftrightarrow a\chi_{\mathbb{H}} * \chi_{\mathbb{H}}(a\cdot). \tag{2–21}$$

The support of the convolution of the indicator functions of two polytopes is determined by the Minkowski sum of the two [21]. Therefore, the frequency support of the right hand side is determined by the Minkowski sum of the support of $\chi_{\mathbb{H}}$ and $\chi_{\mathbb{H}}(a\cdot)$. The support of the $\chi_{\mathbb{H}}$ and generally $\chi_{\mathbb{L}}$ is the Voronoi cell of the dual lattice and hence is a polytope that is convex and symmetric. Minkowski sum of a convex, symmetric, set containing the origin with a scaled version of itself enlarges that set by a factor of $1 + a$ [21]. Hence, the support is precisely determined by enlarging the Brillouin zone

by a factor of $1 + a$. Moreover, the multivariate convolution as in (2–21) increases the degree of continuity by 1 [82].

The increase in the continuity of the transfer function makes the truncation, in the space domain, less susceptible to the ringing phenomenon [65]. One can apply the window function several times to further reduce the ringing artifacts that are caused by truncation. In the space domain, the windowed-sinc function is given by:

$$L_a^n(\mathbf{x}) = \begin{cases} \mathrm{sinc}_{\mathsf{L}}(\mathbf{x})\,\mathrm{sinc}_{\mathsf{L}}^n(\frac{\mathbf{x}}{a}), & \mathbf{x}/a \in S\{\mathrm{sinc}_{\mathsf{L}}\} \\ 0, & \text{otherwise}. \end{cases} \tag{2–22}$$

The parameters n and a determine the smoothness and size of the kernel's support respectively. It is interesting to note that, unlike the multidimensional Cartesian setting, the Lanczos filter kernel in the non-separable setting has a support which is non-planar object (i.e., not a polytope in general). For example, the Lanczos window for hexagonal lattice has the shape with hexagonal symmetry but with curved faces (see the support in Figure 2-9 (c)).

2.4 Experimental Comparison

Optimal lattices such as hexagonal, BCC and FCC have been theoretically considered to be superior to the Cartesian lattice in the context of sampling theory [91]. However, for practical applications, the sampling operation together with the reconstruction step influence the signal quality. While there are several spline-type solutions for specific lattices [47, 60], the sinc functions offer a fair and unbiased framework for reconstruction across various sampling lattices. This framework allows us to examine the practical aspects of optimal sampling by employing the ideal interpolation scheme on each lattice for the purspose of signal reconstruction.

2.4.1 Experiments Setup

In order to show the results of the optimal sampling schemes compared to the common Cartesian scheme, we implemented a ray-caster [115] to render images from

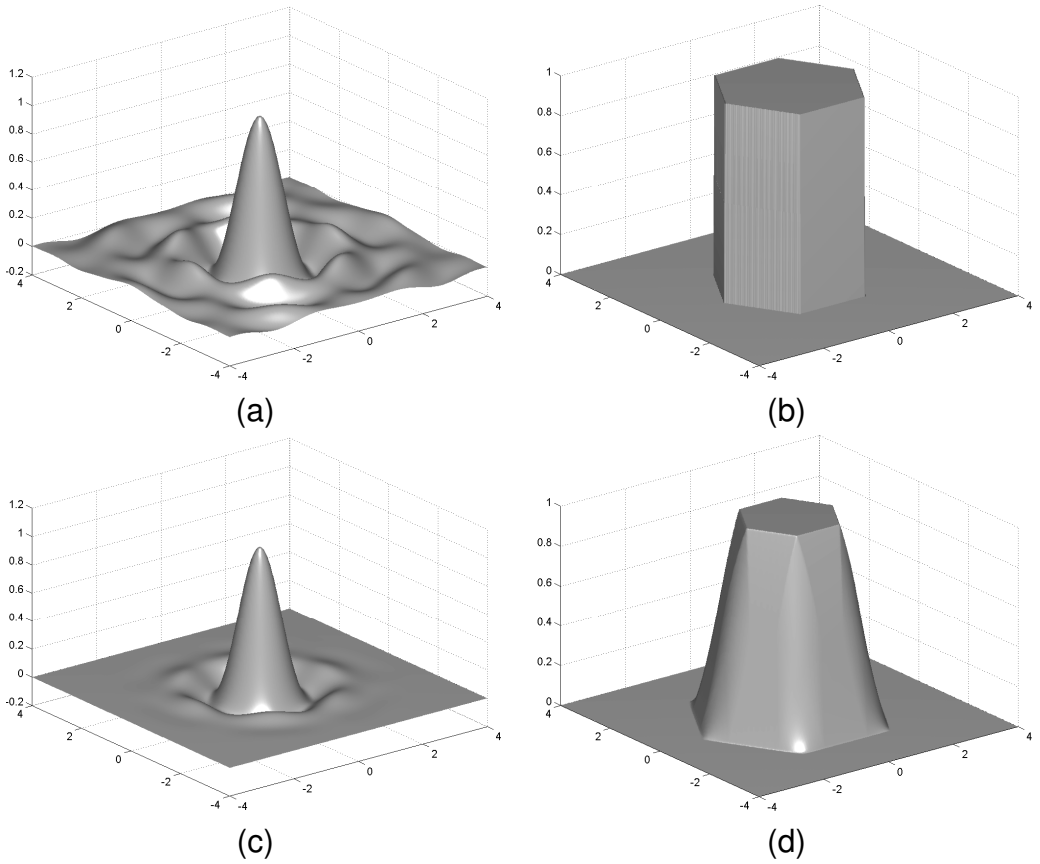

Figure 2-9. Plots of $\mathrm{sinc}_{\mathbb{H}}$ and its Lanczos windowed version in space (left column) and frequency (right column) domains. $\mathrm{sinc}_{\mathbb{H}}$ by itself in (a) space domain and (b) frequency domain. Lanczos windowed $\mathrm{sinc}_{\mathbb{H}}$ with $a = 4$ and $n = 2$ in (c) space domain and (d) frequency domain.

the reconstructed signal from BCC, FCC and Cartesian sampled volumetric datasets. The 3-D datasets consist of samples from a function $f(\mathbf{Lk})$ where $\mathbf{k} \in \mathbb{Z}^3$ and $\mathbf{L}$ is the sampling matrix. $\mathbf{L}$ is an identity matrix for Cartesian lattice, $\mathbb{B}$ and $\mathbb{F}$ as in (2–13) for BCC and FCC lattices. The reconstructed signal $\tilde{f}$:

$$\tilde{f} = f * \mathrm{sinc}_{\mathsf{L}} = \sum_{\mathsf{k} \in \mathbb{Z}^3} f(\mathbf{Lk}) \, \mathrm{sinc}_{\mathsf{L}}(\cdot - \mathbf{Lk}) \tag{2–23}$$

where the sinc function is windowed using (2–22) for practical implementation.

As a benchmark for comparison, we chose a frequency-modulation synthetic dataset called ML, shown as Figure 2-10 (a) which was first proposed by Marschner and Lobb [73]. The function was sampled at the "critical" resolution of $41 \times 41 \times 41$ on the

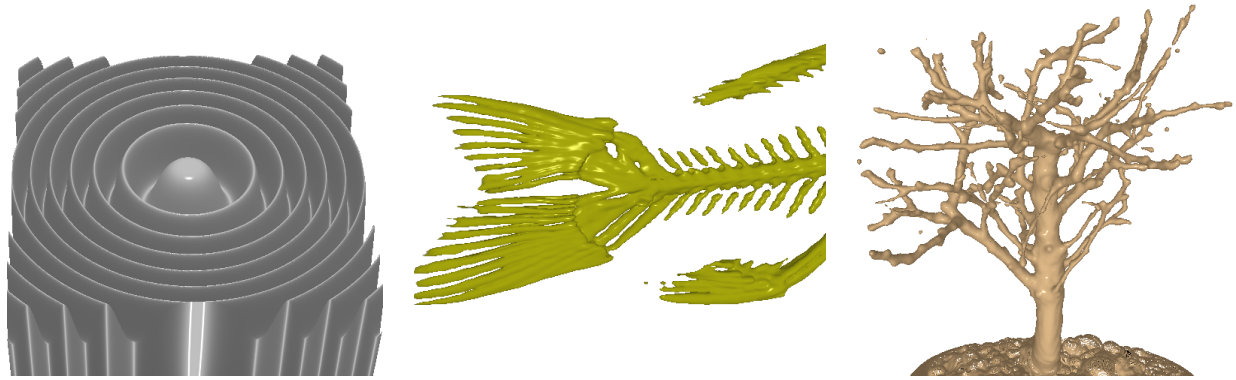

(a) (b) (c)

Figure 2-10. Benchmark volumetric datasets of (a) Marschner-Lobb, (b) carp fish and (c) bonsai tree.

Cartesian lattice, and equivalent sampling resolutions of $32 \times 32 \times 64$ on the BCC lattice and $25 \times 25 \times 100$ on the FCC lattice. The resolution of 41 was chosen as the critical resolution [73] because it captures 98% of the energy of the spectrum. So, it is treated as a practical Nyquist frequency for this non-bandlimited signal.

In addition to the synthetic ML dataset, we have further examined our scheme on real volumetric datasets of carp fish and bonsai tree shown as Figure 2-10 (b) and Figure 2-10 (c). Since there are no acquisition systems developed for BCC/FCC sampling, all the real-life datasets are scanned on Cartesian lattice. In order to test the reconstruction performance on the three lattices, we simulated three datasets through subsampling the original Cartesian datasets, that were densely sampled, onto low-resolution Cartesian, BCC and FCC lattices with almost identical densities. The original datasets were at the resolution of $256 \times 256 \times 256$ and were subsampled (to 16%) on Cartesian, BCC and FCC lattices with resolutions $140 \times 140 \times 140$, $111 \times 111 \times 222$ and $88 \times 88 \times 352$ respectively.

For the reconstruction kernel, we chose the second order, $n = 2$, Lanczos windowed sinc interpolant with scaling factor $a = 3$. We have verified in practice that this kernel

always covers approximately the same number of voxels in all the three lattices, which ensures the reconstruction from different lattices uses the same amount of information.

2.4.2 Visual Comparison

Figure 2-11 shows the rendered images from the ML dataset on different lattices. This experiment illustrates that the reconstruction from Cartesian lattice exhibits the strongest aliasing artifacts. Reconstructions from BCC and FCC lattices clearly outperform that from Cartesian lattice. The third row in Figure 2-11 shows the angular error which is the difference between the true normal and the reconstructed normal on the isosurface. The darker pixels denotes smaller error and the white pixels indicate the maximum angular error of 30 degrees. Again, we observe that BCC lattice produces smallest error while FCC lattice minimizes aliasing which matches the theoretical expectation [48].

Figure 2-12 and Figure 2-13 show the rendered images of carp fish and bonsai tree datasets from the three different lattices. We can observe that images rendered from BCC/FCC datasets always contains more details than those of the Cartesian datasets. The superiority of BCC/FCC datasets are mostly visible in tail fin and bones in the carp fish dataset and the connectivity of the branches in bonsai dataset.

2.4.3 Numerical Comparison

To perform a numerical error analysis of our reconstruction schemes, we estimated the root mean square (RMS) error (i.e., L_2) present in the reconstructed signal $\tilde{f}$, when compared with f. We could simply compare the numerical errors calculated from the same data volumes used previously for rendering. But we found it is more interesting to show how the resolution is influencing the error. We picked a Cartesian volume with a fixed resolution, e.g. $41 \times 41 \times 41$ for the ML dataset. We call this resolution "reference-resolution" and treat its number of sample points as our reference, named 100%. Then, we can characterize the resolution of a BCC/FCC data volume by the percentage ratio of its number of samples over the reference-resolution. For instance,

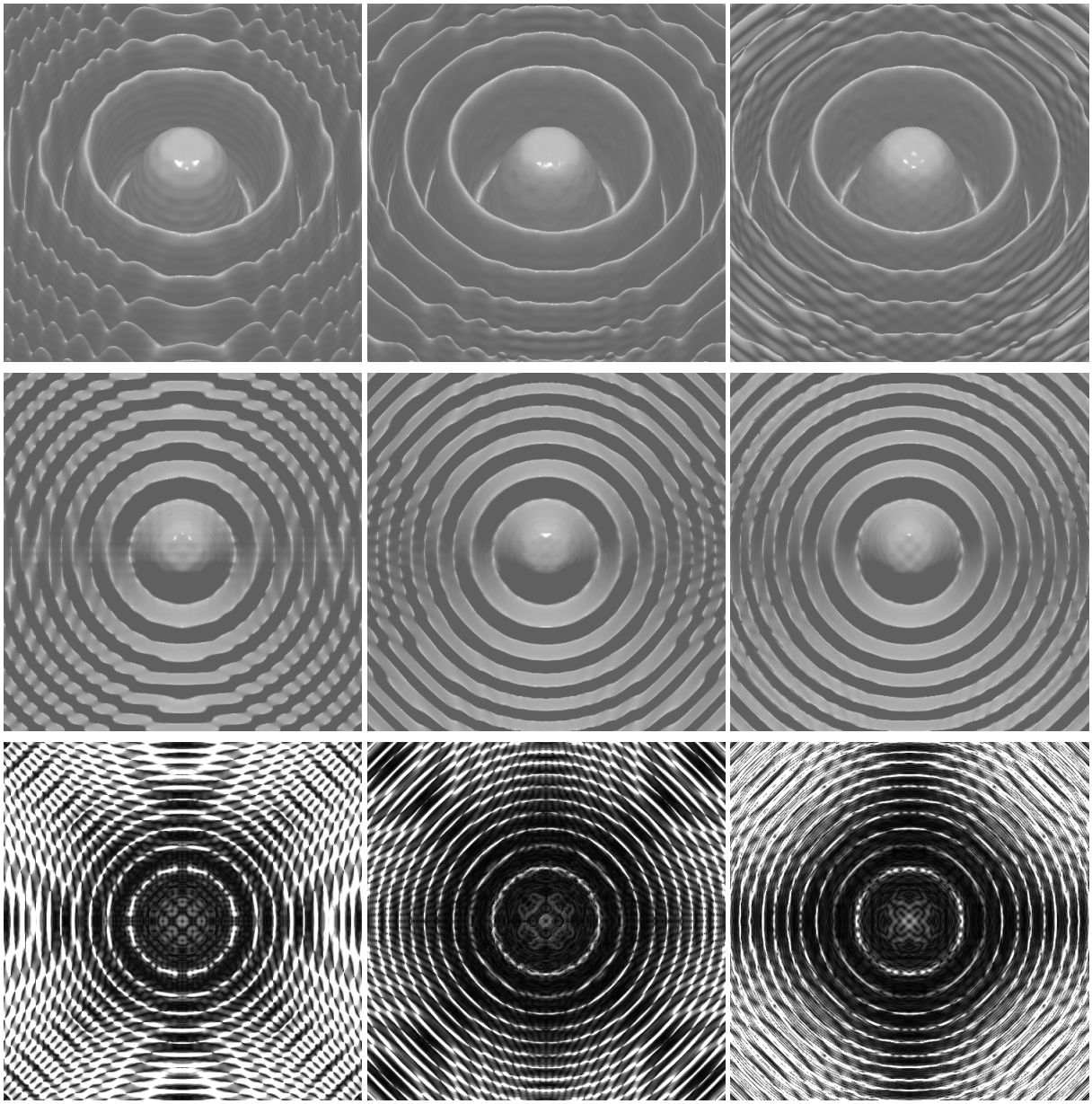

(a) (b) (c)

Figure 2-11. Visual comparison of images rendered from Cartesian, BCC and FCC lattices. ML isosurface image rendered from (a) Cartesian lattice, (b) BCC lattice and (c) FCC lattice. The third row shows the angular errors occurred in gradient estimation on the isosurface. Black indicates zero error and white denotes an angular error of 30 degrees.

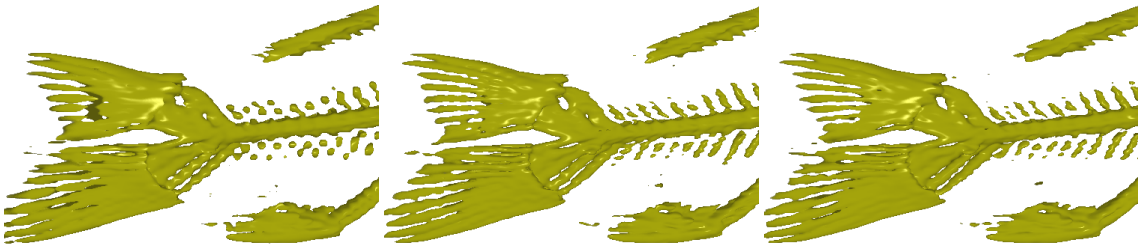

(a) (b) (c)

Figure 2-12. Visual comparison of images rendered from Cartesian, BCC and FCC lattices using Lanczos windowed sinc interpolants. Carp fish isosurface images rendered from (a) Cartesian lattice, (b) BCC lattice, (c) FCC lattice.

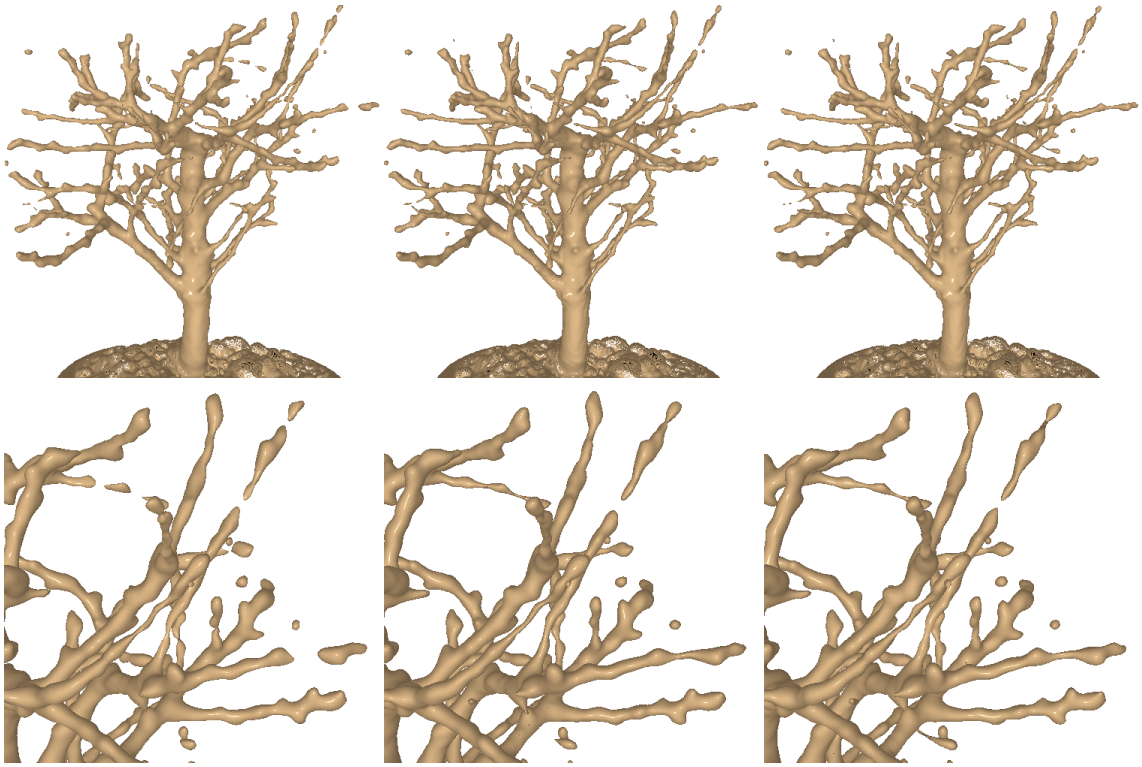

(a) (b) (c)

Figure 2-13. Visual comparison of images rendered from Cartesian, BCC and FCC lattices using Lanczos windowed sinc interpolants. Bonsai tree isosurface images rendered from (a) Cartesian lattice, (b) BCC lattice, (c) FCC lattice. The closeup views of the upper right corners are shown in the second row.

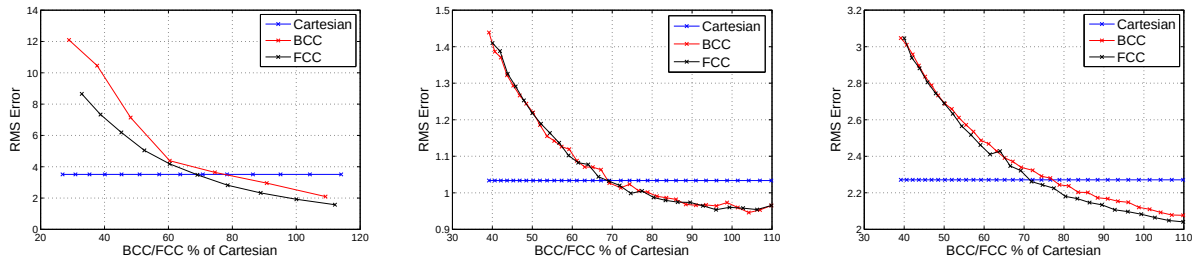

Figure 2-14. The RMS error comparison of BCC, FCC versus $41 \times 41 \times 41$ Cartesian lattice over (a) ML dataset (b) carp fish dataset and (c) bonsai tree dataset.

if we pick the $41 \times 41 \times 41$ Cartesian volume as the 100% reference-resolution, the 26.87% BCC volume has a resolution of $21 \times 21 \times 42$ and the 114.24% FCC volume has a resolution of $27 \times 27 \times 108$. For numerical comparison, we chose BCC/FCC volumes with resolution varying from around 30% to 115% and plotted their RMS errors as two curves. During the comparison, only one Cartesian volume with resolution 100% was used and its RMS error was plotted as a horizontal line considered the benchmark line. This benchmark line intersects the BCC error curve and FCC error curve respectively. These two intersection points tell us at what resolution the BCC/FCC volumes produce the same RMS error as the 100% Cartesian volume does.

Figure 2-14 (a) shows how the RMS error of BCC/FCC reconstructions on an ML data set varying with their resolutions. The reconstruction error from a $41 \times 41 \times 41$ Cartesian volume is plotted as the benchmark line. From the figure, we can see that the curve of BCC/FCC reconstruction error intersect the Cartesian benchmark line at around 70%. It means that we only need 70% sample points for BCC/FCC lattices, compared with Cartesian lattice, to achieve the same reconstruction accuracy. This matches the theorem precisely.

Finally, we show the numerical comparisons on RMS errors from carp fish and bonsai tree datasets as Figure 2-14 (b) and Figure 2-14 (c). $140 \times 140 \times 140$ Cartesian volumes were chosen as the 100% reference-resolution for both datasets. Since we do not have the true analytical function values to calculate the error, we use the interpolated

values from the original high-resolution data volume as the truth. These plots also show that we need around 70% number of samples to achieve the same reconstruction accuracy for BCC/FCC lattices.

CHAPTER 3
TOMOGRAPHIC RECONSTRUCTION OF DIFFUSION PROPAGATORS USING OPTIMAL SAMPLING LATTICES

This chapter exploits the power of optimal sampling lattices in tomography based reconstruction of the diffusion propagator. Optimal sampling leads to increased accuracy of the tomographic reconstruction approach introduced by Pickalov and Basser [92]. Alternatively, the optimal sampling geometry allows for further reducing the number of samples while maintaining the accuracy of reconstruction of the diffusion propagator. The optimality of the proposed sampling geometry comes from the information theoretic advantages of sphere packing lattices in sampling multidimensional signals. These advantages are in addition to those accrued from the use of the tomographic principle used here for reconstruction. We present comparative results of reconstructions of the diffusion propagator using the Cartesian and the optimal sampling geometry for synthetic and real data sets.

3.1 Motivations

In this chapter, we propose a model-free approach to reconstruction of the diffusion propagator at each voxel. The approach builds on the work in Pickalov and Basser [92], where in they exploit the Fourier transform relationship between $P(\mathbf{r})$ and $S(\mathbf{q})$ to develop a tomographic reconstruction of the propagator at each voxel. By interpolating a relatively small number of samples from the DW signal in the $\mathbf{q}$-space onto a regular grid, their approach allows for a tomographic reconstruction of $P(\mathbf{r})$ using the Fourier transform.

Since $P(\mathbf{r})$, at each voxel (tile), may contain anisotropic features in *any* arbitrary direction, it behooves us to choose a tiling of the space where each tile captures the maximum radial content of $P(\mathbf{r})$. Optimal tiling of the space results in voxels that admit a larger inscribing sphere compared to the traditional Cartesian tiling with cubic voxels. The main idea in this chapter exploits optimal tiling where each voxel is a rhombic dodecahedron and admits a larger inscribing sphere; hence, a better resolution of $P(\mathbf{r})$

(i.e., the one with a larger radius $\mathbf{r}$) is available with the same sampling density as with cubic Cartesian tiling. The rhombic dodecahedral tiling centers form the Face Centered Cubic (FCC) lattice which is the densest sphere packing lattice in 3-D. As we have seen in 2.2.1, this amounts to optimal sampling of the $\mathbf{q}$-space on a Body Centered Cubic (BCC) lattice which is the key contribution of our work.

The optimal sampling in $\mathbf{q}$-space allows us to achieve a better reconstruction due to significantly smaller ghosting effects in the reconstructed $P(\mathbf{r})$. When sampling $\mathbf{q}$-space $E(\mathbf{q})$ on a BCC lattice, the $P(\mathbf{r})$ is contained in rhombic dodecahedral voxels which admit a larger inscribing sphere than the commonly used Cartesian voxels. The inscribing sphere to the rhombic dodecahedral voxel is about 30% larger than that of the cubic voxel while the two voxels are of the same unit volume. Therefore, when reconstructing $P(\mathbf{r})$ on each individual voxel, a reconstruction based on BCC sampling of $\mathbf{q}$-space yield larger resolution of $\mathbf{r}$ while preventing the ghosting artifacts. The ghosting artifacts is the space-domain equivalent of aliasing. When sampling the $\mathbf{q}$-space signal in frequency space with a coarse sampling rate, the replicas in the space domain bleed into the main voxel area. For a given fixed sampling resolution in $\mathbf{q}$-space, the ghosting artifact is smaller for the rhombic dodecahedral voxel compared to the commonly-used cubic voxels.

Additionally, by using a significantly reduced sample set, we can maintain the same accuracy as one obtained using a Cartesian sampling lattice.

3.2 Algorithm and Implementation

The algorithm proposed by Pickalov and Basser [92] is a modified version of the iterative procedure presented by Gerchberg and Papoulis (G-P). They assume the original data samples lie on radial lines in $\mathbf{q}$-space. On each radial line, several samples are available corresponding to different radii. Using an interpolator/extrapolator, they obtain the data values on a Cartesian lattice in the $\mathbf{q}$-space. By imposing some constrains both in the $\mathbf{q}$-space and displacement probability space, their algorithm runs

iteratively via the use of direct and inverse Fourier transforms. In each iteration, the original sampled data is imposed into the $\mathbf{q}$-space values to reinforce the consistency between the reconstructed $P(\mathbf{r})$ and the true diffusion propagators implied by the data samples.

As we saw in 2.2.1, we can increase the accuracy of reconstruction by changing the $\mathbf{q}$-space sampling from the Cartesian lattice to the BCC lattice. Therefore, we push the radially sampled data, on to the BCC lattice together with an approach similar to the algorithm of Pickalov and Basser. Since our purpose is to investigate the theoretical advantages of the optimal lattice, we took the same radial samples from $E(\mathbf{q})$ and pushed them into both Cartesian and BCC lattices with the same number of lattice points. While there are several esoteric interpolation methods [47] for interpolation into the BCC and Cartesian lattices, we used an identical interpolant in both cases to ensure that the only difference in the two reconstructions is the sampling geometry. Therefore, we used a cubic spline interpolant in both cases, even though in our experiments, other interpolants resulted in similar results.

After the Cartesian and BCC re-sampling of the $\mathbf{q}$-space data, the $P(\mathbf{r})$ reconstruction is obtained through a direct Fourier transform. While the usual FFT algorithm is suitable for Cartesian sampling, the we employed the modified FFT algorithm [5] for the BCC sampled data. In order to evaluate our method the accuracy of reconstruction in each case was measured by comparing the reconstructed signal from the true synthetic signal by the means of sum of squared errors (SSE). For the synthetic data some visual comparison is insightful and discussed in 3.3.

3.3 Algorithm Evaluation

We now present propagator reconstruction experiments using the BCC and Cartesian lattices in a synthetic dataset (Figure 3-1) and a real dataset (Figure 3-2) from a rat optic chiasm.

Table 3-1. SSE comparison of reconstructions from different lattices with N_r, $N_\theta = 12$, $N_\phi = 13$, $\alpha = 90°$

N_r	10	9	8	7	6
Cartesian($\times 10^{-5}$)	2.19	2.31	2.63	3.34	4.04
BCC($\times 10^{-5}$)	0.60	0.68	0.87	1.38	2.56

Table 3-2. SSE comparison of reconstructions from different lattices with N_θ, N_ϕ, $N_r = 10$,$\alpha = 90°$

N_θ, N_ϕ	12,13	11,12	10,11	9,10	8,9
Cartesian($\times 10^{-5}$)	2.19	3.91	6.67	5.40	3.36
BCC($\times 10^{-5}$)	0.60	1.37	3.83	2.81	2.97

For our synthetic data experiments, we generated samples from a mixture of two Gaussian functions in the 3-D $\mathbf{q}$-space and examined the SSE between reconstructions and the true signal. In the experiments, data samples are distributed on radial lines along (r, θ, ϕ) in the spherical coordinate system. The number of samples along each radial line is denoted by N_r, of θ values by N_θ, and the ϕ values by N_ϕ respectively. α denotes the angle between the two Gaussian components.

Table 3-1 reports the SSE differences between the BCC and Cartesian reconstructions with fixed $\alpha = 90°$ and varying N_r. It is evident from the errors that the BCC-based reconstruction yields smaller errors despite the same sampling rate N_r as in the Cartesian-based reconstruction; this remains to be the case even for varying sampling resolutions. Similarly by changing the sampling resolutions in N_θ and N_ϕ, the advantages of BCC reconstruction is maintained (see Table 3-2). Table 3-3 depicts the comparison between BCC and Cartesian reconstructions by varying the angle between the two Gaussian components simulating various angles of fiber-crossings. Table 3-4 compares

Table 3-3. SSE comparison of reconstructions from different lattices with α, $N_r = 10$, $N_\theta = 12$, $N_\phi = 13$

α	90°	80°	70°	60°	50°
Cartesian($\times 10^{-5}$)	2.19	3.75	4.16	4.04	2.92
BCC($\times 10^{-5}$)	0.60	1.05	1.60	2.09	1.69

Table 3-4. SSE comparison of reconstructions from different lattices with σ, $N_r = 10$, $N_\theta = 12$, $N_\phi = 13$, $\alpha = 90$

σ	0	0.02	0.04	0.06	0.08
Cartesian($\times 10^{-5}$)	2.19	2.57	3.51	4.79	6.78
BCC($\times 10^{-5}$)	0.60	1.05	2.31	3.84	6.28

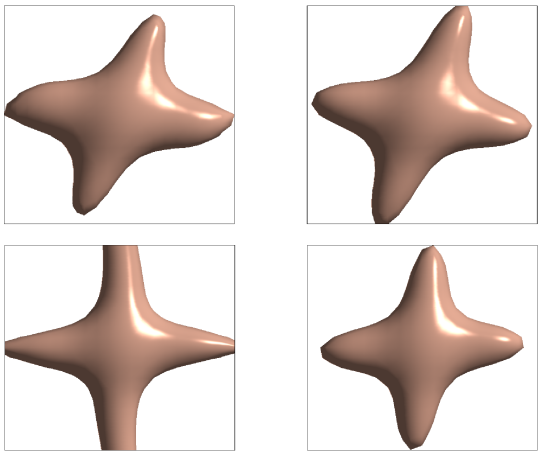

Cartesian BCC

Figure 3-1. Visual comparison of the reconstructed $P(\mathbf{r})$. Row 1: $(\theta_1, \theta_2) = (20°, 100°)$, Row 2:$(\theta_1, \theta_2) = (5°, 85°)$. ($\theta_1$,$\theta_2$) are the directions of the two Gaussian components.

the reconstructions under Rician noise of different noise levels σ. We can clearly see that under all the test conditions, reconstructions from BCC lattice achieve smaller errors compared to reconstructions from the Cartesian lattice. Also, Table 3-1 and Table 3-2 show that a reconstruction based on a smaller number of BCC samples (e.g., $N_r = 6$) in the $\mathbf{q}$-space is comparable to a reconstruction with larger number of Cartesian samples (e.g., $N_r = 8$) in the q-space. This suggests a strategy to further reduce the sample size of $E(\mathbf{q})$ and reduce the acquisition time.

For $N_r = 10$, $N_\theta = 12$, $N_\phi = 13$, $\alpha = 80$ and $\sigma = 0$, Figure 3-1 shows the isosurfaces of the reconstructed $P(\mathbf{r})$ from Cartesian and BCC lattices respectively. We can see that the isosurface of $P(\mathbf{r})$ from Cartesian lattice exhibits some ghosting artifacts at the tips due to leakage from ghosts in the neighboring period. The reconstruction from BCC lattice is not influenced by the ghosting artifacts since when we take samples on

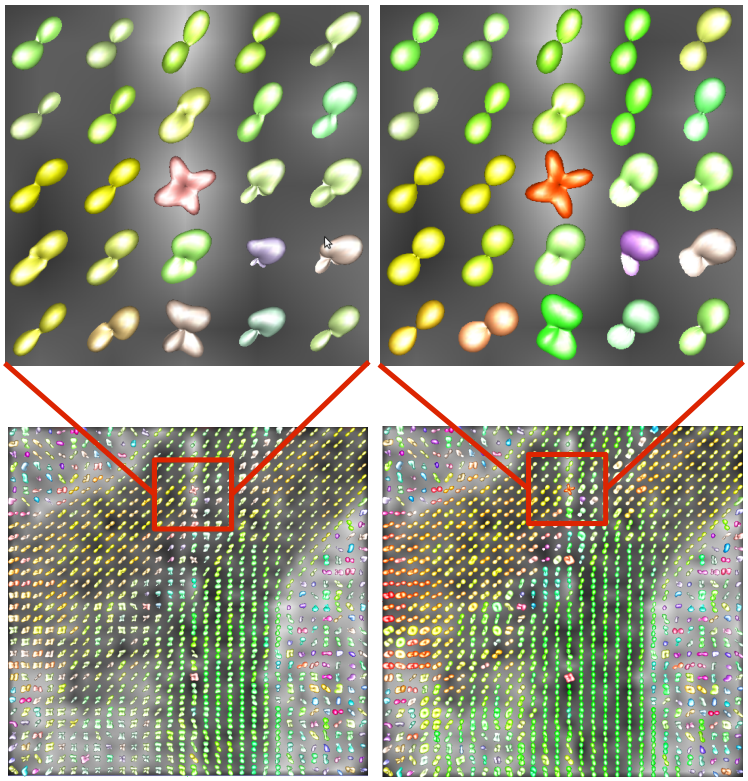

(a) (b)

Figure 3-2. Probability maps reconstructed from real data set: (a) from Cartesian lattice, (b) from BCC lattice.

BCC lattice in $\mathbf{q}$-space, the distance between the reconstructed $P(\mathbf{r})$ and its nearest ghost replica is larger than that derived from Cartesian lattice. Theoretically, the larger distance implies less influence from the ghost replica.

We now present an experiment with real data from a rat optic chiasm, which contains samples measured with 46 different directions with just one b value. Since our algorithm needs samples with different b values, for interpolation purposes, we used the high rank tensor model in [10] to process the data and get the values for different bs via re-sampling. Figure 3-2 depicts the probability maps reconstructed from the Cartesian and BCC lattices respectively. A close examination depicts that the reconstruction from Cartesian lattice appears distorted compared to the BCC reconstruction. This is due to the resilience of the BCC sampling (of $\mathbf{q}$-space) to the ghosting artifacts that distort the reconstruction of $P(\mathbf{r})$.

CHAPTER 4
RECONSTRUCTION FROM INTERLACED SAMPLING

In Chapter 3, we have shown that for the same sampling pattern, using the BCC lattice instead of Cartesian lattice in the tomographic reconstruction framework can increase the reconstruction accuracy through suppressing the ghosting phenomenon. In this chapter, we are introducing an interlaced sampling scheme as an superior alternate to the standard multi-shell scheme.

In standard multi-shell sampling scheme, sample points are uniformly distributed on several concentric spherical shells in the $\mathbf{q}$ space. This distribution does not change through different shells and is determined by the vertices of certain polyhedron. Actually, this is not the most efficient way of distributing sample points. We propose an interlaced scheme where sample points are placed on vertices of a pair of dual polyhedra on the consecutive shells. Specifically, we use rhombic triacontahedron on odd shells and icosidodecahedron on even shells. This scheme increases the angular discrimination because it indeed samples more directions than the standard scheme. Together with the sampling scheme, reconstruction algorithms using the lattice dependent sinc interpolants are introduced. Samples measured in interlaced multi-shell pattern are re-sampled (interpolated) onto the dense regular lattices, Caretesian or BCC. The diagram is shown in Figure 4-1. The sampling scheme and reconstruction algorithms were evaluated on both synthetic dataset and rat brain data collected from a $600MHz$ (14.1 Tesla) Bruker imaging spectrometer.

4.1 Interlaced Sampling Scheme

In this work, we propose an interlaced sampling scheme as an alternative to the standard multi-shell sampling scheme. The idea of interlaced lattice comes from the structure of the BCC lattice as it can be viewed as a stack of 2-D Cartesian layers of points where every alternate layer is shifted by half of the sampling distance (in the 2-D plane). In the multi-shell sampling, the proposed interlaced lattice has the interleaving

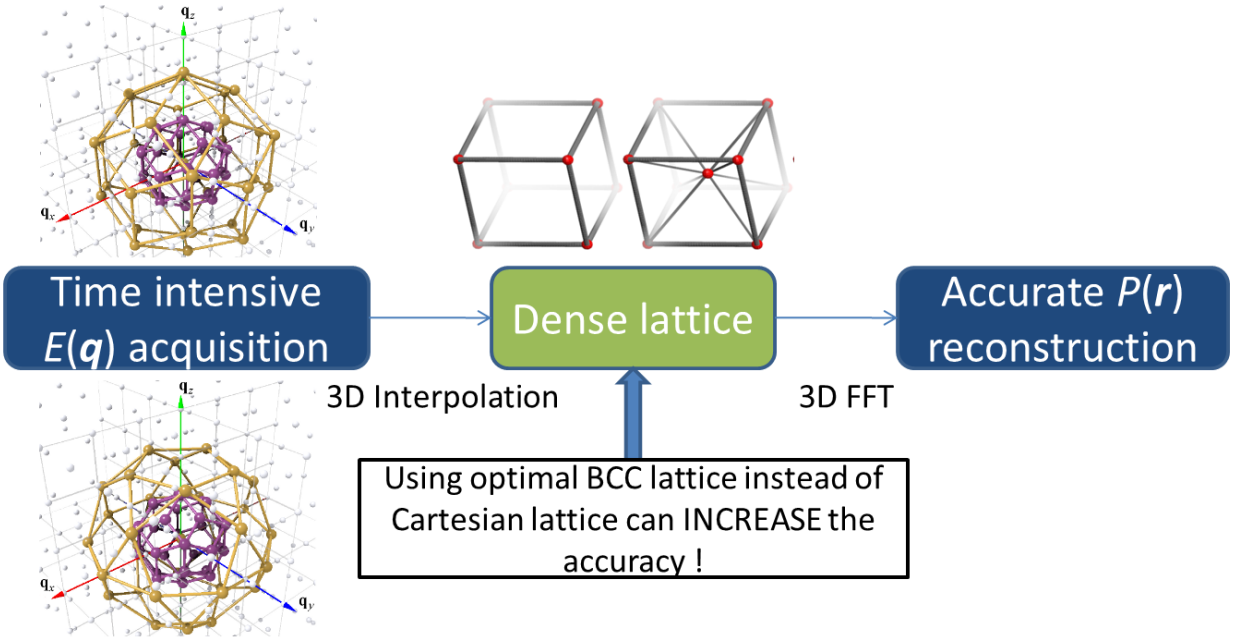

Figure 4-1. Diagram of the reconstruction process. The multi-shell diffusion signal acquisition scheme can be standard (top) or interlaced (bottom). The dense lattice can be Cartesian or BCC.

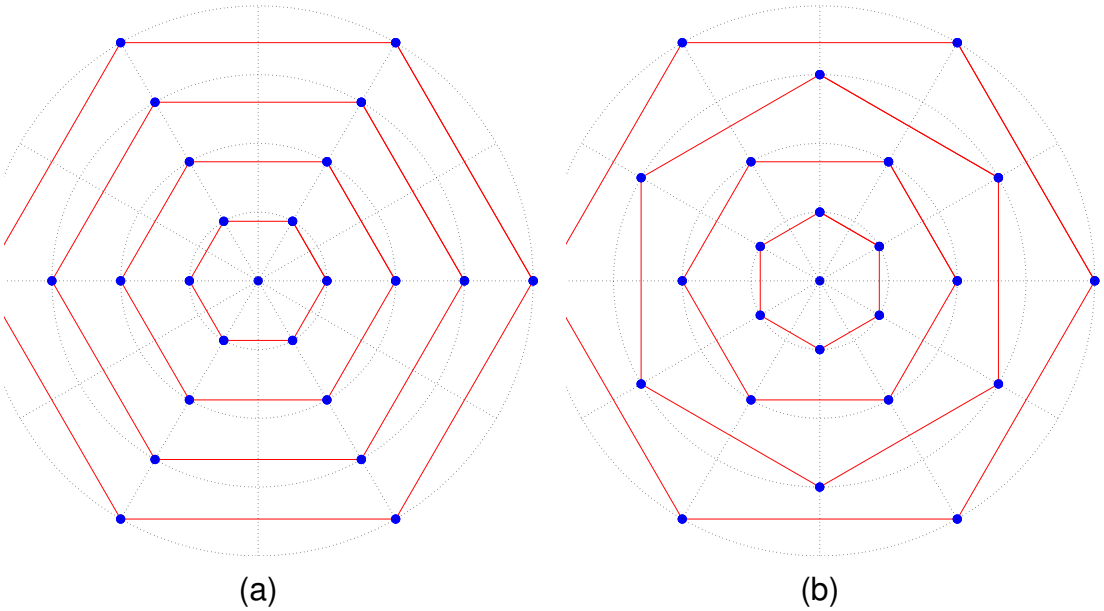

Figure 4-2. Comparison of 2D (a) standard and (b) interlaced sampling schemes in the case of CT reconstruction

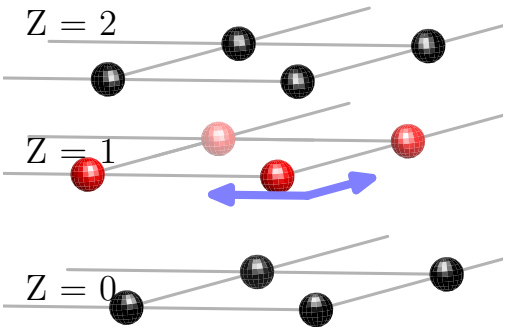

Figure 4-3. The structure of BCC lattice as 2-D Cartesian layers of samples *shifted* on alternate Z slices.

structure in the spherical coordinates where every alternate shell is shifted by half of the angular resolution. A similar idea in 2-D interlaced sampling has been explored for computed tomography [49] which compared the performance of an interlaced sampling scheme with the standard scheme in the case of 2-D computed tomography (CT) reconstruction. For their interlaced scheme, the detector array was shifted by one half of a detector spacing when going from one projection direction to the next. With some good experimental results, this work concluded that the interlaced scheme allows almost twice the resolution of the standard scheme with the same number of samples in 2-D. Figure 4-2 shows the sample distributions of both schemes. In the interlaced scheme, samples on the odd and even circles form two different polygons. These two polygons are a pair of dual polygons where the vertices of one correspond to the edges of the other.

By extending the idea of dual polygons to dual polyhedra (the vertices of one correspond to the *faces* of the other), we produced a three-dimensional interlaced sampling scheme. To ensure that samples are uniformly distributed on each spherical shell, one could use the sampling directions defined by the vertices of the commonly-used icosahedron (Figure 4-4(a)) and its dual, the dodecahedron (Figure 4-4(b)), alternately for odd and even shells. Icosahedron and dodecahedron are both Platonic solids, i.e. convex regular polyhedrons, which are highly symmetrical, being edge-transitive, vertex-transitive and face-transitive. This property makes them suitable choices as the

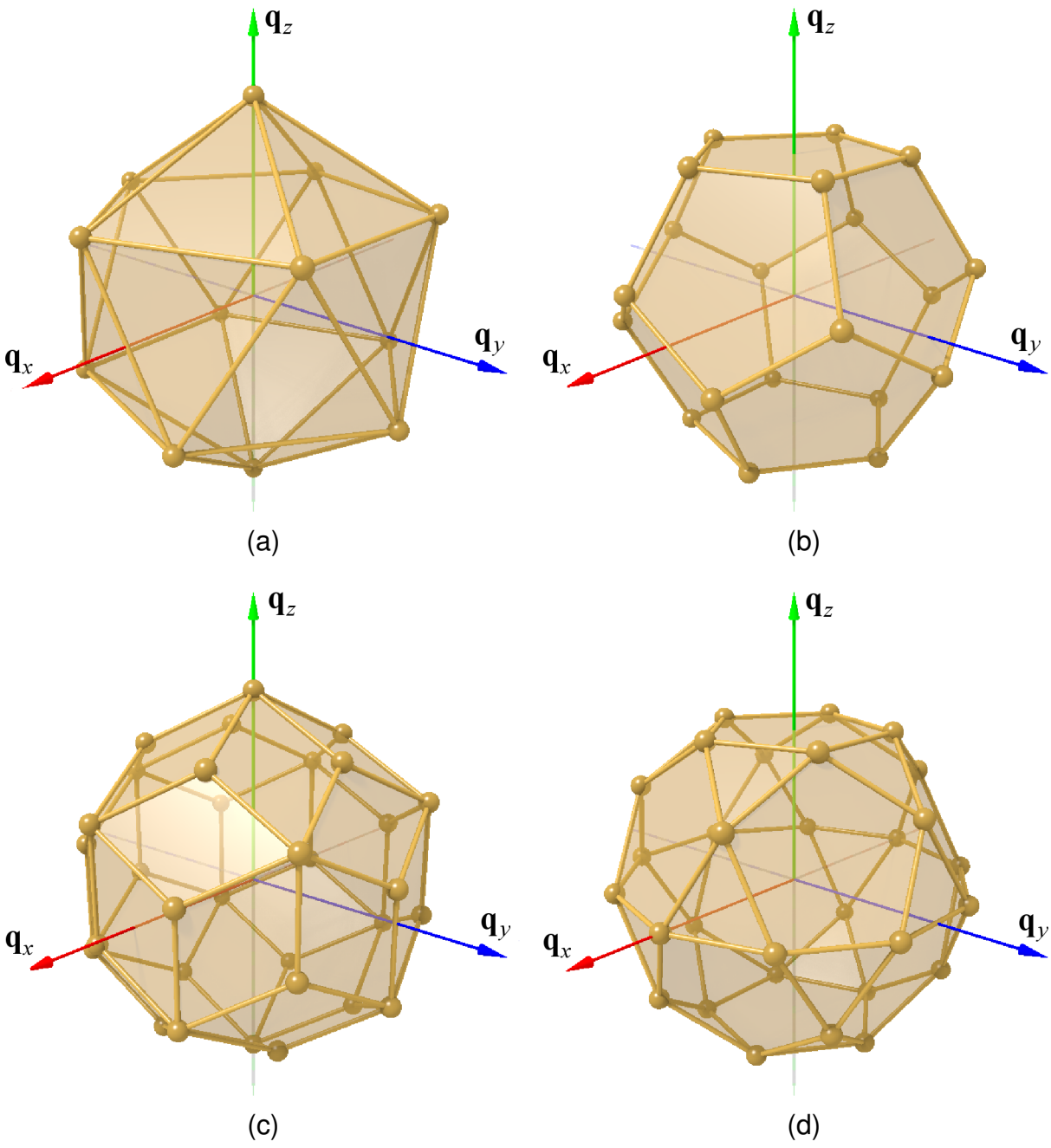

Figure 4-4. Shape of polyhedra used in this scheme. (a) Icosahedron, 12 vertices, 30 edges, 20 faces, (b) Dodecahedron, 20 vertices, 30 edges, 12 faces, (c) Rhombic triacontahedron, 32 vertices, 60 edges, 30 faces, (d) Icosidodecahedron, 30 vertices, 60 edges, 32 faces.

generators of sampling directions. However, the dodecahedron has 20 vertices while the icosahedron has 12. Therefore, an interlaced sampling scheme based on these two polyhedra would have either greater or fewer samples than a standard multi-shell scheme of comparable sample size. This imbalance makes the comparison of the two approaches difficult.

For a fairer comparison, we used an interlaced scheme based on another pair of dual polyhedra: the rhombic triacontahedron (Figure 4-4(c)) and icosidodecahedron (Figure 4-4(d)) who have about the same number of vertices (32 and 30). The vertex directions of the rhombic triacontahedron and icosidodecahedron determined the sampling directions for odd and even shells, respectively. In the standard scheme, all shells were sampled using the vertex directions of the rhombic triacontahedron. Since a rhombic triacontahedron has 32 vertices and the icosidodecahedron has only 30, the interlaced scheme uses slightly fewer samples than the standard scheme. In the experiments section we will see that, even with fewer samples, the interlaced scheme achieves better reconstruction accuracy. If necessary, more sampling directions can be added by subdividing the edges of both polyhedra.

4.2 Reconstruction Algorithm

In Section 4.1, we proposed the use of an interlaced multi-shell sampling scheme to sample the diffusion signal in $\mathbf{q}$-space. This is not a uniform sampling scheme, so we cannot estimate the diffusion propagator directly through FFT. One solution is to estimate the values of $P(\mathbf{r})$ by numerically computing the integral in (1–1). However, the irregular distribution of sampling positions makes it difficult to design an accurate numerical integration algorithm. Another solution is to define a regular lattice in $\mathbf{q}$-space and estimate the values on this regular lattice through interpolation/extrapolation.
In other words, we can resample the diffusion signal on a regular lattice using the nonuniformly sampled values.

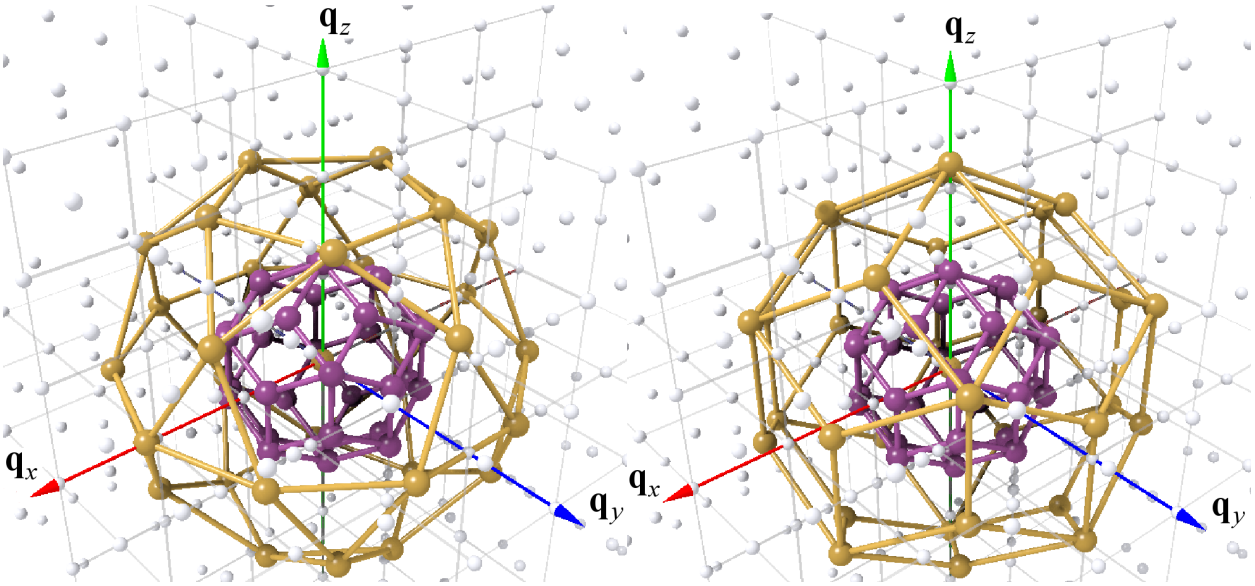

(a) (b)

Figure 4-5. (a) Interlaced multi-shell sampling directions defined on rhombic triacontahedron (purple) and icosidodecahedron (copper) in an alternative manner. (b) Standard multi-shell sampling directions defined on rhombic triacontahedron over all the shells. Rhombic triacontahedron has 32 vertices, 60 edges and 30 faces. Icosidodecahedron has 30 vertices, 60 edges and 32 faces.

Shannon's sampling theory provides a reconstruction formula for a bandlimited function, f, from its samples on a uniform lattice, $\mathcal{L}$, when the sampling rate is higher than the Nyquist frequency of f:

$$f(\mathbf{x}) = \sum_{\mathbf{x}_k \in \mathcal{L}} f(\mathbf{x}_k)\, \mathrm{sinc}_{\mathcal{L}}(\mathbf{x} - \mathbf{x}_k) \tag{4–1}$$

$\mathrm{sinc}_{\mathcal{L}}(\mathbf{x})$ is the ideal interpolation function that depends on the sampling lattice $\mathcal{L}$. In the 3-D Cartesian lattice case, $\mathrm{sinc}_{\mathcal{L}}(\mathbf{x})$ is the tensor product of three 1-D sinc functions defined as:

$$\mathrm{sinc}_{\mathcal{L}}(\mathbf{x}) = \frac{\sin(\pi x)}{\pi x}\frac{\sin(\pi y)}{\pi y}\frac{\sin(\pi z)}{\pi z}. \tag{4–2}$$

(4–2) can be computed from the inverse Fourier transform of the indicator function of the Brillouin zone – a cube for Cartesian lattice.

For the BCC lattice, the corresponding $\text{sinc}_{\mathcal{L}}$ is computed, similarly, from the inverse Fourier transform of the indicator function of its Brillouin zone – a rhombic dodecahedron as shown in Figure 2-4. This function can be efficiently evaluated using a geometric approach [120]. The explicit formula for BCC lattice's sinc function is given by:

$$\text{sinc}_{\mathcal{L}}(\mathbf{x}) = \frac{1}{4}\sum_{k=1}^{4}[\cos(\pi\xi_k^T\mathbf{x})\prod_{m\neq k}\text{sinc}(\xi_m^T\mathbf{x})] \tag{4–3}$$

where

$$[\boldsymbol{\xi}_1 \dots \boldsymbol{\xi}_4] = \frac{1}{4}\begin{bmatrix} 1 & -1 & -1 & 1 \\ -1 & 1 & -1 & 1 \\ -1 & -1 & 1 & 1 \end{bmatrix}. \tag{4–4}$$

See (2–10) in 2.3 for details of the derivation.

Shannon's reconstruction formula (e.g., (4–1)) involves infinitely many terms, which make its evaluation impractical. In practice, only finite terms involving lattice points, $\mathbf{x}_k$, within a bounding box are considered non-zero. While only finite terms are considered in the summation, the linear combination of $\text{sinc}_{\mathcal{L}}$ shifted to these finite lattice points provides an infinitely-supported approximation to f:

$$\hat{f}(\mathbf{x}) = \sum_{\mathrm{x}_k\in\boldsymbol{\mathcal{L}},1\leq k\leq K} f(\mathbf{x}_k)\,\text{sinc}_{\mathcal{L}}(\mathbf{x}-\mathbf{x}_k). \tag{4–5}$$

The inverse Fourier transform of this approximation has a compact support which will approximate $P(\mathbf{r})$ in our setting. In our case, the signal under investigation is the diffusion signal $E(\mathbf{q})$ in $\mathbf{q}$-space. We are given N sample measurements $E(\mathbf{q}_n)$ on multiple spherical shells, depicted by copper and purple vertices in Figure 4-5 (a) and Figure 4-5 (b). The desired estimates are K values $E(\mathbf{x}_k)$ on a regular lattice $\mathbf{x}_k \in \boldsymbol{\mathcal{L}}$, depicted by gray dots in Figure 4-5 (a) and Figure 4-5 (b) for the Cartesian case. The diffusion signal can be approximated according to equation (4–5) as $\hat{E}(\mathbf{q})$. By matching

$\hat{E}(\mathbf{q})$ to the measurements $E(\mathbf{q}_n)$ at locations $\mathbf{q}_n$, we get:

$$E(\mathbf{q}_n) = \sum_{x_k \in \boldsymbol{\mathcal{L}}, 1 \leq k \leq K} E(\mathbf{x}_k)\, \mathrm{sinc}_{\boldsymbol{\mathcal{L}}}(\mathbf{q}_n - \mathbf{x}_k),\ n = 1, 2, \ldots, N \tag{4–6}$$

where N is the total number of measurements of $E(\mathbf{q})$. Considering $E(\mathbf{x}_k)$ as unknowns, (4–6) are N equations in K unknowns which can be written as a linear system $\mathbf{Ae} = \mathbf{b}$, where $\mathbf{A}_{n,k} = \mathrm{sinc}_{\boldsymbol{\mathcal{L}}}(\mathbf{q}_n - \mathbf{x}_k)$, $\mathbf{e}_k = E(\mathbf{x}_k)$ and $\mathbf{b}_n = E(\mathbf{q}_n)$.

For accurate lattice-based reconstruction, the regular lattice should be dense, so we usually have $K > N$. $K \leq N$ means that the number of $\mathbf{q}$-space measurements is higher than the lattice resolution that we are reconstructing onto. Since the acquisition time is determined by N, a high sampling rate (e.g., DSI) is impractical. Therefore, we consider $K > N$ that our reconstruction lattice more dense compared to the acquired sampling rate. This means that (4–6) is an underdetermined linear system which can be solved in the least-squares sense using normal equations and the conjugate gradient method. To expedite the process, we provide an initial estimate of $E(\mathbf{x}_k)$ using linear interpolation on a Delaunay triangulation of a set of sample points $\mathbf{q}_n$, $n = 1, 2, \ldots N$. One can also obtain solutions with different properties through replacing the L_2 norm with other norms. For example, using L_1 norm on some transform coefficients of leads to sparse reconstructions as discussed in [23, 77, 78].

Once the signal $E(\mathbf{q}_n)$ has been the estimated on a regular lattice, we get a continuous representation of $E(\mathbf{q})$ as:

$$E(\mathbf{q}) = \sum_{x_k \in \boldsymbol{\mathcal{L}}, 1 \leq k \leq K} E(\mathbf{x}_k)\, \mathrm{sinc}_{\boldsymbol{\mathcal{L}}}(\mathbf{q} - \mathbf{x}_k) \tag{4–7}$$

Taking Fourier transform on (4–7), we get:

$$P(\mathbf{r}) = \mathrm{box}(\mathbf{r}) \sum_{x_k \in \boldsymbol{\mathcal{L}}, 1 \leq k \leq K} E(\mathbf{x}_k) \exp(-2\pi i \mathbf{x}_k \cdot \mathbf{r}) \tag{4–8}$$

where $\mathrm{box}(\mathbf{r})$ is the Fourier transform of $\mathrm{sinc}_{\boldsymbol{\mathcal{L}}}(\mathbf{q})$ which is an indicator function whose support is a cube for Cartesian lattice and a rhombic dodecahedron for BCC lattice.

As discussed in Section 2.2.3, to capture the same amount of information about the function being sampled, the BCC lattice only needs about 70% of the sample points needed for the Cartesian lattice. This property makes the necessary K value for the BCC lattice 30% smaller than the K value for the Cartesian lattice. For solving the underdetermined linear system, smaller K is preferred, because it means that the linear system has a higher rank. This usually translates to smaller uncertainty in the final solution. On the other hand, for a fixed K value, resampling on a BCC lattice can reveal more details about the real signal by allowing $P(\mathbf{r})$ reconstructed by a larger radius while avoiding the ghosting effects. In other words, resampling on a BCC lattice is an effective way of improving the accuracy without increasing the rank of the linear system to be solved.

4.3 Experiments

In this section, we present several experimental results on synthetic as well as real data sets. First, the synthetic data examples are presented followed by the real data experiments.

4.3.1 Experiments on synthetic data

In order to show the advantages of our sampling scheme and lattice selection, we first did quantitative comparison using synthetic data. We used a mixture of two oriented Gaussian functions in the 3-D displacement space to simulate the diffusion probability of a fiber crossing. The two Gaussian functions are the rotated versions of an oriented Gaussian distribution function with zero mean and diagonal covariance matrix $\mathbf{C} = diag\{20, 20, 400\}$ which has a fractional anisotropy value of 0.95. These two rotated Gaussian functions can be specified by its covariance matrices $\mathbf{C}_1$ and $\mathbf{C}_2$. The diffusion propagator, $P(\mathbf{r})$, and diffusion signal, $E(\mathbf{q})$, can then be defined analytically:

$$P(\mathbf{r}) = \frac{1}{2}\frac{1}{(2\pi)^{3/2}}\left[\frac{\exp\left(-\frac{1}{2}\mathbf{r}^T\mathbf{C}_1^{-1}\mathbf{r}\right)}{\sqrt{\det \mathbf{C}_1}} + \frac{\exp\left(-\frac{1}{2}\mathbf{r}^T\mathbf{C}_2^{-1}\mathbf{r}\right)}{\sqrt{\det \mathbf{C}_2}}\right] \tag{4–9}$$

$$E(\mathbf{q}) = \frac{1}{2}\left[\exp\left(-2\pi^2\mathbf{q}^T\mathbf{C}_1\mathbf{q}\right) + \exp\left(-2\pi^2\mathbf{q}^T\mathbf{C}_2\mathbf{q}\right)\right] \quad (4\text{–}10)$$

We fixed one of the Gaussian components and rotate the other component to form crossing angles from 20° to 60° with a 5° step size.

As described earlier, $\mathbf{q}$-space data was sampled on multiple shells using both the standard and interlaced schemes. For the standard scheme, the vertex directions of the rhombic triacontahedron defined the sampling directions for all shells. For the interlaced scheme, diffusion directions on even shells were determined from the vertices of the icosidodecahedron. Due to the symmetry of the diffusion signal, i.e. $S(\mathbf{q}) = S(-\mathbf{q})$, only half of the sampling directions are necessary. Thus, only those directions with $\mathbf{q}_z \geq 0$ were chosen. The sampling directions are summarized (in polar coordinates) in Table 4-1. The Cartesian coordinates can be calculated as $x = \sin(\theta)\cos(\phi)$, $y = \sin(\theta)\sin(\phi)$ and $z = \cos(\theta)$

For the synthetic experiments, we picked 7 different shell radii uniformly distributed between 0 and $q_{max} = 0.5\sqrt{1/20}$. So we had samples on 6 shells plus the origin. The total number of samples was 193 for the standard scheme and 187 for the interlaced scheme, symmetric directions included. The data were interpolated onto two embedding lattices: the $15 \times 15 \times 15$ Cartesian lattice and the equivalent BCC lattice, which consists of two interlaced Cartesian lattices of size $11 \times 11 \times 11$ and $12 \times 12 \times 12$. The numbers of lattice points were 3375 for Cartesian and 3059 for BCC.

The reconstructed diffusion propagators, $P(\mathbf{r})$ at different $||\mathbf{r}||$ values, obtained using different sampling schemes and embedding lattices are shown as Figure 4-6. We can see that the interlaced sampling scheme has higher angular discrimination than the standard scheme. In the interlaced sampling case, the two-fiber crossing geometry is correctly reconstructed when the crossing angle is greater than or equal to 35°. In the standard case, the crossing geometry is not reconstructed until 45°. Also, the reconstructions from interlaced scheme are sharper and of higher fidelity with respect

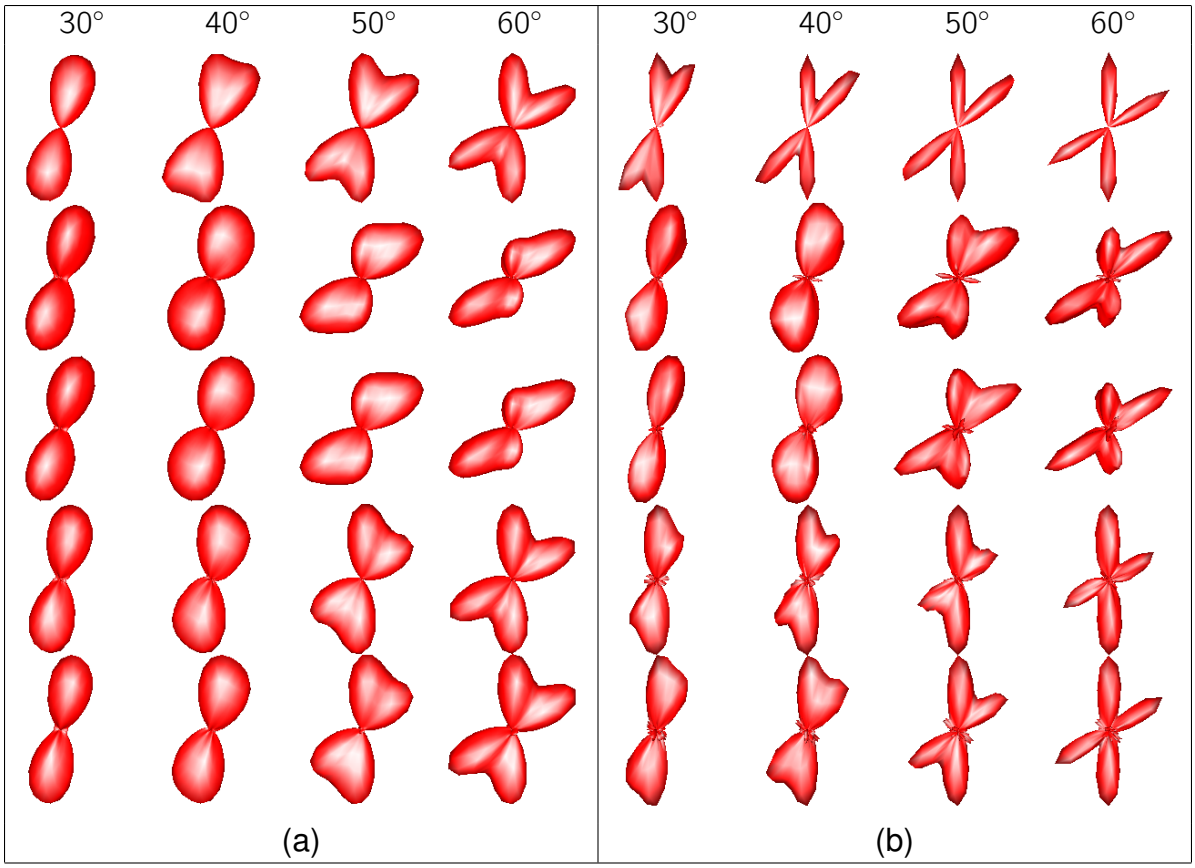

Figure 4-6. Reconstruction of $P(\mathbf{r})$ in the two-fiber case, evaluated at (a) $||\mathbf{r}|| = 15$ and (b) $||\mathbf{r}|| = 25$, using different sampling scheme and embedding lattices. In each figure, we have: first row: true values of $P(\mathbf{r})$, second row: reconstructions using standard scheme and Cartesian lattice, third row: using standard scheme and BCC lattice, forth row: using interlaced scheme and Cartesian lattice, fifth row: using interlaced scheme and BCC lattice.

to the true geometry of $P(\mathbf{r})$. When we compare the reconstructions from Cartesian and BCC embedding lattices, the latter always has less distortion because using a BCC embedding lattice leads to smaller aliasing effects on $P(\mathbf{r})$.

In addition to the visual comparison, some numerical comparison of the reconstruction errors is also necessary. In our multi-shell, model-free scenario, mean square error (MSE) of the reconstructed $\hat{P}(\mathbf{r})$ compared with the true $P(\mathbf{r})$ is a good choice because it indicates both radial and angular reconstruction accuracy. According to Plancherel theorem, it is equivalent to the MSE of the reconstructed $\hat{E}(\mathbf{q})$ in $\mathbf{q}$-space. Thus, we use the MSE of $\hat{E}(\mathbf{q})$ on the embedding lattice points as our error measurement. This

Table 4-1. Sampling directions used in our experiments for Rhombic Triacontahedron and Icosidodecahedron. θ is the elevation and ϕ is the azimuth.

Rhombic Triacontahedron		Icosidodecahedron	
θ	ϕ	θ	ϕ
0°	0°	58.2825°	288°
37.3774°	288°	58.2825°	72°
37.3774°	72°	31.7175°	324°
37.3774°	0°	31.7175°	36°
63.4349°	324°	58.2825°	0°
63.4349°	36°	31.7175°	180°
63.4349°	252°	58.2825°	216°
63.4349°	108°	58.2825°	144°
79.1877°	288°	31.7175°	252°
79.1877°	72°	31.7175°	108°
63.4349°	180°	90°	90°
37.3774°	216°	90°	54°
37.3774°	144°	90°	126°
79.1877°	0°	90°	162°
79.1877°	216°	90°	18°
79.1877°	144°		

error is further divided by the mean value of the true $E^2(\mathbf{q})$ as a normalization so that it is not dependent on the magnitude of the signal. We repeated the reconstruction procedure with Rician noise of different levels, δ_n. The results are shown in Figure 4-7. It is obvious that the interlaced scheme gives less error than the standard scheme and the BCC embedding lattice even further reduces the error. The benefit of BCC lattice over Cartesian lattice is rooted in its ability to capture extra high frequency information without introducing aliasing. But when this information is too noisy, the benefits gradually disappear. As such, the reconstruction errors using Cartesian and BCC lattices approach each other when the noise level increases.

We have shown the visual and numerical comparison of different reconstruction schemes on 2-fiber crossing synthetic data. To explore different fiber configurations, we repeat the comparison on 3-fiber synthetic data. The visual comparisons are shown in Figure 4-9. The numerical comparisons are shown in Figure 4-10. In the end,

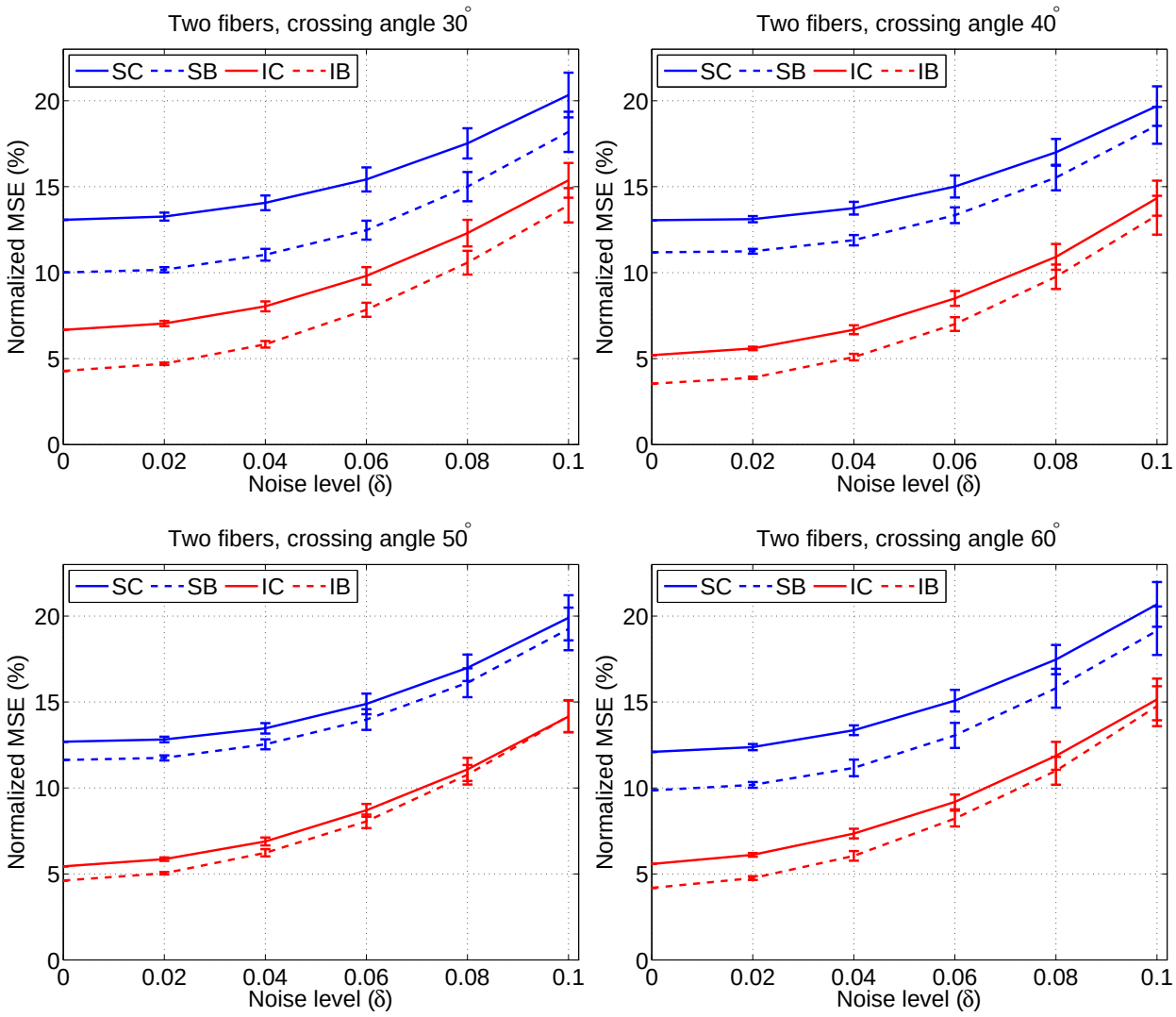

Figure 4-7. Plots showing the normalized MSE of the reconstruction for synthetic data of two-fiber crossings. In the legend, SC means standard scheme with Cartesian lattice. SB means standard scheme with BCC lattice. IC means interlaced scheme with Cartesian lattice. IB means interlaced scheme with BCC lattice.

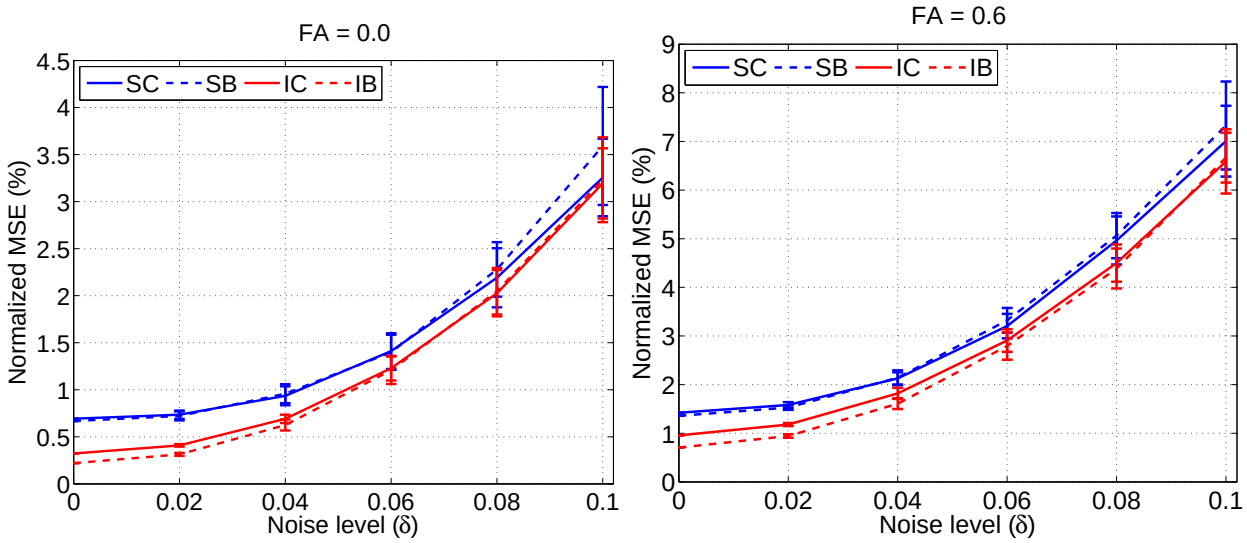

Figure 4-8. Plots showing the normalized MSE of the reconstruction for single fiber synthetic data of FA values 0 and 0.6. FA value equals to 0 means the signal is isotropic.

we provide the numerical error comparisons for 1-fiber synthetic data with different FA values of 0 and 0.6 in Figure 4-8. It is still obvious that our proposed scheme outperforms the standard scheme.

4.3.2 Experiments on real data

To further test our scheme, we acquired real MRI data using both the standard and interlaced multi-shell sampling schemes and compared the reconstruction results. All magnetic resonance imaging was performed on a $600MHz$ (14.1 Tesla) Bruker imaging spectrometer, using a conventional diffusion weighted spin echo pulse sequence. The sampling directions are the same as those used in the synthetic experiments. Three multi-shell datasets, which captured different regions of the mouse brain were acquired: 1) a coronal set at the level of the corpus callosum, 2) a coronal set through the brain stem at the level of the superior colliculus, and 3) a sagittal set through the midline. All the datasets were pre-processed with non-local means filtering to reduce the noise [32, 39].

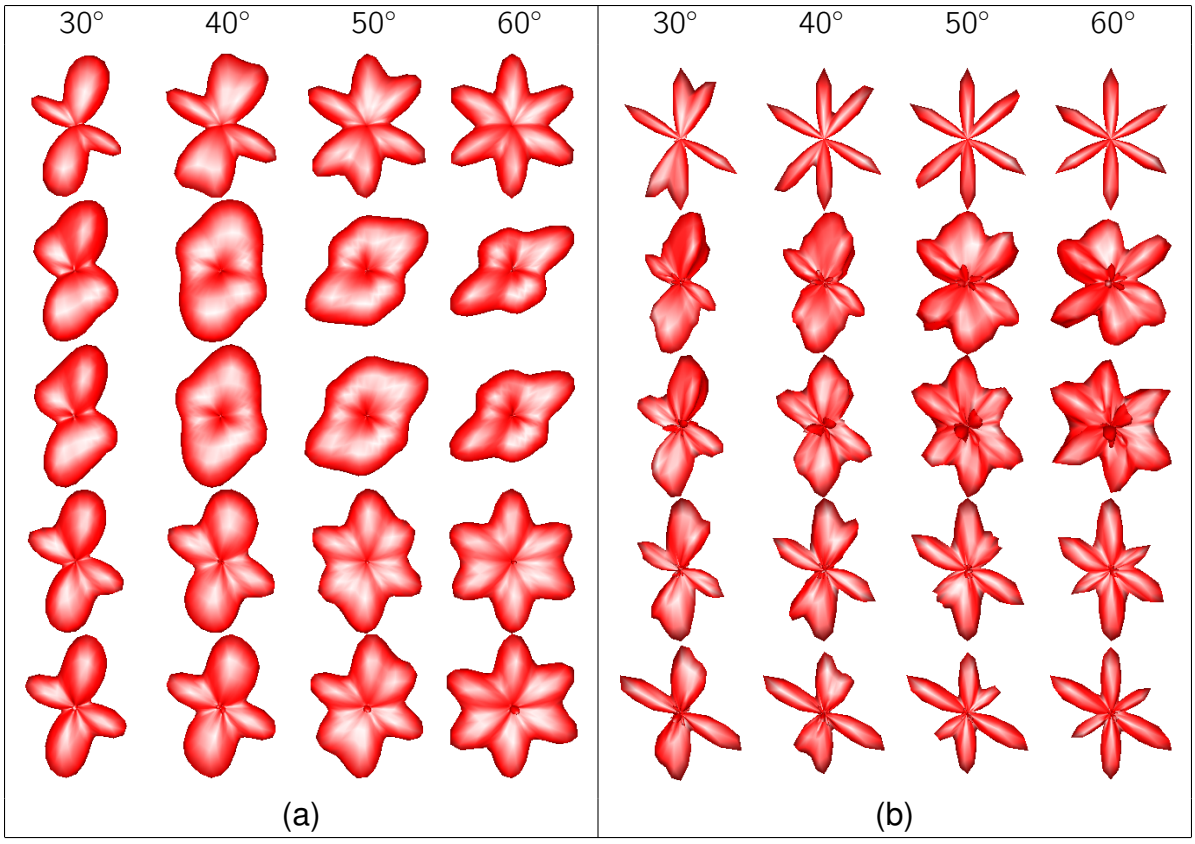

Figure 4-9. Reconstruction of $P(\mathbf{r})$ in the three-fiber case, evaluated at (a) $||\mathbf{r}|| = 10$ and (b) $||\mathbf{r}|| = 15$. Two fixed fibers are of $120°$ crossing and the third fiber is rotating to form different angle to the vertical fiber. The arrangement of the figure is the same as Figure 4-6.

- Dataset $\#1$ was acquired with: slice thickness = $0.7mm$, $1.2 \times 1.2cm^2$ field-of-view, 128×128 data matrix, and $94\mu m$ in-plane resolution. Diffusion parameters included: diffusion time, Δ = $15msec$, diffusion gradient duration, δ = $1msec$, and b-values of 500, 1000, 2000, 3000, 4000 and 5000 s/mm^2 ($\|\mathbf{q}\|$ = 29.1, 41.1, 58.1, 71.2, 82.2, and 91.9 mm^{-1}).

- Dataset $\#2$ was acquired with: slice thickness = $0.3mm$, $1.2 \times 1.2cm^2$ field-of-view, 192×192 data matrix, $62.5\mu m$ in-plane resolution, Δ = $12msec$, δ = $1msec$, and b-values of 187, 750, 1687, and 3000 s/mm^2. The nonuniform spacing between b-values was chosen to provide roughly equal spacing between $\mathbf{q}$-values ($\|\mathbf{q}\|$ = 20.2, 40.3, 60.5, and 80.7 mm^{-1}).

- Dataset $\#3$ was acquired with: slice thickness = $0.35mm$, $1.8 \times 0.9cm^2$ field-of-view, 256×128 data matrix, and $70.3\mu m$ in-plane resolution. Diffusion parameters were identical to those used for dataset $\#2$.

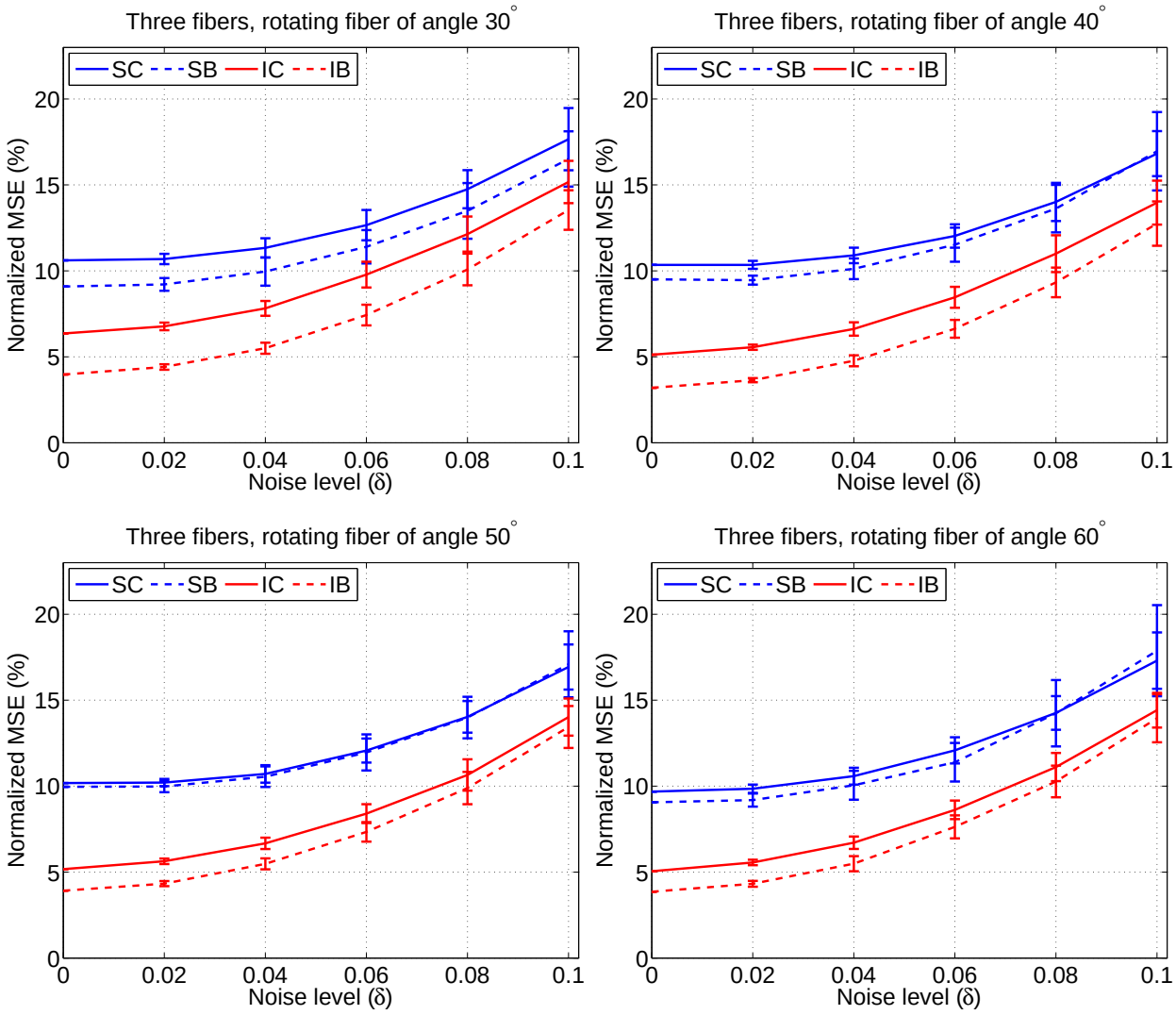

Figure 4-10. Plots showing the normalized MSE of the reconstruction for synthetic data of three-fiber crossings.

The choice of maximum b (or $\|\mathbf{q}\|$) is a compromise between signal-to-noise ratio (SNR) and resolution of the diffusion propagator, $P(\mathbf{r})$. In the experimental data, the SNR of the highest b-value image was 15, 16 and 25 for datasets 1, 2, and 3, respectively. SNR was computed from magnitude images, by dividing the mean of the signal over the entire object by the standard deviation of the noise in an artifact-free background region. The values provided represent the minimum across all of the sampled diffusion directions.

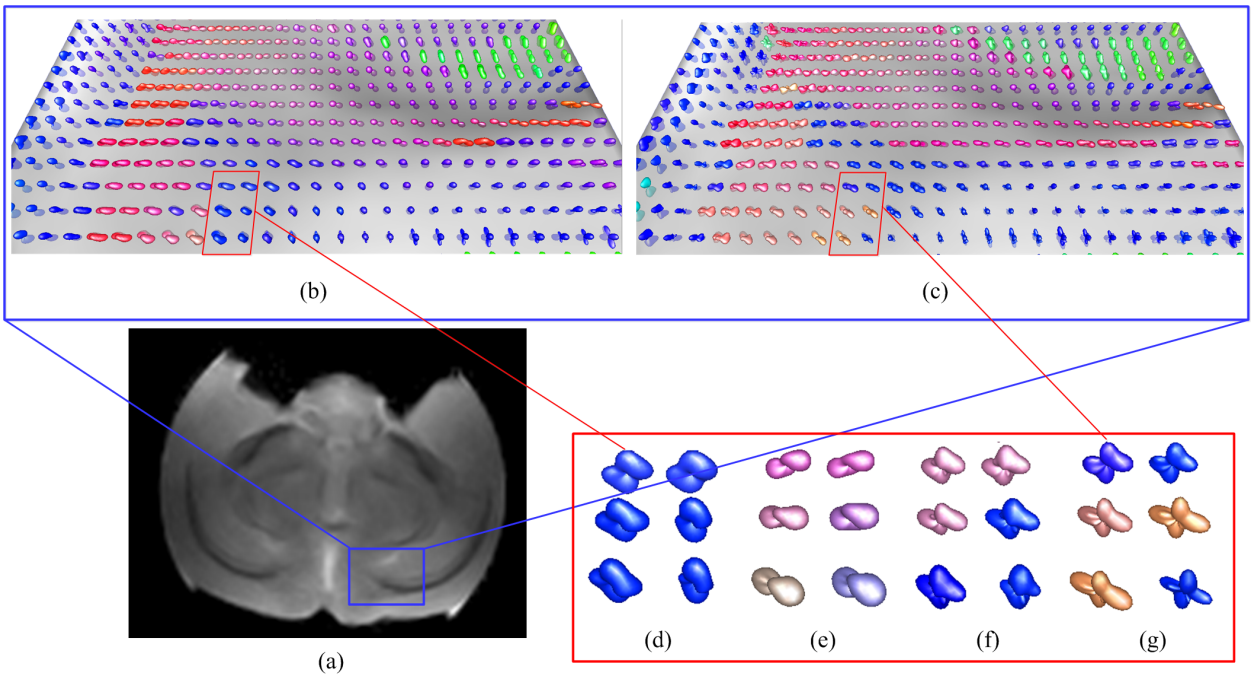

Figure 4-11. Reconstruction results on dataset $\#1$ evaluated at $\|\mathbf{r}\| = 8.0\mu m$. (a) S_0 image of the slice under test where the region of interest (ROI) is shown in the blue box. (b) Reconstruction using standard scheme and Cartesian lattice. (c) Reconstruction using the proposed scheme and BCC lattice. Zoom-in views of reconstructions on several voxels using standard scheme with Cartesian lattice (SC) (d), standard scheme with BCC lattice (SB) (e), interlaced scheme with Cartesian lattice (IC) (f), interlaced scheme with BCC lattice (IB) (g).

Further increases in $\|\mathbf{q}\|$ or b were avoided to limit the Rician noise bias within the data [38]. This comes at the expense of $P(\mathbf{r})$ resolution, which is equal to the inverse of the maximal $\mathbf{q}$-value [28]. While additional resolution is desirable, acquiring noisy data at high $\mathbf{q}$- (or b-) values may not represent an efficient use of the available imaging time. Instead, more time was spent on higher SNR acquisitions at intermediate b-values. This allows for finer sampling of the diffusion signal, $E(\mathbf{q})$, which reduces aliasing distortion in $P(\mathbf{r})$. The total imaging time for the experimental data acquired with the standard sampling scheme was approximately 34, 35 and 28 hours for datasets 1, 2, and 3 respectively. The interlaced scheme resulted in roughly a 1 hour decrease in total scan time.

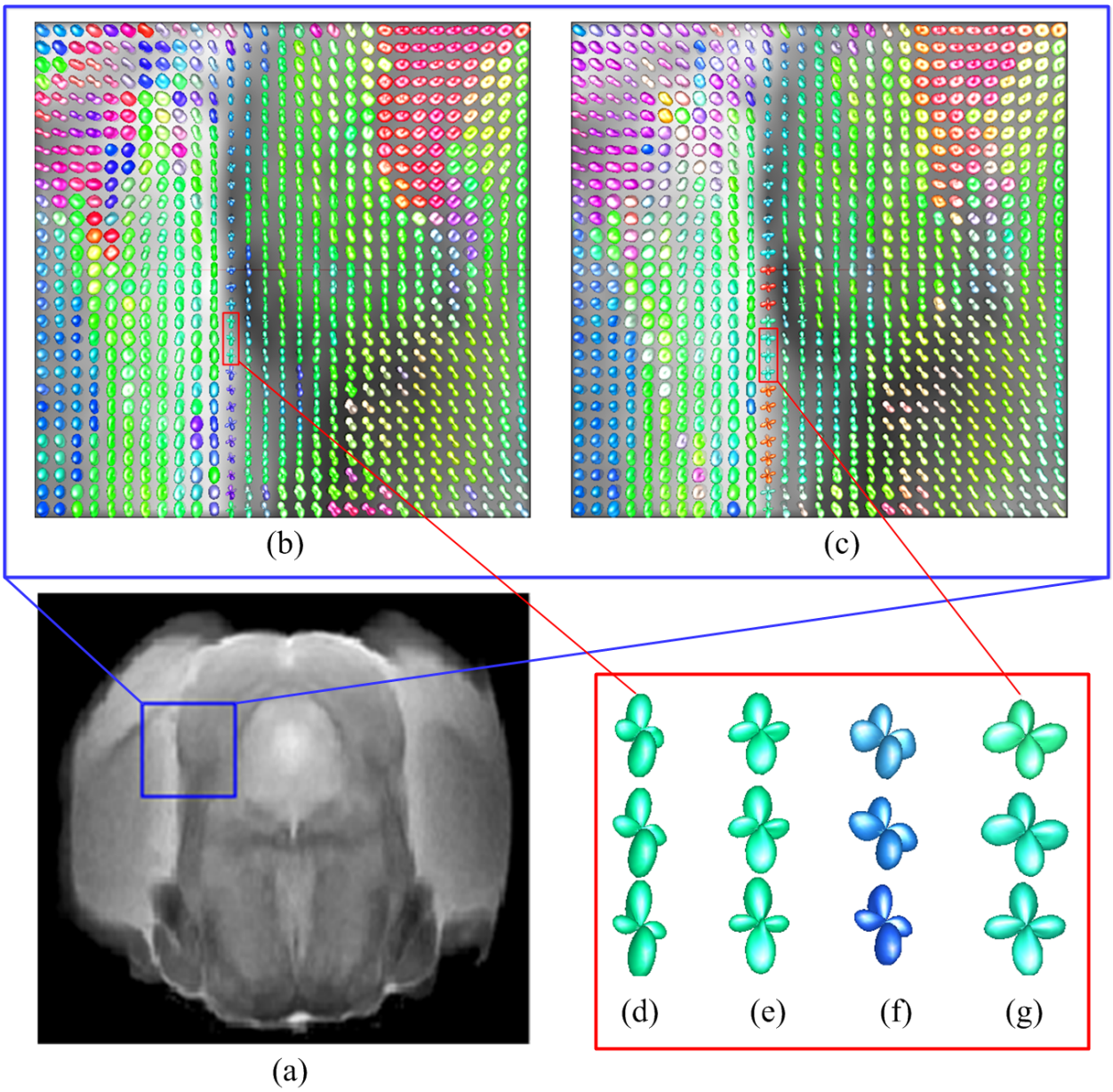

Figure 4-12. Reconstruction results on dataset $\#2$ evaluated at $\|\mathbf{r}\| = 9.8\mu m$. (a) S_0 image of the slice under test where the ROI is shown in the blue box. (b) Reconstructed diffusion propagator using SC scheme. (c) Reconstruction using the IB scheme. Zoom-in views of reconstructions on several voxels using SC scheme (d), SB scheme (e), IC scheme (f), IB scheme (g).

Figure 4-11 shows the reconstruction results of dataset $\#1$. The boxed region of interest contains intersecting fiber bundles from cingulum and corpus callosum. Our proposed scheme provides sharper reconstructions of the fiber crossings in the identified ROI.

Figure 4-12 shows the reconstruction results of dataset #2. We picked this region of interest because it has been validated that there are plenty of in-plane crossing fibers in this region [68]. The results show that our proposed scheme can recover the crossings more accurately.

Figure 4-13 shows the reconstruction results of dataset #3. The branching structure in the highlighted region of interest is obvious. Our proposed scheme provides sharper reconstructions of those fiber crossings.

The comparisons of the reconstructed diffusion propagators using 4 different settings, standard or interlaced scheme with Cartesian or BCC lattice, are shown in Figure 4-11, Figure 4-12 and Figure 4-13 as (d), (e), (f) and (g). The interlaced scheme with BCC lattice is the clear winner for its ability to accurately reconstruct sharp crossings.

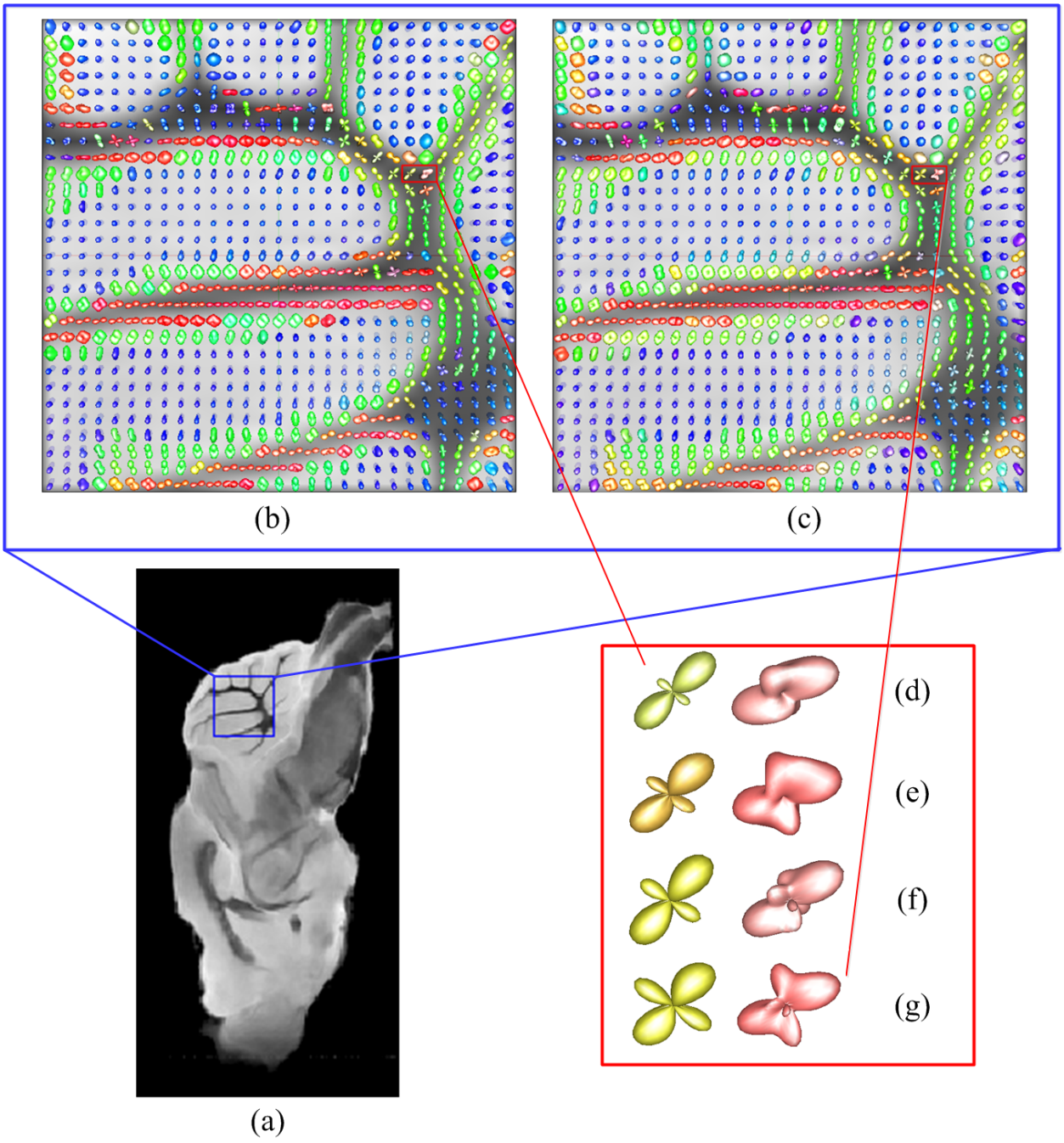

Figure 4-13. Reconstruction results on dataset #3 evaluated at $\|\mathbf{r}\| = 10.0\mu m$. (a) S_0 image of the slice under test where the ROI is shown in the blue box. (b) Reconstruction using SC scheme. (c) Reconstruction using IB scheme. Zoom-in views of reconstructions on several voxels using SC scheme (d), SB scheme (e), IC scheme (f), IB scheme (g).

CHAPTER 5
BOX SPLINE BASED RECONSTRUCTION METHOD

In Chapter 3 and Chapter 4, we discussed the sampling geometries of the diffusion signal and the approaches to re-sampling the diffusion signal on regular lattices, Cartesian and BCC, in the $\mathbf{q}$ space. In this chapter, we develop an independent approach to tomographic reconstruction of diffusion propagators which are represented in box spline basis. The diffusion propagators are directly reconstructed on a pre-defined regular lattice in the displacement space. In this approach, the diffusion propagators are analytically related to the samples of diffusion signals in the $\mathbf{q}$ space through Radon transform and Fourier slice theorem. Thus, there is no need to re-sample diffusion signals on a $\mathbf{q}$ space lattice or to do explicit Fourier transform. However, it can still benefit from the interlaced sampling geometry discussed in Chapter 4.

The key property of box splines that makes them particularly suitable for the tomographic reconstruction is that they are *closed* under X-Ray and Radon transforms [45]. In other words, a signal which is represented in box spline basis can be represented exactly (i.e., with no approximation or discretization of the forward model) in the sinogram space. Therefore, from the X-Ray or Radon data one can formulate the tomographic reconstruction process exactly. The box spline approach offers an exact inversion of X-Ray or Radon transform, similar to Filtered Back Projection algorithm; however, the box spline approach achieves the exact inversion process with finite amount of computation and data, in contrast to the FBP solution. From the approximation-theoretic point of view, the box spline approach can be considered as a generalization of the (square) pixel basis approach that allows for basis functions with higher approximation order (than the pixel basis). The increase in approximation order offered by the compactly supported box splines can lead to significant savings in the computational cost of reconstruction.

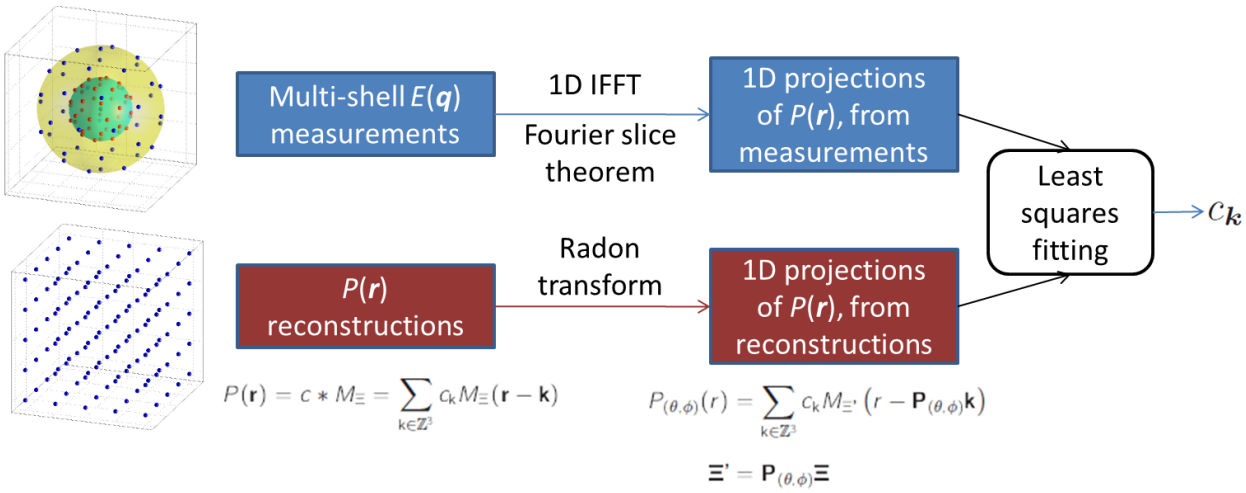

Figure 5-1. Diagram of the reconstruction process. Measurements of $E(\mathbf{q})$ are on $\mathbf{q}$-space shells. $P(\mathbf{r})$ is represented with shifted sum of box splines sitting on a regular lattice, Cartesian in this case. The reconstruction problem turns out to be the least square fitting to the projected data (sinogram data).

We present synthetic and real multi-shell diffusion-weighted MR data experiments that demonstrate the increased accuracy of $P(\mathbf{r})$ reconstruction as the order of basis functions is increased.

5.1 Box Splines and Radon Transform

A box spline is a smooth piecewise polynomial, compactly-supported, function (defined on $\mathbb{R}^2, \mathbb{R}^3$ or generally in $\mathbb{R}^d$), that is associated with a set of vectors that are usually gathered in a matrix: $\mathbf{\Xi} = [\boldsymbol{\xi}_1 \dots \boldsymbol{\xi}_N]$ [34]. From the signal processing point of view, box splines are constructed by repeated convolution of elementary line-segment distributions along each vector in $\mathbf{\Xi}$. Specifically, we have:

$$M_{\Xi}(\mathbf{x}) = \left(M_{\boldsymbol{\xi}_1} * \cdots * M_{\boldsymbol{\xi}_N}\right)(\mathbf{x}), \tag{5–1}$$

where the elementary box splines, $M_{\boldsymbol{\xi}_n}$, are Dirac-like line distributions supported over $\mathbf{x} = t\boldsymbol{\xi}_n$ with $t \in [0, 1]$. These elementary box splines are in direct geometric

correspondence (via a rotation and a proper scaling) with the primary box spline

$$M_{\vec{e}_1}(\mathbf{x}) = \text{box}(x_1)\delta(x_2, \cdots, x_d) \tag{5–2}$$

where $\delta(x_2, \cdots, x_d)$ is the $(d-1)$-dimensional Dirac distribution and

$$\text{box}(x) = \begin{cases} 1 & 0 \leq x \leq 1 \\ 0 & \text{otherwise} \end{cases}.$$

Moreover, they integrate to 1 which is a property that is shared by all box splines (and also preserved through convolution).

Based on (5–1), one directly infers that the box splines are positive, compactly-supported functions. Their support is a zonotope, which is the Minkowski sum of N vectors in $\boldsymbol{\Xi}$.

For instance, in a 3-D setting, a pixel basis (i.e., voxel basis) can be represented by a box spline whose direction matrix, $\boldsymbol{\Xi} = \mathbf{I}_3$ is the 3×3 identity matrix. More generally, an n^{th}-order tensor-product B-spline can be represented as a box spline whose direction matrix contains the directions in $\mathbf{I}_3$, each of which is repeated by n-times.

The key property of box splines that is used in our tomographic approach is that the Radon transform of a box spline along a particular direction specified by (θ, ϕ) is a univariate (1-D) box spline whose direction vectors are the *geometric* projection of the original box spline directions [45]. Let $P_{(\theta,\phi)}$ denote the projection matrix that geometrically projects a point $\mathbb{R}^3$ to the line specified by the direction (θ, ϕ). Then, the Radon transform of a trivariate box spline associated with a matrix $\boldsymbol{\Xi}$ is a 1-D box spline specified by $\boldsymbol{\Xi}' = P_{(\theta,\phi)}\boldsymbol{\Xi}$ (see Figure 5-2).

This property suggests that for tomographic reconstruction applications, box splines are suitable basis functions for representing the source signal. This choice of representation of the source signal, leads to an exact forward-model that can be used to match the sinogram data. This property is exploited in the following section for our reconstruction algorithm.

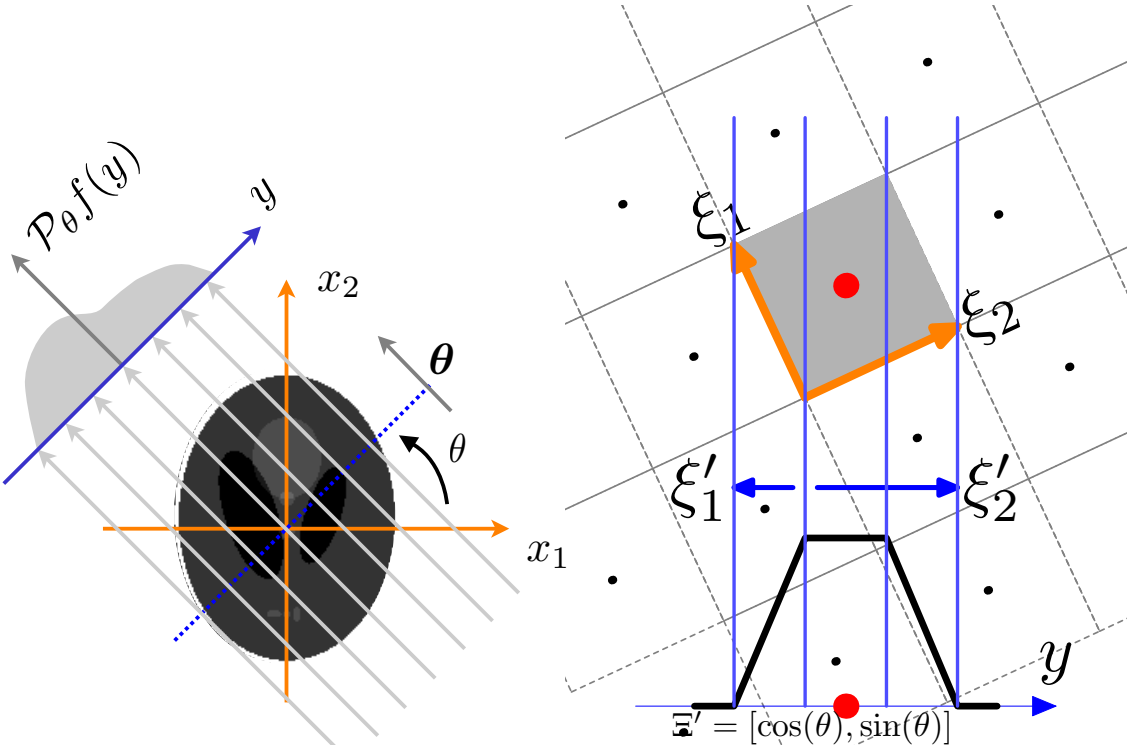

Figure 5-2. A 2-D illustration of Radon transform geometry. On the right: Radon transform of a pixel (tensor-product first-order B-spline) leads to a 1-D box spline whose directions are the *geometric* projection of the directions of the source box spline. This property directly generalizes to 3-D for voxel or higher-order basis.

5.2 Detailed Algorithm

In practice, diffusion propagator $P(\mathbf{r})$ is reconstructed from samples of diffusion signal $E(\mathbf{q})$. The $\mathbf{q}$-space samples usually lie on radial lines through the origin of different orientations. According to the Fourier transform relationship in (1–1) and the Fourier slice theorem, the 1-D inverse Fourier transform of the restriction of $E(\mathbf{q})$ to a radial line equals to the Radon transform of $P(\mathbf{r})$ along line in $\mathbf{r}$ space of the same orientation. Hence, the reconstruction problem is equivalent to inverting the Radon transform that translates into reconstructing the $P(\mathbf{r})$ from its projections, (i.e., Radon data). This problem problem has widely been studied in the tomographic reconstruction literature. Our contribution is that we generalize the natural pixel basis, which is the first order tensor product B-spline, to basis functions of high approximation power using the

framework of non-separable box splines. The more general class of box splines include higher-order tensor-product B-splines as a special case, but also include non-separable basis functions. This generalization significantly simplifies the inversion of Radon transform since the more general class of box splines happen to be closed under X-Ray and Radon transform.

We assume that $P(\mathbf{r})$ can be represented in box spline basis:

$$P(\mathbf{r}) = c * M_{\Xi} = \sum_{\mathbf{k}\in\mathbb{Z}^3} c_{\mathbf{k}} M_{\Xi}(\mathbf{r}-\mathbf{k}). \tag{5–3}$$

When $\mathbf{\Xi}$ is the 3×3 identity matrix, the box spline corresponds to the cube voxel basis and we have a piecewise-constant approximation of $P(\mathbf{r})$. However, a higher order tensor-product B-spline or generally a non-separable box spline can be used in the above approximation to achieve a higher-order approximation to the true $P(\mathbf{r})$. The reconstruction problem is now the task of finding suitable coefficients $c_{\mathbf{k}}$ in (5–3) such that $P(\mathbf{r})$ agrees with the given data (i.e., samples of diffusion signal $E(\mathbf{q})$). According to the discussion in 5.1, the Radon transform of $P(\mathbf{r})$ for a given direction (θ, ϕ) is:

$$\begin{aligned} P_{(\theta,\phi)}(r) &= \sum_{\mathbf{k}\in\mathbb{Z}^3} c_{\mathbf{k}} M_{\Xi'}\left(r - \mathbf{P}_{(\theta,\phi)}\mathbf{k}\right) \\ \mathbf{\Xi'} &= \mathbf{P}_{(\theta,\phi)}\mathbf{\Xi} \end{aligned} \tag{5–4}$$

where $\mathbf{P}_{(\theta,\phi)}$ is the 3-D to 1-D projection matrix onto the direction (θ, ϕ). Note that the Cartesian grid shifts $\mathbf{k} \in \mathbb{Z}^3$, are also transformed by $\mathbf{P}_{(\theta,\phi)}$. In other words, the Radon-transform data can be represented by $\mathbf{P}_{(\theta,\phi)}\mathbf{k}$ shifts of the 1-D box spline which is associated with the matrix $\mathbf{\Xi'} = \mathbf{P}_{(\theta,\phi)}\mathbf{\Xi}$.

Denoting the samples of real projected data as $d_{(\theta,\phi)}(r)$ and enforce $d_{(\theta,\phi)}(r) = P_{(\theta,\phi)}(r)$ at all the sample points, we can build a linear equation set expressed as $\mathbf{Ac} = \mathbf{d}$ where $\mathbf{c}$ is the vector composed of coefficients $c_{\mathbf{k}}$ in (5–4), $\mathbf{d}$ is the vector of sampled data and each row of $\mathbf{A}$ is the evaluations of $M_{\mathbf{P}_{(\theta,\phi)}\Xi}(r)$ at each sample position. In our application, the number of samples is usually smaller than the number of shifted box

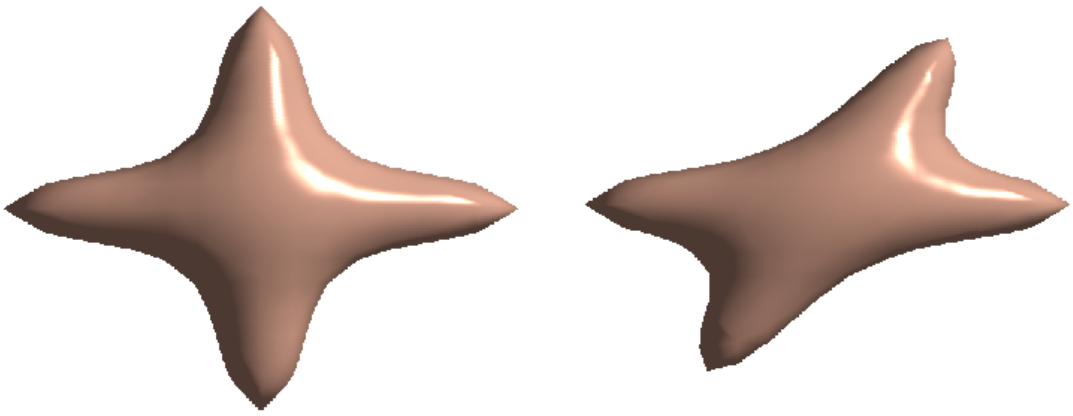

(a) (b)

Figure 5-3. The desired isosurface of $P(\mathbf{r})$: (a) of 90° crossing (b) of 60° crossing

splines, so the linear system is under-determined. In order to get reasonable solution of coefficients, we introduce a smoothness regularization and search for the least square solution. Hence, we solve the following optimization problem:

$$\min_{\mathbf{c}} ||\mathbf{Ac} - \mathbf{d}||^2 + \lambda||\mathbf{Lc}||^2 \tag{5–5}$$

where $\mathbf{L}$ is the matrix of 3-D discrete Laplacian operator on $\mathbf{c}$, λ is the weights for the smoothness regularization term $||\mathbf{Lc}||^2$.

5.3 Experimental Results of the Algorithm

We first evaluated our algorithm using synthetic data. We generated samples from a mixture of two Gaussian functions in 3-D $\mathbf{q}$-space simulating the diffusion signal of two-fiber crossings. Crossing angles of 90° and 60° as shown in Figure 5-3 were tested. The data samples are uniformly distributed on radial lines specified by spherical coordinates (r, θ, ϕ) with $0 \leq r \leq 35$. We picked 19 points on each radial line and 81 directions that correspond to vertices of a subdivided icosahedron approximating a unit hemisphere. The basis function of choice were tensor-product B-splines shifted on a $25 \times 25 \times 25$ Cartesian lattice.

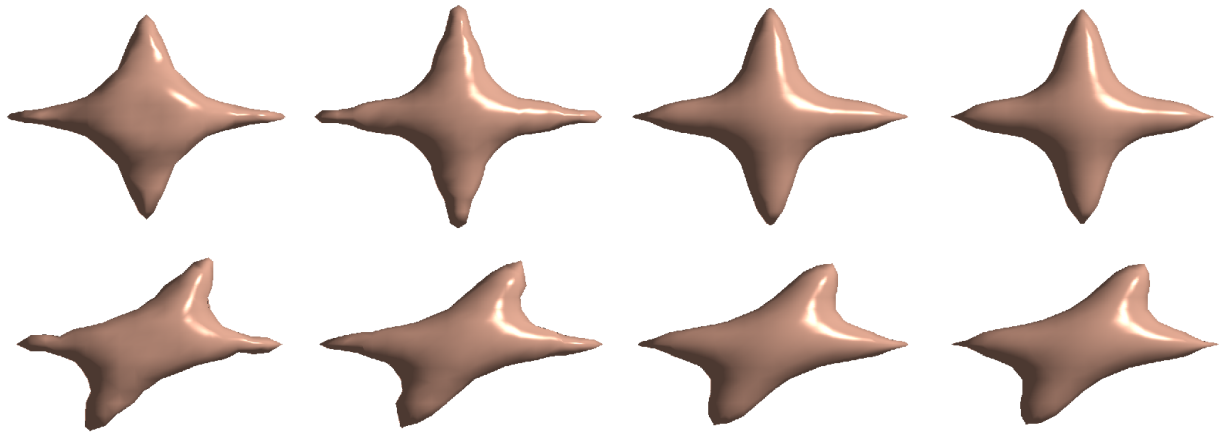

(a) (b) (c) (d)

Figure 5-4. Reconstruction results for the synthetic data. First row, 90° crossing. Second row, 60° crossing. (a) first order box spline, (b) second order box spline, (c) third order box spline, (d) fourth order box spline.

Table 5-1. MSE in percentage of the reconstructions for the synthetic data. α is the crossing angle. δ_n is the noise level. n is the order of the box spline.

α	δ_n	$n=1$	$n=2$	$n=3$	$n=4$
3*90°	0	16.03	7.02	3.34	2.80
	.04	$19.16 \pm .79$	$10.17 \pm .25$	$5.25 \pm .15$	$4.53 \pm .14$
	.08	27.87 ± 1.31	$19.88 \pm .62$	$11.34 \pm .46$	$10.38 \pm .31$
3*60°	0	11.67	7.42	3.57	2.95
	.04	$15.05 \pm .54$	$10.45 \pm .26$	$5.37 \pm .16$	$4.66 \pm .14$
	.08	$22.97 \pm .85$	$19.99 \pm .80$	$11.38 \pm .33$	$10.56 \pm .39$

Figure 5-4 show the isosurfaces of the reconstructed $P(\mathbf{r})$ with different B-spline basis orders. We observe that the reconstruction becomes smoother and more accurate as the order of the basis function increases. Increasing the approximation order above the third order leads to less significant improvement as the approximation error becomes very small for this particular dataset. Numerical comparisons with different noise level δ_n are shown in Table 5-1. The mean square error (MSE) normalized by the energy of the desired signal was used as the measurement. The numerical results also support the expected advantages of higher order basis functions.

We also tested our algorithm on real multi-shell data consisting of mid-sagittal mouse brain scans acquired at different b values. 16 orientations and 5 different b

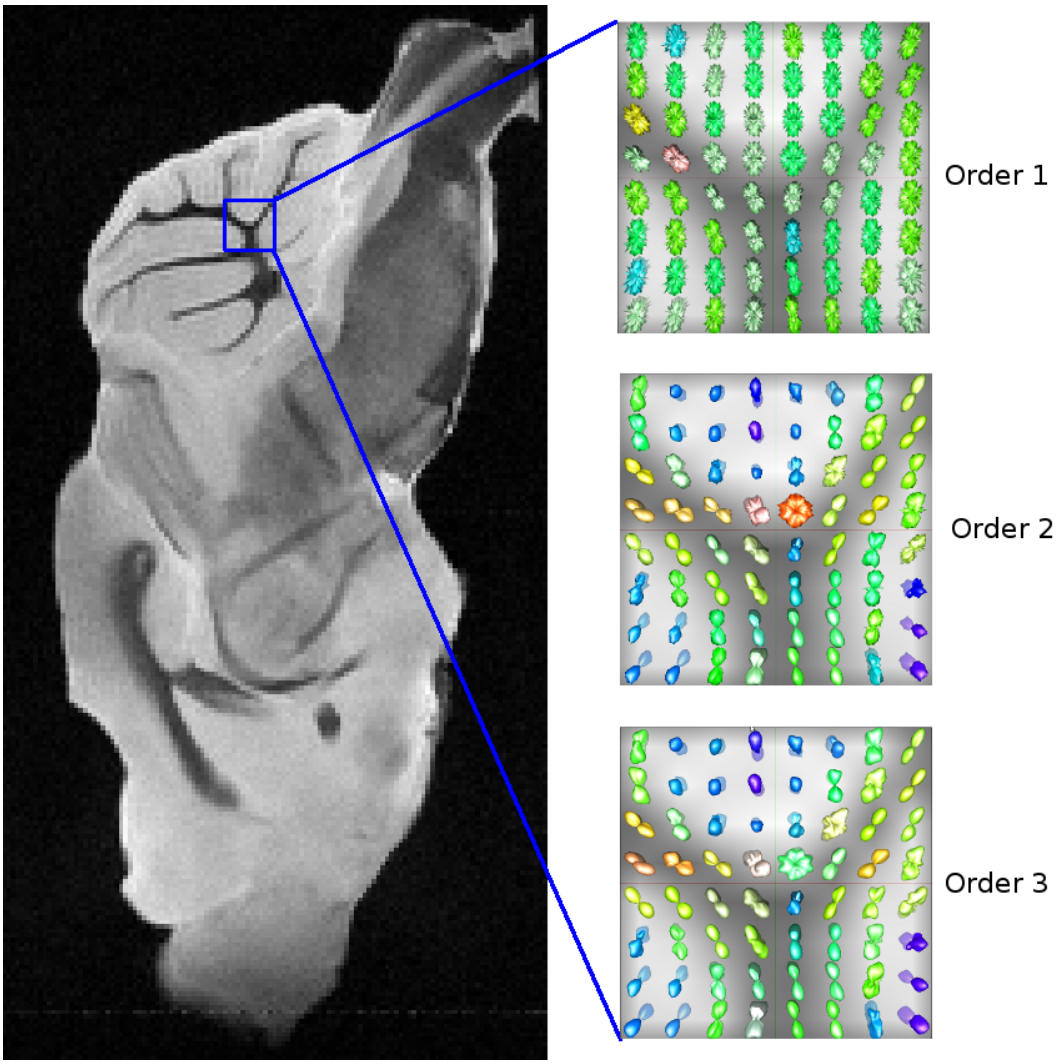

Figure 5-5. Reconstruction results for a region of the multi-shell mouse brain data with different box spline basis orders.

values, including $b = 0$, were used. All magnetic resonance imaging was performed on a $600MHz$ (14.1 Tesla) Bruker imaging spectrometer, using a conventional diffusion weighted spin echo pulse sequence. The dataset was acquired with: slice thickness = $0.35mm$, $1.8 \times 0.9cm^2$ field-of-view, 256×128 data matrix, and $70.3mm$ in-plane resolution, Δ = $12msec$, δ = $1msec$, and b-values of 187, 750, 1687, and 3000 s/mm^2. The nonuniform spacing between b-values was chosen to provide roughly equal spacing between $\mathbf{q}$-values ($\|\mathbf{q}\|$ = 20.2, 40.3, 60.5, and 80.7 mm^{-1}).

Figure 5-5 shows the reconstructed $P(\mathbf{r})$ for a small region of the real data set with different box spline orders. We can observe the smoothness improvement going from the first order one to the third order. For the first order box spline basis (i.e., voxel basis), the reconstructed $P(\mathbf{r})$ is discontinuous; hence, the $P(\mathbf{r})$ values (evaluated on the sphere for visualization) appear spiky as shown in Figure 5-5 Order 1.

CHAPTER 6
RECONSTRUCTION OF A DIFFUSION PROPAGATOR FIELD

All the discussion before was focused on the reconstruction of a single diffusion propagator at one voxel. In reality, the diffusion MRI signal is almost always collected as a volumetric data containing lots of voxels in the 3D space. So the desired reconstruction result is a diffusion propagator field. By assuming independence among different voxels, we can reconstruct the whole field through applying the aforementioned methods onto all the voxels one by one. However, the reconstruction can be much more resilient to noise by considering the coherence among the diffusion profiles of the adjacent voxels.

In this chapter, We present a dictionary learning framework for achieving a smooth diffusion propagator reconstruction across the field wherein, the dictionary atoms are learned from the data via an initial regression using adaptive spline kernels. The formulation involves optimizing for a sparse dictionary using a K-SVD based updating and a non-local means based regularization across the field. The novelty lies in a dictionary based reconstruction as well as an NLM-based regularization that helps preserving features in the reconstructed field. We document experimental results on synthetic data from crossing fibers and real optic chiasm data set that demonstrate the advantages of the proposed approach.

6.1 Overview: From Fixed Basis to Data Driven Dictionary

The DW-MRI datasets are usually provided as a field of $S(\mathbf{q}, \mathbf{x})$ where $\mathbf{x}$ specifies spatial locations. Most of the existing reconstruction methods reconstruct $P(\mathbf{r}, \mathbf{x})$ at each location $\mathbf{x}$ independently which do not consider the spatial coherency that inherently exists in the data. In a recent study [80], a spatially regularized reconstruction approach was developed that exploits sparse representation of $P(\mathbf{r})$ in spherical ridgelet basis. In this framework, spherical ridgelet transform was applied at every voxel on $S(\mathbf{q}, \mathbf{x})$ to obtain a sparse representation. Then the sparsity of transform-domain coefficients as well as the total variation of the reconstructed signal field $S(\mathbf{q}, \mathbf{x})$, with respect to $\mathbf{x}$ were

used to formulate the reconstruction as the following optimization problem:

$$\min_{\mathbf{C}} \frac{1}{2}||\mathbf{AC}-\mathbf{S}||_F^2 + \lambda \sum_i ||\mathbf{c}_i||_1 + \mu TV\{\mathbf{AC}\}. \quad (6\text{–}1)$$

In this formulation, $\mathbf{A}$ is the spherical ridgelet transform matrix, $\mathbf{C}$ contains the transform coefficients at all voxels in the field of interest where each column, $\mathbf{c}_i$, is one set of transform coefficients at i^{th} voxel. $\mathbf{AC}$ represents the reconstructed diffusion signal field and $TV\{\mathbf{AC}\}$ is the total variation of the reconstructed field. The third term enforces correlations among $\mathbf{c}_i$ from neighbouring voxels which makes the solution of the coefficient field spatially regularized. The final step is to calculate the diffusion propagator from the reconstructions as $\mathbf{P} = \{\mathbf{A}\}\mathbf{C}$ where $\{\mathbf{A}\}$ denotes the Fourier transform of the basis functions (i.e., spherical ridgelets).

$\mathbf{A}$ in the above formulation is fixed to be the spherical ridgelet bases truncated up to a certain degree. In contrast we introduce a dictionary-based method where we learn the basis functions in $\mathbf{A}$ from data examples that will provide a sparse representation. Through updating both $\mathbf{A}$ and $\mathbf{C}$ during the optimization process, we obtain a dictionary learned from the specific dataset as well as the corresponding sparse representation of the reconstruction. The globally defined dictionary plays an implicit role of regularizing the reconstructions over different voxels. We also introduce the spherical deconvolution model with adaptive kernels to control the way the dictionary gets updated. In addition, we use an NLM-based regularization which further suppresses the noise. We will briefly introduce the adaptive kernels in Section 6.2 and give the dictionary learning framework in Section 6.3. Section 6.4 will show the experiment results.

6.2 Adaptive Kernels for Multi-fiber Reconstruction

Given a diffusion-weighted MR dataset, there are many methods employing different spherical deconvolution kernels to reconstruct the multi-fiber diffusion profile. In the spherical deconvolution framework, the DW-MRI signal is considered as the convolution

of a kernel function k with a probability density function f over the sphere [56]:

$$E(b, \mathbf{g}) = \int f(\mathbf{p}) k(b, \mathbf{g}|\mathbf{p}) \, \mathrm{d}\mathbf{p} \tag{6–2}$$

where b is the diffusion weighting, $||\mathbf{g}|| = 1$ and $\mathbf{q} \sim \sqrt{b}\mathbf{g}$. The integration is over the domain of parameter $\mathbf{p}$. Many well known reconstruction techniques turn out to be the special cases of (6–2) by picking certain kernel functions $k(b, \mathbf{g}|\mathbf{p})$ and mixing densities $f(\mathbf{p})$ [56]. For example, k can be multivariate Gaussian function $k(b, \mathbf{g}|\mathbf{D}) = \exp(-b\mathbf{g}^T\mathbf{D}\mathbf{g})$[104]. The choices of such fix-shaped kernels are used to represent the diffusion property of the underlying fibers; however they also impose some unnecessary assumptions which may not hold for the real DW-MRI dataset.

Adaptive spline kernels [11] were proposed as a flexible kernel model to fit datasets with varieties of different diffusion patterns. The density function f is re-parametrized on the sphere as $f(\mathbf{p}) = \sum_{j=1}^{N} w_j \phi(\mathbf{p}|\mathbf{v}_j)$ where $\mathbf{v}_1, ..., \mathbf{v}_N$ is a set of unit vectors uniformly distributed on the hemisphere. By letting the reconstruction kernel $K(b, \mathbf{g}|\mathbf{v}_j) = \int \phi(\mathbf{p}|\mathbf{v}_j) k(b, \mathbf{g}|\mathbf{p}) \mathrm{d}\mathbf{p}$ and considering the case of a constant b-value (which is quite common in HARDI acquisition), we have:

$$E(\mathbf{g}) = \sum_{j=1}^{N} w_j K(\mathbf{g}|\mathbf{v}_j) = \sum_{j=1}^{N} w_j \sum_{k=1}^{P} c_k \psi_k(|\mathbf{g} \cdot \mathbf{v}_j|), \tag{6–3}$$

where K is represented in spline bases ψ_k. The shape of the kernel is flexible and is determined by the control points c_k. When we plug a number of measurements $S(\mathbf{g}_i), i = 1, ..., M$ and the corresponding gradient directions $\mathbf{g}_i$ into (6–3), we obtain M linear equations with respect to unknowns w_j and c_k. w_j and c_k are then estimated through non-negative least square fitting in an alternative pattern. In other words, w_j is estimated while c_k are fixed and then c_k's are estimated while w_j are fixed. See [11] for details of the search algorithm.

Finally, the diffusion propagator is calculated by the estimated w_j and c_k parameters and by applying the Fourier transform on both sides of (6–3). Since ψ_k are known spline bases, their Fourier transforms can be calculated beforehand.

6.3 Dictionary based Reconstruction Framework

In the afore-mentioned spherical deconvolution framework, diffusion signal is modelled as weighted sum of kernel functions each of which represents the diffusion properties of a single fiber. The number of parameters, c_k, in kernel functions and the weights, w_j, is usually very large which makes the reconstruction problem ill-posed. Fortunately, the fact that the number of fibers at each voxel is limited in real datasets allows us to exploit the sparsity of weighting coefficients to solve the reconstruction problem. The problem of searching for the proper kernel function as well as the sparse weighting coefficients can be solved by a dictionary learning paradigm.

For a given voxel v, we define the weights as a vector $\mathbf{w}_v$ whose j^{th} element is denoted by w_j, the measurements as vector $\mathbf{e}_v$ whose i^{th} element is denoted by $E(\mathbf{g}_i)$, and $\mathbf{K}_v$ which denotes the kernel $\mathbf{K}_v(i,j) = K(\mathbf{g}_i|\mathbf{v}_j)$. With these notations (6–3) becomes $\mathbf{e}_v = \mathbf{K}_v\mathbf{w}_v$ where $\mathbf{K}$ is flexible by changing coefficients c_k. Modelling signal within a single voxel can be interpreted as a dictionary learning problem with one observation and dictionary atoms formed by our splines.

Instead of fitting the adaptive kernel to the signal at each voxel individually, here we use an over complete dictionary $\mathbf{K}_{M\times D}, D > N$ for all the voxels. We define $\mathbf{E} = [\mathbf{e}_1, ..., \mathbf{e}_V]$ as the measurements from all the voxels in the field of interest, $\mathbf{W} = [\mathbf{w}_1, ..., \mathbf{w}_v]$ as the corresponding weights respect to the new global dictionary $\mathbf{K}$. Now, we can formulate the modelling of the whole field as the optimization problem:

$$\min_{\mathrm{K,W}} ||\mathbf{E} - \mathbf{KW}||_F^2 \quad \text{s.t. } \forall v, ||\mathbf{w}_v||_0 \leq T_0 \tag{6–4}$$

where T_0 specifies how many non-zero weights are allowed. There are many algorithms which solve this dictionary learning problem, we pick the K-SVD algorithm [3] because

of its simplicity and efficiency. The global dictionary $\mathbf{K}$ implicitly brings in some spatial regularization such that the reconstructed field $\mathbf{KW}$ does not change independently at each voxel. The dictionary size D and sparsity constraint T_0 indirectly control the smoothness of the reconstructions.

In order to further suppress the noise during the reconstruction, we introduce an explicit regularization term:

$$\min_{\mathrm{K,W}} ||\mathbf{E} - \mathbf{KW}||_F^2 + \mu M\{\mathbf{KW}\} \quad \text{s.t. } \forall v, ||\mathbf{w}_v||_0 \leq T_0 \tag{6–5}$$

where $M\{\mathbf{KW}\}$ is a roughness measure of the reconstruction $\mathbf{KW}$. In (6–1), M is set to be the total variation. In this chapter, we propose to use the deviation of $\mathbf{KW}$ from its non-local means $NL\{\mathbf{KW}\}$ [18], i.e. $M\{\mathbf{KW}\} = ||\mathbf{KW} - NL\{\mathbf{KW}\}||_F^2$.

A direct solution to this problem is difficult because of the complicated regularization term. So we solve it iteratively through assuming that the component $NL\{\mathbf{KW}\}$ has fixed value estimated from last iteration. Then, at each iteration t, we are solving the following optimization problem:

$$\{\mathbf{K}^t, \mathbf{W}^t\} = \operatorname*{argmin}_{\mathrm{K,W}} ||\mathbf{E} - \mathbf{KW}||_F^2 + \mu ||\mathbf{KW} - NL\{\mathbf{K}^{t-1}\mathbf{W}^{t-1}\}||_F^2 \text{ s.t. } \forall v, ||\mathbf{w}_v||_0 \leq T_0 \tag{6–6}$$

which is equivalent to:

$$\{\mathbf{K}^t, \mathbf{W}^t\} = \operatorname*{argmin}_{\mathrm{K,W}} ||\mathbf{E}_{t-1} - \mathbf{KW}||_F^2 \text{ s.t. } \forall v, ||\mathbf{w}_v||_0 \leq T_0 \tag{6–7}$$

where $\mathbf{E}_{t-1} = \frac{1}{1+\mu}(E + \mu NL\{\mathbf{K}^{t-1}\mathbf{W}^{t-1}\})$ and $\mathbf{E}_0 = E$. Then, the problem can be solved through iteratively applying K-SVD algorithm.

To initialize the dictionary $\mathbf{K}$, we individually fit the adaptive spline kernel to every voxel in the field and pick D of the kernels with the largest weights across the field. And at each iteration t, we refit the adaptive kernel to $\mathbf{K}^t$ to ensure that the atoms of our dictionary can still be expressed in (6–3).

6.4 Results

In this section, we evaluate our proposed reconstruction framework by comparing to the reconstruction of $P(\mathbf{r})$ on individual voxels, and our regularized framework. The experiments demonstrate the advantages of the regularization from the learned global dictionary as well as the non-local smoothness regularizer.

6.4.1 Synthetic Dataset

We first evaluate the reconstruction performance with our synthetic data field using the simulation model proposed in [98] with cylindrical fiber radius of $5\mu m$, length $5mm$ and diffusion weighting $b = 1500s/mm^2$. All the data were simulated using 81 gradient directions with different noise level δ changing from 0 to 0.3. We compared our results against the voxel-wise individual reconstruction, voxel-wise reconstruction on the smoothed data field using the non-local mean denoising algorithm and the reconstruction using dictionary learning without smoothness regularization. For the individual adaptive kernel, we picked $N = 321$, $P = 5$, ψ_k to be a 3rd-order B-spline basis function. For our dictionary learning framework, we set dictionary size $D = 100$, $T_0 = 4$, $\lambda = 2\delta$ and $\mu = 10\delta$ where δ can be estimated in real dataset. For NLM, we set the radius of local patch to be 3, the radius of neighbourhood search window to be 5. In our experiments, we observed the advantages of our method is not sensitive to choices of λ and μ. The reconstructed diffusion propagator fields ($\delta = 0.2$) are shown in Figure 6-1. We also show the error comparison among these methods under different noise level in Figure 6-2 (a) and the convergence plot in Figure 6-2 (b).

The results show that the proposed method is much more accurate when the noise level is high since the voxel-wise reconstruction method does not take advantage of the smooth global fiber structure and is more vulnerable to the noise. We also see that the dictionary learning method itself without smoothness regularization can provide some degrees of resilience to the noise. This is because the dictionary learned is supposed to represent the consistent components over the whole data volume.

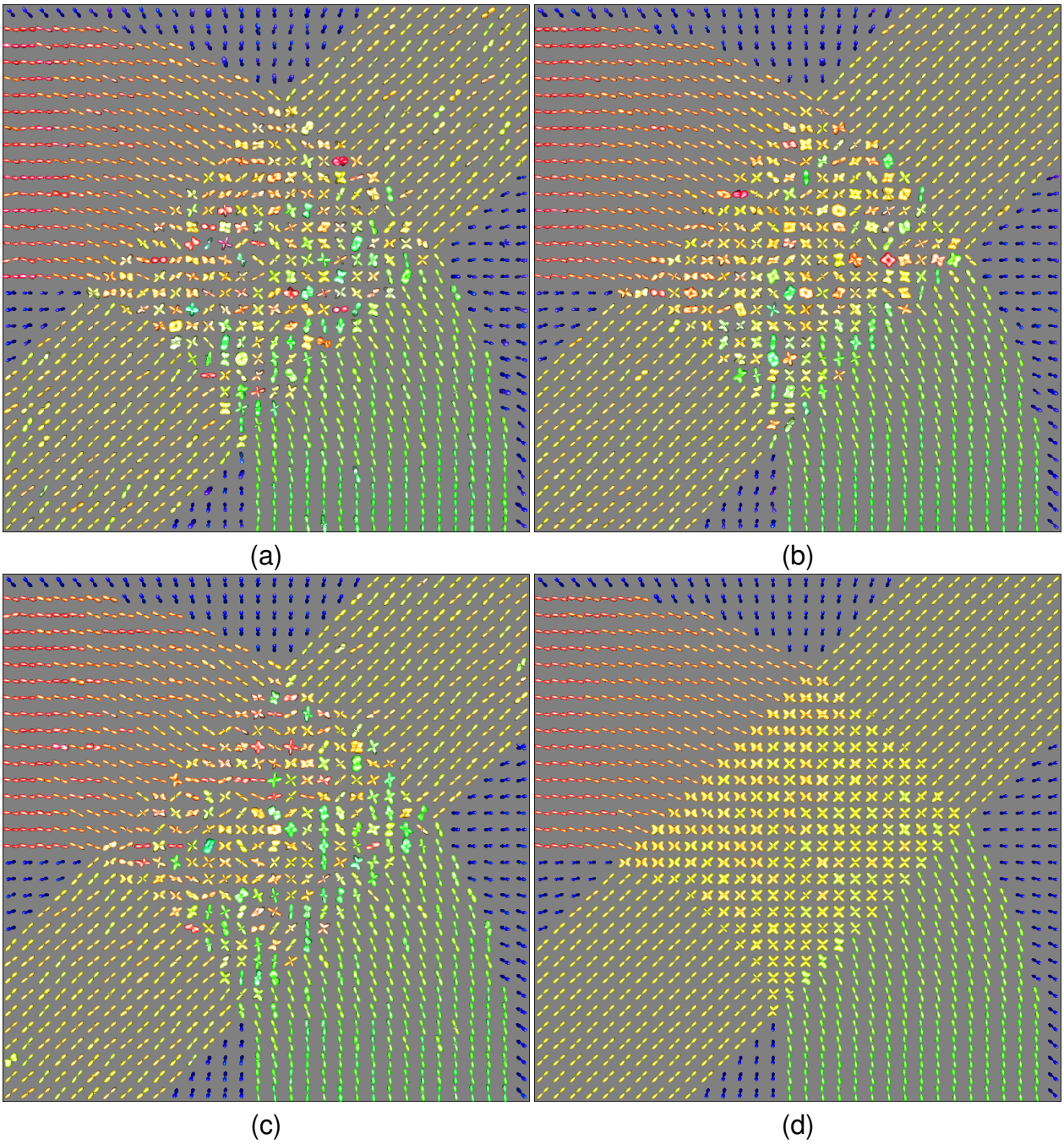

Figure 6-1. Reconstructed field ($\delta = 0.2$) using (a) voxel-wise individual reconstruction, (b) voxel-wise reconstruction on NLM denoised data field, (c) reconstruction using dictionary learning without smoothness regularization, (d) the proposed method.

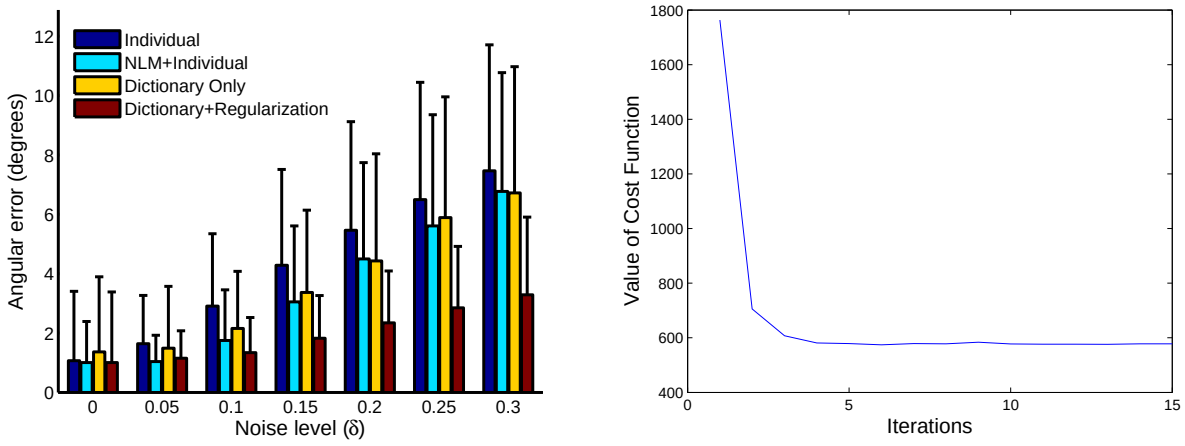

(a) (b)

Figure 6-2. (a) Comparison of the angular reconstruction errors with different noise level. (b) Plot showing the convergence of the cost function values over iterations.

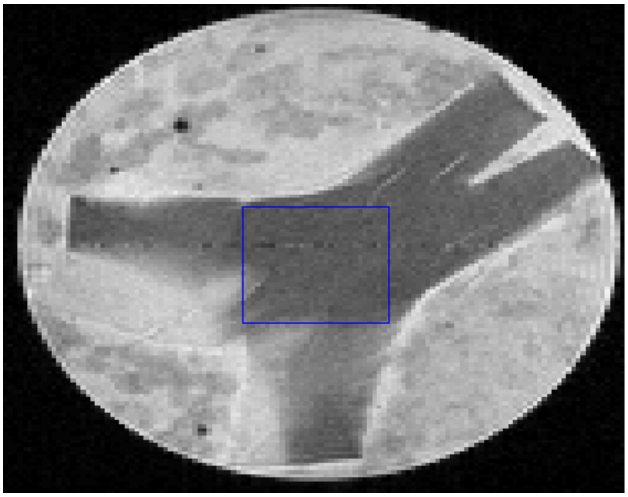

Figure 6-3. S_0 image of the optic chiasm and the ROI.

6.4.2 Real Dataset

We also performed an evaluation of the proposed method with real data from a rat optic chiasm, which contains samples measured with 46 different directions with b-value around $1240 s/mm^2$. The S_0 image as well as the region of interest, marked with a blue box, are shown in Figure 6-3. The reconstructed $P(\mathbf{r})$ field at the region of interest is shown in Figure 6-4. We observe that the proposed method generates a smooth reconstruction while keeping the underlying fiber structure. The parameter setting is the

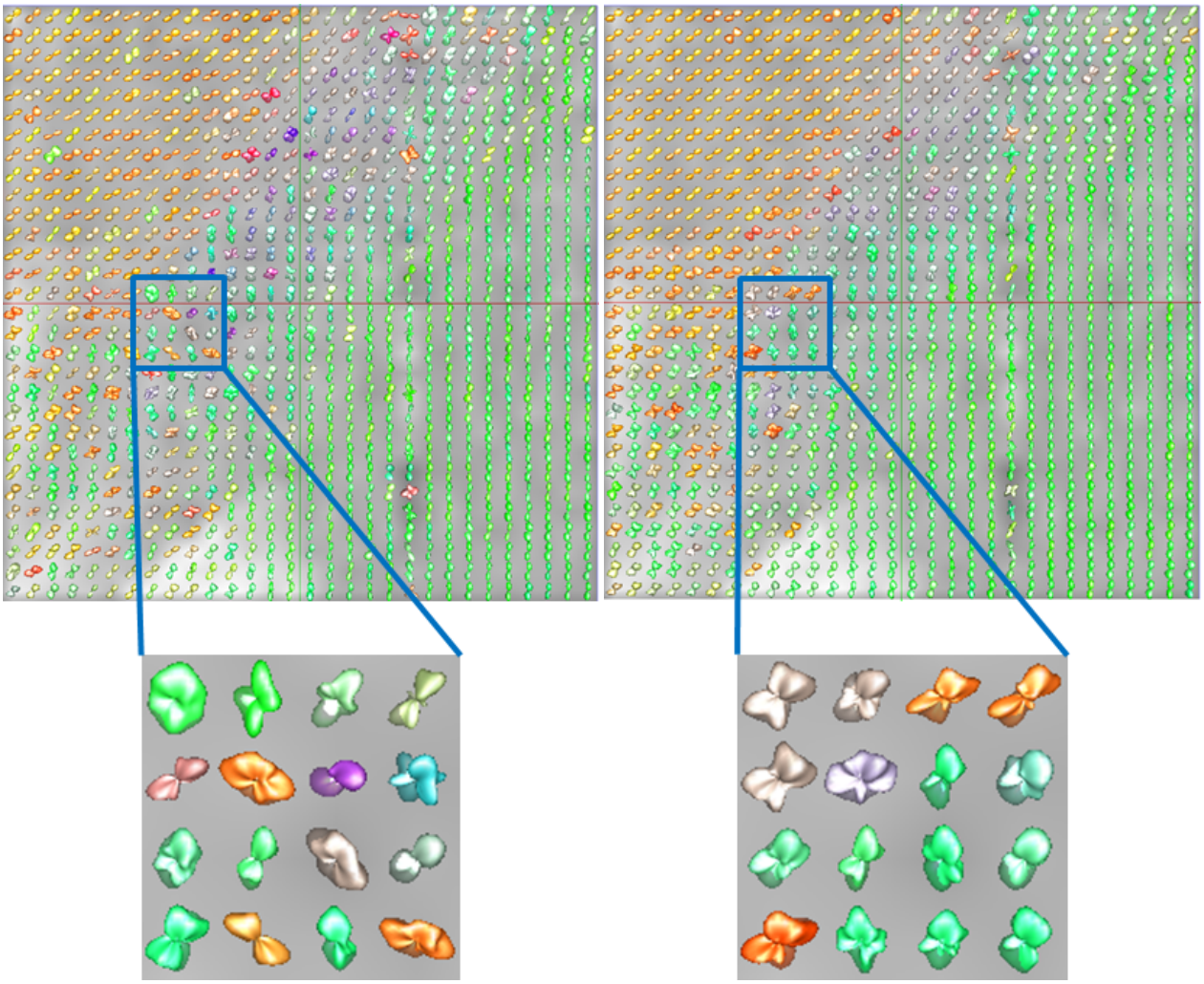

(a) (b)

Figure 6-4. Reconstructed region of interest using (a) voxel-wise individual reconstruction, (b) the proposed method. The zoomed in views show that the result from the proposed method is more regularized and the structures are preserved.

same as those used in the synthetic experiments except that we picked a different value of $T_0 = 12$ and estimated the value of $\delta = 0.17$ from the homogeneous (noisy) areas of the image.

CHAPTER 7
CONCLUSIONS

In this dissertation, a novel sampling scheme together with several reconstruction methods for reconstructing diffusion propagators were presented. To pursue the goal of more accurate reconstruction from less sample points, concepts of optimal sampling theory, ideal interpolating sinc function, box spline basis and dictionary learning were brought into the reconstruction framework. A new interlaced sampling scheme together with several reconstruction methods were proposed and evaluated with both synthetic and real diffusion MRI data.

Chapter 2 addressed the optimal sampling and interpolating problem in multivariate cases and provided the theoretical foundation for the reconstruction methods introduced in Chapter 3 and Chapter 4. Chapter 3 first introduced the use of optimal sampling lattice in the tomographic reconstruction of the diffusion propagators in DW-MRI. The benefit, increased accuracy, of replacing the traditional Cartesian lattice with the BCC lattice during interpolation procedure was validated. Then, the interlaced sampling geometry, which shares the interleaving structure of BCC lattice, was brought into the framework in addition to the optimal interpolation lattice. Since the sampling geometries and the interpolation lattices are independent, we could pick either interlaced or non-interlaced geometry and Cartesian or BCC lattice to form the final reconstruction (total of 4 combinations). Our experiments showed the improvements of the reconstruction accuracy, with no more samples, from both of the techniques. Another direction that the proposed framework can be applied is for the reduction of acquisition time. Compared to the standard (non-interlaced) data acquisition scheme, where we can achieve the same reconstruction accuracy, with fewer samples.

Chapter 5 is not a direct extension of Chapter 3 and Chapter 4. It is also rooted from the tomographic reconstruction framework, but the focus moved from the sampling lattices to higher order box spline bases for the representation of $P(\mathbf{r})$. The simple

voxel (cube) basis achieves a first order approximation in the context of tomographic reconstruction. The box spline framework allows one to employ higher-order basis functions that significantly increase the accuracy of reconstruction.

Chapter 6 extends the pixel-wise reconstruction framework onto the scenario of estimating the whole diffusion propagator field at the same time. A non-local regularized dictionary learning framework was presented to improve the reconstruction. Through learning a dictionary from the given data volume and enforcing the non-local regularization, this approach generated reconstructions at voxels that are robust to noise and preserve fiber structures at the same time.

Different concepts were brought together into the diffusion propagator reconstruction problem, addressing different aspects of the process. Combining these ideas will generate surprising, new ideas which have not been fully exploited yet. For example, a direct generalization is to adapt the interlaced geometry and optimal sampling lattices onto the box spline framework. Different box splines have already been defined on BCC and FCC lattices [43, 61], so it would be interesting to see the effects of combining box spline basis, BCC lattice and interlaced sampling. Moreover, bringing the spatial information from the diffusion propagator field into the tomographic reconstruction framework and using dictionary learning techniques to guide the sampling process are another two interesting directions to follow.

REFERENCES

[1] Abramowitz, M. and Stegun, I.A. *Handbook of mathematical functions with formulas, graphs, and mathematical tables*. Dover publications, 1964.

[2] Aganj, I., Lenglet, C., Sapiro, G., Yacoub, E., Ugurbil, K., and Harel, N. "Reconstruction of the orientation distribution function in single-and multiple-shell q-ball imaging within constant solid angle." *Magnetic Resonance in Medicine* 64 (2010).2: 554–566.

[3] Aharon, M., Elad, M., and Bruckstein, A. "K-SVD: An Algorithm for Designing Overcomplete Dictionaries for Sparse Representation." *TSP* 54 (2006).11: 4311–4322.

[4] Alexander, D. C., Barker, G. J., and Arridge, S. R. "Detection and modeling of non-Gaussian apparent diffusion coefficient profiles in human brain data." *Magn. Reson. Med.* 48 (2002).2: 331–340.

[5] Alim, U. and Möller, T. "An FFT with Rectangular Output on the BCC and FCC Lattices." *Intl Conf. Samp. Theory and Apps.*. 2009.

[6] Assaf, Y. and Basser, P.J. "Composite hindered and restricted model of diffusion (CHARMED) MR imaging of the human brain." *NeuroImage* 27 (2005).1: 48–58.

[7] Assaf, Y., Freidlin, R.Z., Rohde, G.K., and Basser, P.J. "New modeling and experimental framework to characterize hindered and restricted water diffusion in brain white matter." *Magnetic Resonance in Medicine* 52 (2004).5: 965–978.

[8] Assemlal, H-E., Tschumperlé, David, and Brun, Luc. "Evaluation of q-Space Sampling Strategies for the Diffusion Magnetic Resonance Imaging." *MICCAI*. London/England, 2009, 406–414.

[9] Bailey, A., Schlumprecht, Th., and Sivakumar, N. "Nonuniform sampling and recovery of multidimensional bandlimited functions by Gaussian radial-basis functions." *Arxiv preprint arXiv:0906.2105v3* (2010).

[10] Barmpoutis, A., Hwang, M.S., Howland, D., Forder, J.R., and Vemuri, B.C. "Regularized Positive-Definite Fourth-Order Tensor Field Estimation from DW-MRI." *Neuroimage* (2009).

[11] Barmpoutis, A., Jian, B., and Vemuri, B. C. "Adaptive kernels for multi-fiber reconstruction." *IPMI*. 2009, 338–349.

[12] Basser, P. J., Pajevic, S., Peierpaoli, C., J, Duda, and Aldroubi, A. "In vivo fiber tractography using DT-MRI data." *Magn. Reson. Med.* 44 (2000).4: 625–632.

[13] Basser, P.J., Mattiello, J., and LeBihan, D. "MR Diffusion Tensor Spectroscopy and Imaging." *Biophys. J.* 66 (1994): 259–267.

[14] Basser, P.J., Mattiello, J., LEBiHAN, D., et al. “Estimation of the effective self-diffusion tensor from the NMR spin echo.” *JMR B* 103 (1994): 247–254.

[15] Behmard, H. and Faridani, A. “Sampling of bandlimited functions on unions of shifted lattices.” *Journal of Fourier Analysis and Applications* 8 (2002).1: 43–58.

[16] Blinn, J. *Jim Blinn's corner: dirty pixels*. San Francisco, CA, USA: Morgan Kaufmann Publishers Inc., 1998.

[17] Bracewell, Ronald N. *The Fourier transform and its applications*. McGraw-Hill Series in Electrical Engineering. Circuits and Systems. New York: McGraw-Hill Book Co., 1986, third ed.

[18] Buades, A., Coll, B., and Morel, J.M. “A non-local algorithm for image denoising.” *CVPR*. vol. 2. IEEE, 2005, 60–65.

[19] Burns, Gerald and Glazer, A. M. *Space groups for solid state scientists*. Boston, MA: Academic Press Inc., 1990, second ed.

[20] Callaghan, P.T. *Principles of Nuclear Magnetic Resonance Microscopy*. Oxford: Clarendon Press, 1991.

[21] Cassels, J. W. S. *An introduction to the geometry of numbers*. Berlin: Springer-Verlag, 1971. Second printing, corrected, Die Grundlehren der mathematischen Wissenschaften, Band 99.

[22] Chenevert, TL, Brunberg, JA, and Pipe, JG. “Anisotropic diffusion in human white matter: demonstration with MR techniques in vivo.” *Radiology* 177 (1990).2: 401.

[23] Cheng, Jian, Merlet, Sylvain, Caruyer, Emmanuel, Ghosh, Aurobrata, Jiang, Tianzi, and Deriche, Rachid. “Compressive Sensing Ensemble Average Propagator Estimation via L1 Spherical Polar Fourier Imaging.” *MICCAI Workshop on CDMRI*. Toronto, Canada, 2011.

[24] Chiang, WY, Wedeen, VJ, Kuo, LW, Perng, MH, and Tseng, WYI. “Diffusion spectrum imaging using bodycenter-cubic sampling scheme.” *Proc Int Soc Magn Reson Med*. vol. 1041. 2006, 1041.

[25] Choi, B. “A fundamental theorem of algebra, spectral factorization, and stability of two-dimensional systems.” *IEEE Transactions on Signal Processing* 51 (2003).3: 853–863.

[26] Cleveland, GG, Chang, DC, Hazlewood, CF, and Rorschach, HE. “Nuclear magnetic resonance measurement of skeletal muscle: anisotrophy of the diffusion coefficient of the intracellular water.” *Biophysical Journal* 16 (1976).9: 1043–1053.

[27] Cohen, A. and Daubechies, I. “Nonseparable bidimensional wavelet bases.” *Rev. Mat. Iberoamericana* 9 (1993).1: 51–137.

[28] Cohen, Y. and Assaf, Y. “High b-value q-space analyzed diffusion-weighted MRS and MRI in neuronal tissues-a technical review.” *NMR in Biomedicine* 15 (2002).7-8: 516–542.

[29] Conturo, T. E., Lori, N. F., Cull, T. S., Akbudak, E., Snyder, A. Z., Shimony, J. S., McKinstry, R. C., Burton, H., and Raichle, M. E. “Tracking Neuronal Fiber Pathways in the Living Human Brain.” *Proc Natl Acad Sci* 96 (1999): 10422–10427.

[30] Conway, J.H and Sloane, N.J.A. *Sphere Packings, Lattices and Groups*. Springer, 1999, 3rd ed.

[31] Coulombe, S. and Dubois, E. “Multidimensional windows over arbitrary lattices and their application to FIR filter design.” *ICASSP ’96: Proceedings of the Acoustics, Speech, and Signal Processing, 1996. on Conference Proceedings., 1996 IEEE International Conference*. Washington, DC, USA: IEEE Computer Society, 1996, 2383–2386.

[32] Coupé, P., Yger, P., Prima, S., Hellier, P., Kervrann, C., and Barillot, C. “An optimized blockwise nonlocal means denoising filter for 3-D magnetic resonance images.” *Medical Imaging, IEEE Transactions on* 27 (2008).4: 425–441.

[33] Coxeter, H. S. M. “The classification of zonohedra by means of projective diagrams.” *J. Math. Pures Appl. (9)* 41 (1962): 137–156.

[34] de Boor, C., Höllig, K., and Riemenschneider, S. *Box Splines*, vol. 98 of *Applied Mathematical Sciences*. New York: Springer-Verlag, 1993.

[35] de Boor, C. and Ron, A. “Fourier analysis of the approximation power of principal shift-invariant spaces.” *Constr. Approx.* 8 (1992).4: 427–462.

[36] Descoteaux, M., Angelino, E., Fitzgibbons, S., and Deriche, R. “Regularized, fast, and robust analytical Q-ball imaging.” *Magnetic Resonance in Medicine* 58 (2007).3: 497–510.

[37] Descoteaux, M., Deriche, R., Le Bihan, D., Mangin, J.F., and Poupon, C. “Diffusion Propagator Imaging: Using Laplaces Equation and Multiple Shell Acquisitions to Reconstruct the Diffusion Propagator.” *Information Processing in Medical Imaging*. Springer, 2009, 1–13.

[38] ———. “Multiple q-shell diffusion propagator imaging.” *Medical Image Analysis* 15 (2011): 603–621.

[39] Descoteaux, M., Wiest-Daesslé, N., Prima, S., Barillot, C., and Deriche, R. “Impact of rician adapted non-local means filtering on hardi.” *Medical Image Computing and Computer-Assisted Intervention–MICCAI 2008* (2008): 122–130.

[40] Deza, M. and Grishukhin, V. “Voronoĭ’s conjecture and space tiling zonotopes.” *Mathematika* 51 (2004).1-2: 1–10 (2005).

[41] Dudgeon, D. E. and Mersereau, R. M. *Multidimensional Digital Signal Processing*. Englewood-Cliffs, NJ: Prentice-Hall, Inc., 1984, 1st ed.

[42] Entezari, A. *Optimal Sampling Lattices and Trivariate Box Splines*. Ph.D. thesis, Simon Fraser University, Vancouver, Canada, 2007.

[43] Entezari, A., Dyer, R., and Moller, T. "Linear and cubic box splines for the body centered cubic lattice." *Visualization, 2004. IEEE*. IEEE, 2004, 11–18.

[44] Entezari, A., Dyer, R., and Möller, T. "From sphere packing to the theory of optimal lattice sampling." *Mathematical Foundations of Scientific Visualization, Computer Graphics, and Massive Data Exploration. Springer* (2009).

[45] Entezari, A. and Unser, M. "A box spline calculus for computed tomography." *ISBI*. IEEE, 2010, 600–603.

[46] Erdahl, R. M. "Zonotopes, dicings, and Voronoi's conjecture on parallelohedra." *European J. Combin.* 20 (1999).6: 527–549.

[47] *et al*, A. Entezari. "Practical Box Splines for Reconstruction on the Body Centered Cubic Lattice." *IEEE Trans. Vis. Comp. Graph.* 14 (2008).2: 313–328.

[48] *et al*, H.R. Kunsch. "Optimal lattices for sampling." *IEEE Tran. Info. Theory* 51(2) (2005): 634–647.

[49] Faridani, A. and Ritman, E.L. "High-resolution computed tomography from efficient sampling." *Inverse Problems* 16 (2000): 635.

[50] Frank, L.R. "Characterization of Anisotropy in High Angular Resolution Diffusion Weighted MRI." *Magn. Reson. Med.* 47 (2002).6: 1083–1099.

[51] Hamitouche, C., Ibáñez, L., and Roux, C. "Discrete Topology of (A_n^*) Optimal Sampling Grids. Interest in Image Processing and Visualization." *J. Math. Imaging Vis.* 23 (2005).3: 401–417.

[52] Hart, G.W. "Zonohedrification." *Mathematica Journal* 7 (1999).3: 374–389.

[53] Higgins, J. R. *Sampling theory in Fourier and signal analysis: foundations*. Oxford University Press, USA, 1996.

[54] Hofer, S. and Frahm, J. "Topography of the human corpus callosum revisited–comprehensive fiber tractography using diffusion tensor magnetic resonance imaging." *NeuroImage* 32 (2006).3: 989–994.

[55] J. Kovačević and Vetterli, M. "Nonseparable Multidimensional Perfect Reconstruction Filter Banks and Wavelet Bases for $\mathbb{R}^n$." *IEEE Transactions on Information Theory* 17 (1992).10: 939–954.

[56] Jian, B. and Vemuri, B.C. “A unified computational framework for deconvolution to reconstruct multiple fibers from diffusion weighted MRI.” *TMI* 26 (2007).11: 1464–1471.

[57] Jian, B., Vemuri, B.C., Özarslan, E., Carney, P.R., and Mareci, T.H. “A novel tensor distribution model for the DWMR signal.” *NeuroImage*. vol. 37(1). 2007, 164–176.

[58] Kazhdan, M. “Reconstruction of solid models from oriented point sets.” *Proceedings of the third Eurographics symposium on Geometry processing*. Eurographics Association, 2005, 73.

[59] Kezele, I., Descoteaux, M., Poupon, C., Poupon, F., and Mangin, J.F. “Spherical wavelet transform for ODF sharpening.” *Medical Image Analysis* 14 (2010).3: 332–342.

[60] Kim, M., Entezari, A., and Peters, J. “Box Spline Reconstruction on the Face Centered Cubic Lattice.” *IEEE Trans. on Visualization and Computer Graphics* 14 (2008).6: 1523–1530.

[61] ———. “Box spline reconstruction on the face-centered cubic lattice.” *Visualization and Computer Graphics, IEEE Transactions on* 14 (2008).6: 1523–1530.

[62] Kluvanek, I. “Sampling theorem in abstract harmonic analysis.” *Mat.-Fyz. Casopis Sloven. Akad. Vied* 15 (1965): 43–48.

[63] Kowalski, M. A., Sikorski, K. A., and Stenger, F. *Selected topics in approximation and computation*. New York, NY, USA: Oxford University Press, Inc., 1995.

[64] Kumar, Ritwik, Vemuri, Baba C., Wang, Fei, Syeda-Mahmood, Tanveer, Carney, Paul R., and Mareci, Thomas H. “Multi-fiber Reconstruction from DW-MRI data using a Continuous Mixture of Hyperspherical von Mises-Fisher Distributions.” *Information Processing in Medical Imaging (IPMI)*. 2009, 139–150.

[65] Lanczos, Cornelius. *Discourse on Fourier series*. New York, Hafner, 1966.

[66] Le Bihan, D., Breton, E., Lallemand, D., Grenier, P., Cabanis, E., and Laval-Jeantet, M. “MR imaging of intravoxel incoherent motions: application to diffusion and perfusion in neurologic disorders.” *Radiology* 161 (1986).2: 401.

[67] Lee, S.K., Kim, D.I., Kim, J., Kim, D.J., Kim, H.D., Kim, D.S., and Mori, S. “Diffusion-Tensor MR Imaging and Fiber Tractography: A New Method of Describing Aberrant Fiber Connections in Developmental CNS Anomalies1.” *Radiographics* 25 (2005).1: 53.

[68] Leergaard, T.B., White, N.S., De Crespigny, A., Bolstad, I., DArceuil, H., Bjaalie, J.G., and Dale, A.M. “Quantitative histological validation of diffusion MRI fiber orientation distributions in the rat brain.” *PLoS One* 5 (2010).

[69] Lu, Y. M., Do, M. N., and Laugesen, R. S. "A computable Fourier condition generating alias-free sampling lattices." *IEEE Transactions on Signal Processing* 57 (2009): 1768–1782.

[70] Lucarini, V. "Three-dimensional Random Voronoi Tessellations: From Cubic Crystal Lattices to Poisson Point Processes." *Journal of Statistical Physics* 134 (2009).1: 185–206.

[71] Lyubarskii, Y.I. and Rashkovskii, A. "Complete interpolating sequences for Fourier transforms supported by convex symmetric polygons." *Arkiv för Matematik* 38 (2000).1: 139–170.

[72] Mallat, S. *A wavelet tour of signal processing*. Academic Press, 2009.

[73] Marschner, S. R. and Lobb, R. J. "An Evaluation of Reconstruction Filters for Volume Rendering." *Proceedings of the IEEE Conference on Visualization 1994*. eds. R. Daniel Bergeron and Arie E. Kaufman. Los Alamitos, CA, USA: IEEE Computer Society Press, 1994, 100–107.

[74] McMullen, P. "On zonotopes." *Trans. Amer. Math. Soc.* 159 (1971): 91–109.

[75] ———. "Space tiling zonotopes." *Mathematika* 22 (1975).2: 202–211.

[76] Meijering, E. "A Chronology of Interpolation: From Ancient Astronomy to Modern Signal and Image Processing." *Proceedings of the IEEE* 90 (2002).3: 319–342.

[77] Menzel, M.I., Tan, E.T., Khare, K., Sperl, J.I., King, K.F., Tao, X., Hardy, C.J., and Marinelli, L. "Accelerated diffusion spectrum imaging in the human brain using compressed sensing." *Mag. Res. in Medicine* 66 (2011).5: 1226–1233.

[78] Merlet, Sylvain and Deriche, Rachid. "Compressed Sensing for Accelerated EAP Recovery in Diffusion MRI." *MICCAI*. Pekin, Chine, 2010, 14.

[79] Meyer, F. "Mathematical Morphology: from two dimensions to three dimensions." *Journal of Microscopy* 165 (1992).1: 5–28.

[80] Michailovich, O., Rathi, Y., and Dolui, S. "Spatially regularized compressed sensing for high angular resolution diffusion imaging." *TMI* 30 (2011).5: 1100–1115.

[81] Middleton, L. and Sivaswamy, J. *Hexagonal Image Processing: A Practical Approach*. Springer, 2005.

[82] Mirzargar, M. and Entezari, A. "Voronoi Splines." *Signal Processing, IEEE Transactions on* 58 (2010).9: 4572 –4582.

[83] Miyakawa, H. "Sampling theorem of stationary stochastic variables in multidimensional space." *Journal of the Institute of Electronic and Communication Engineers of Japan* 42 (1959): 421–427.

[84] Mori, S., Crain, B. J., Chacko, V. P., and van Zijl, P. C. M. "Three-Dimensional Tracking of Axonal Projections in the Brain by Magnetic Resonance Imaging." *Ann Neurol* 45 (1999): 265–269.

[85] Moseley, ME, Cohen, Y., Kucharczyk, J., Mintorovitch, J., Asgari, HS, Wendland, MF, Tsuruda, J., and Norman, D. "Diffusion-weighted MR imaging of anisotropic water diffusion in cat central nervous system." *Radiology* 176 (1990).2: 439.

[86] Moseley, ME, Cohen, Y., Mintorovitch, J., Chileuitt, L., Shimizu, H., Kucharczyk, J., Wendland, MF, and Weinstein, PR. "Early detection of regional cerebral ischemia in cats: comparison of diffusion-and T2-weighted MRI and spectroscopy." *Magnetic resonance in medicine* 14 (1990).2: 330–346.

[87] Oppenheim, A.V. and Schafer, R.W. *Discrete-Time Signal Processing*. Prentice Hall Inc., Englewoods Cliffs, NJ, 1989.

[88] Özarslan, E. and Mareci, T. H. "Generalized DTI and analytical relationships between DTI and HARDI." *MRM* 50(5) (2003): 955–965.

[89] Özarslan, E., Shepherd, T. M., Vemuri, B. C., Blackband, S. J., and Mareci, T. H. "Resolution of Complex Tissue Microarchitecture using the Diffusion Orientation Transform (DOT)." *NeuroImage* 31 (2006): 1086–1103.

[90] Özarslan, E., Vemuri, Baba C., and Mareci, Thomas. "Fiber Orientation Mapping Using Generalized Diffusion Tensor Imaging." *International Symposium on Biomedical Imaging: From Nano to Macro*. 2004, 1036–1038.

[91] Petersen, D. P. and Middleton, D. "Sampling and Reconstruction of Wave-Number-Limited Functions in N-Dimensional Euclidean Spaces." *Information and Control* 5(4) (1962): 279–323.

[92] Pickalov, V. and Basser, P.J. "3d tomographic reconstruction of the average propagator from mri data." *3rd IEEE ISBI*. 2006, 710–713.

[93] Prandoni, P. and Vetterli, M. "From Lagrange to Shannon...and Back: Another Look at Sampling." *IEEE Signal Processing Magazine* 26 (2009).5: 138–144.

[94] Saranathan, M., Ramanan, V., Gulati, R., and Venkatesan, R. "ANTHEM: anatomically tailored hexagonal MRI." *Magnetic Resonance Imaging* 25 (2007).7: 1039–1047.

[95] Senay, S., Chaparro, L.F., and Akan, A. "Sampling and reconstruction of nonbandlimited signals using Slepian functions." *EUSIPCO, Lusanne, Switzerland* (2008): 25–29.

[96] Senechal, M. *Quasicrystals and Geometry*. Cambridge University Press, 1995.

[97] Slepian, D. "Prolate spheroidal wave functions, Fourier analysis, and uncertainty. V-The discrete case." *AT T Technical Journal* 57 (1978): 1371–1430.

[98] Söderman, O. and Jönsson, B. “Restricted diffusion in cylindrical geometry.” *J. Magn. Reso., Ser A* 117 (1995).1: 94–97.

[99] Stejskal, E. O. and Tanner, J. E. “Spin Diffusion Measurements: Spin Echoes in the Presence of a Time-DependentField Gradient.” *J. Chem. Phys.* 42 (1965).2: 288–292.

[100] Stenger, F. *Numerical methods based on Sinc and analytic functions*. Springer Verlag, 1993.

[101] ———. “Polynomial function and derivative approximation of Sinc data.” *J. Complex.* 25 (2009).3: 292–302.

[102] Strand, R. and Stelldinger, P. “Topology Preserving Marching Cubes-like Algorithms on the Face-Centered Cubic Grid.” *Image Analysis and Processing, 2007. ICIAP 2007. 14th International Conference on*. 2007, 781–788.

[103] Sugihara, M. “De-Sinc numerical methods.” *SNC ’09: Proceedings of the 2009 conference on Symbolic numeric computation*. New York, NY, USA: ACM, 2009, 9–10.

[104] Tournier, J. D., Calamante, F., Gadian, D. G., and Connelly, A. “Direct estimation of the fiber orientation density function from diffusion-weighted MRI data using spherical deconvolution.” *NeuroImage* 23 (2004).3: 1176–1185.

[105] Tournier, J.-Donald, Calamante, Fernando, Gadian, David G., and Connelly, Alan. “Direct estimation of the fiber orientation density function from diffusion-weighted MRI data using spherical deconvolution.” *NeuroImage* 23 (2004).3: 1176–1185.

[106] Tristán-Vega, A., Westin, C.F., and Aja-Fernández, S. “Estimation of fiber orientation probability density functions in high angular resolution diffusion imaging.” *NeuroImage* 47 (2009).2: 638–650.

[107] Tuch, D. S. “Q-ball imaging.” *Magn. Reson. Med.* 52 (2004).6: 1358–1372.

[108] Tuch, D. S., Weisskoff, R. M., Belliveau, J. W., and Wedeen, V. J. “High Angular Resolution Diffusion Imaging of the Human Brain.” *Proc. of the 7th ISMRM*. Philadelphia, 1999, 321.

[109] Tuch, D.S., Reese, T.G., Wiegell, M.R., Makris, N., Belliveau, J.W., and Wedeen, V.J. “High angular resolution diffusion imaging reveals intravoxel white matter fiber heterogeneity.” *MRM* 48(4) (2002): 577–582.

[110] Tuch, D.S., Reese, T.G., Wiegell, M.R., and Van J, W. “Diffusion MRI of complex neural architecture.” *Neuron* 40 (2003).5: 885–895.

[111] Unser, M. “Sampling—50 Years After Shannon.” *Proceedings of the IEEE* 88 (2000).4: 569–587.

[112] Vaidyanathan, P.P. *Multirate Systems and Filter Banks*. Signal Processing. Englewood Cliffs, New Jersey 07632: Prentice Hall, 1993.

[113] Van De Ville, D., Blu, T., Unser, M., Philips, W., Lemahieu, I., and Van de Walle, R. "Hex-Splines: A Novel Spline Family for Hexagonal Lattices." *IEEE Transactions on Image Processing* 13 (2004).6: 758–772.

[114] von dem Hagen, E.A.H. and Henkelman, R.M. "Orientational diffusion reflects fiber structure within a voxel." *Magn. Reson. Med.* 48 (2002).3: 454–459.

[115] vuVolume. "A Framework for General Rendering and Visualization Algorithms." http://vuvolume.sourceforge.net/, 2004. [Online; accessed 13-Feb-2012].

[116] Wedeen, VJ, Reese, TG, Tuch, DS, Weigel, MR, Dou, JG, Weiskoff, RM, and Chessler, D. "Mapping fiber orientation spectra in cerebral white matter with Fourier transform diffusion MRI." *8th ISMRM*. 2000, 82.

[117] Wei, D. and Guo, S. "A new approach to the design of multidimensional nonseparable two-channel orthonormal filterbanks and wavelets." *Signal Processing Letters, IEEE* 7 (2000).11: 327–330.

[118] Wu, Y.C. and Alexander, A.L. "Hybrid diffusion imaging." *NeuroImage* 36 (2007).3: 617–629.

[119] Yan, C., Gong, G., Wang, J., Wang, D., Liu, D., Zhu, C., Chen, Z.J., Evans, A., Zang, Y., and He, Y. "Sex-and Brain Size–Related Small-World Structural Cortical Networks in Young Adults: A DTI Tractography Study." *Cerebral Cortex* 21 (2011).2: 449.

[120] Ye, W. and Entezari, A. "A Geometric Construction of Multivariate Sinc Functions." *IEEE Transactions on Image Processing* (Accepted 2011).

BIOGRAPHICAL SKETCH

Wenxing Ye received his B.E. degree from the Department of Automation at University of Science and Technology of China, Hefei, China in 2004. Then he was enrolled in the graduate program at Graduate University of the Chinese Academy of Sciences, associated to the Institute of automation. In 2006, he chose to pursue his Ph.D. degree in the Department of Electrical and Computer Engineering at the University of Florida. He has been working in the Multimedia Communications and Networking Lab and joint the laboratory for Computer Vision, Graphics, and Medical Imaging in 2009. His research interests include medical image processing, machine learning and image analysis. He would like to make contributions to the society through innovative and continuous research.